Doctoral Thesis

Charge Kinetics Study to Improve Photo-energy Conversion & Storage Efficiency using Thin Photoactive TiO_2 Film

Byung-Man Kim

Department of Chemical Engineering

Graduate School of UNIST

2018

Charge Kinetics Study to Improve Photo-energy Conversion & Storage Efficiency using Thin Photoactive TiO_2 Film

Byung-Man Kim

Department of Chemical Engineering

Graduate School of UNIST

Charge Kinetics Study to Improve Photo-energy Conversion & Storage Efficiency using Thin Photoactive TiO_2 Film

A thesis/dissertation
submitted to the Graduate School of UNIST
in partial fulfillment of the
requirements for the degree of
Doctor of Philosophy

Byung-Man Kim

5. 31. 2018
Approved by

_____

Advisor
Tae-Hyuk Kwon

Charge Kinetics Study to Improve Photo-energy Conversion & Storage Efficiency using Thin Photoactive TiO_2 Film

Byung-Man Kim

This certifies that the thesis/dissertation of Byung-Man Kim is approved.

5. 31. 2018

Signature

_____

Advisor: Tae-Hyuk Kwon

Signature

_____

Sang-Young Lee

Signature

_____

Hyun-Kon Song

Signature

_____

Kwanyong Seo

Signature

_____

Jin Young Kim

Abstract

Dye-sensitized solar cells (DSCs) have been often used as photo-energy converter in hybrid photo-rechargeable system because of their several advantages, especially high performance under low light intensity. Nevertheless, it is still veiled which factors are influential for the performance of DSC-combined energy storage devices.

First, I investigated the correlation between charge kinetics in mesoporous TiO_2 network and photocurrent density (J_{SC}) according to the film thickness. The findings suggest that four factors be considered to understand photocurrent generation, such as the efficiencies of light harvesting (η_{lh}), charge injection (η_{inj}), charge collection (η_{cc}), charge regeneration (η_{reg}). Among them, η_{inj} becomes more influential for J_{SC} when decreasing TiO_2 film thickness, while η_{coll} and η_{reg} become gradually less influential. Following studies were carried out to further improve J_{SC} using thin mesoporous TiO_2 film below 2.0-μm by controlling dye distribution in the mesoporous film.

Finally, thin mesoporous TiO_2 film (ca. 1.8-μm)-based photo-electrode was applied to 3-electrode photo-rechargeable system that is consisting of dyed TiO_2 photo-electrode, catalytic-functionalized membrane electrode, and $LiMn_2O_4$ storage-electrode, named as dye-sensitized solar battery (DSSB). Three kinds of redox mediators, such as I^-/I_3^-, $Co^{+2/+3}(bpy)_3$, and $Cu^{+/+2}(dmp)_2$, were introduced as charge regenerator for oxidized dye.

As a result, I^-/I_3^- delivering the highest photo-injection current generally provided the highest photo-charging current (J_{Ch}) and thus stored energy (E_{stored}) under 1 sun condition (1000 W m^{-2}), followed by $Co^{+2/+3}(bpy)_3$ and $Cu^{+/+2}(dmp)_2$. However, under dim lighting (1. 37 W m^{-2}, 410 lux), $Cu^{+/+2}(dmp)_2$ showed the highest E_{stored} corresponding to 8.8% of overall photo-energy conversion/storage efficiency ($\eta_{overall}$). The trend of $\eta_{overall}$ under dim lighting indicates that output voltage gradually becomes more influential for E_{stored} as the incident light intensity decreases, while the impact of J_{Ch} becomes small. These findings present which factors we should consider to develop the indoor-customized photo-rechargeable system.

Contents

List of Figures

List of Tables

Chapter 1 Introduction ---------- 1

1.1 Motivation ---------- 1

1.2 Dye-sensitized Solar Cells (DSCs) ---------- 3

1.2.1 Structure and Working Principle ---------- 3

1.2.2 Research Strategy ---------- 4

1.3 Hybrid Photo-rechargeable Systems ---------- 7

REFERENCE ---------- 10

Chapter 2 Experimental Methods ---------- 14

2.1 DSCs Fabrication ---------- 14

2.2 Characterization Techniques ---------- 17

2.2.1 Current-Voltage (J-V) Measurement ---------- 17

2.2.2 Incident Photon-to-Current Conversion Efficiency (IPCE) ---------- 18

2.2.3 Controlled Intensity Modulated Photo Spectroscopy (CIMPS) ---------- 20

2.2.4 Electrochemical Impedance Spectroscopy (EIS) ---------- 23

REFERENCE ---------- 27

Chapter 3 Performance Optimization of Thin Photoactive TiO_2 Film-based DSCs using Indoline-based Sensitizer---------- 31

3.1 Introduction ---------- 31

3.2 Results and Discussion ---------- 33

3.3 Conclusion ---------- 54

3.4 Experimental Section ---------- 55

REFERENCE ---------- 57

Chapter 4 Control and Monitoring of Dye Distribution in Mesoporous TiO_2 Film for Improving Photovoltaic Performance ---------- 61

4.1 Introduction ---------- 61

4.2 Results and Discussion ---------- 62

4.3 Conclusion ---------- 81

4.4 Experimental Section ---------- 82

REFERENCE ---------- 88

Chapter 5 Light Intensity Dependent Photo-energy Conversion/Storage Efficiency of Dye-sensitized Solar Battery (DSSB) ---------- 92

5.1 Introduction ---------- 92

5.2 Results and Discussion ---------- 94

5.3 Conclusion ---------- 115

5.4 Experimental Section ---------- 116

REFERENCE ---------- 120

Acknowledgement ---------- 128

List of Figures

[Chapter 1]

Figure 1.1 World annual solar photovoltaics cell production from 1990 to 2013, with projection to 2017 (Earth Policy Institute - www.earth-policy.org)**.**

Figure 1.2 (a) Schematic of a typical DSSC and (b) Overview of processes and typical time constants under working conditions (1 sun) in a Ru-based DSC with I^-/I_3^- redox couples.

Figure 1.3 Schematic of a building energy management system (BEMS).

Figure 1.4 TiO_2 film thickness dependent (a) transparency and (b) film state after bending test.

Figure 1.5 Time dependent PV energy production and energy demand curves.

Figure 1.6 The comparison of two types of photo-rechargeable systems.

Figure 1.7 Li^+ ion active potentials and performances of cathode materials for lithium ion battery.

[Chapter 2]

Figure 2.1 Dye-sensitized solar cell fabrication process.

Figure 2.2 2D surface scanning profiles of TiO_2 layer according to the number of printing.

Figure 2.3 Typical current density-voltage curve from DSCs with corresponding power density.

Figure 2.4 (a) Charge behavior (blue arrow for electron and orange arrow for redox mediator) for photocurrent generation since photo-excitation of sensitizer. (b) IPCE spectra as a function of chopping frequency in AC mode.

Figure 2.5 (a) Schematic of the CIMPS principle. The photo-diode detector/sense amplifier feedback loop forces the light source potentiostat to control light intensity exactly. (b) Actual photograph during the measurement. Photo-sensor is placed near the cell.

Figure 2.6 Light intensity dependent frequency response of (a) photocurrent efficiency (η_{IP}'') and (b) photovoltage efficiency (η_{UP}'') in the complex plane, displayed in Bode plot.

Figure 2.7 (a) Spectroscopic representation of the electrical stimulus on the object and resulting frequency response and (b) representation of vector Z on complex plane.

Figure 2.8 Typical Nyquist diagram obtained from liquid type DSC. Inset shows the structure of DSC with corresponding equivalent circuit (transmission line model).

Figure 2.9 (a) The Fermi level distribution by diffusion–recombination of electrons and photogeneration in a TiO_2 film with L = 10-μm, in dark and under illumination and (b) schematic description of electron diffusion in the TiO_2 film in dark and under illumination. (c) Experimental impedance spectra of a D-DAHTDTT organic dye cell with a liquid electrolyte, measured by applying a forward bias (–0.65 V) with 10 mV modulation in dark and under illumination.

[Chapter 3]

Figure 3.1 Chemical structures of the **RK-1** – **4** organic dyes.

Figure 3.2 (a) UV-vis and photoluminescence spectra for **RK-1** – **4**, measured in a 20 μM CH_2Cl_2 solution containing 0.1 M triethylamine. (b) Cyclic voltammograms obtained from **RK** dye-dissolved CH_2Cl_2 solution containing tetrabutylammonium hexafluorophosphate ($TBAPF_6$,) as a supporting electrolyte.

Figure 3.3 HOMO, LUMO, and electron density difference maps between the excited and ground states of **RK-1** – **4** dyes.

Figure 3.4 Spin density distribution in oxidized monomeric dye, corresponding to **RK-1** – **4** from left one by one.

Figure 3.5 J-V curves of DSCs based on **RK** organic dyes according to the active layer thickness: (a) 1.8-μm and (b) 3.5-μm.

Figure 3.6 Photocurrent density of **RK** DSCs with (a) 1.8-μm and (b) 3.5-μm TiO_2 film as active layer, measured according to incident light intensity. For certainty, corresponding external quantum efficiency is also presented

Figure 3.7 Charge injection efficiency of **RK** DSCs with (a) 1.8-μm and (b) 3.5-μm TiO_2 film as active layer, calculated from Eq.3.2 Piers R. F. Barnes *et al.* reported.

Figure 3.8 Absorbance spectra of **RK** dye-sensitized TiO_2 film (1.8-μm) as a function of soaking time. Note initial states until 3 min.

Figure 3.9 Normalized absorbance spectra separated by the soaking time until 10 min, derived from Figure 3.8.

Figure 3.10 Proposed dye adsorption processes according to the alkyl chain length.

Figure 3.11 Time-resolved PL signals from the **RK** dye-sensitized ZrO_2 layer surrounded by inert electrolyte.

Figure 3.12 Light harvesting efficiency of **RK** dye-sensitized TiO_2 film according to film thickness: (a) 1.8-μm and (b) 3.5-μm.

Figure 3.13 The trend of charge transport time, recombination time, collection efficiency, and diffusion length depending on the TiO_2 thickness: (a, c, e, g) 1.8-μm and (b, d, f, h) 3.5-μm.

Figure 3.14 Impedance spectra in Nyquist plots depending on the TiO_2 thickness: (a) 1.8-μm and (b) 3.5-μm.

Figure 3.15 Structure of the dummy cell used for the exciton lifetime and regeneration yield acquisition.

Figure 3.16 Time-resolved PL signals from the **RK-2** dye-sensitized ZrO_2 layer depending on the iodine electrolyte concentration.

Figure 3.17 Incident photon-to-current conversion efficiency of **RK** DSCs, presented according to the TiO_2 film thickness: (a) 1.8-μm and (b) 3.5-μm.

[Chapter 4]

Figure 4.1 Proposed dyeing mechanisms of GBS (upper) and OS (lower), and the molecular structures of three dyes used, N719, YD2, and DAHTDTT (right).

Figure 4.2 The difference in tonal contrast of 7-μm TiO_2 film according to dyeing method, (a) GBS and (b) OS, for the same time.

Figure 4.3 Photocurrent density-voltage curves of DSCs with 7-μm-thick active layer based on single (N719) and co-dyes (N719 + YD2), using different dyeing conditions.

Figure 4.4 Transient PL signals obtained from the dyed ZrO_2 film surrounded by inert electrolytes.

Figure 4.5 (a) Schematic representation of plasmon sensor consisted of FTO layer, Au nanoparticle layer, and dyed porous TiO_2 layer: (b) In plasmon sensor, dyes supply photoelectrons under electromagnetic radiation so that intrinsic LSPR peak is blue-shifted. (c) Cross section SEM image of plasmon sensor. (d) Enlargement of interface between FTO and porous TiO_2 layer. (e) EDX result in the selected area (red rectangle in Figure 3d), indicating the existence of Au. (f) LSPR peak blue-shift according to GBS and OS soaking time. Note that GBS gives much faster initiation, saturation, and higher maximum values of peak blue-shift than OS. TOF-SIMS depth profiles of N719-sensitized TiO_2 films according to dyeing condition: (g) 15 min of GBS and (h) 1 h of OS.

Figure 4.6. The evolutions of absorbance peak of plasmon sensors after dyeing, presented according to dyeing condition, such as (a) 2 min of GBS, (b) 8 min of GBS, (c) 15 min of GBS, (d) 15 min of OS, and (e) 30 min of OS.

Figure 4.7 (a) Difference in charge collection kinetics according to the dye distribution, slow (left) and fast (right) charge transport with long and short dye-free sites, respectively. (b) Charge transport times from N719-based DSCs using a 7-μm-thick active layer as a function of incident photon flux (503 nm, 130 W m^{-2}) and (c) corresponding imaginary component of photocurrent response depending on the modulation frequency applied on the light source bias.

Figure 4.8 (a) Nyquist plots from N719-based DSCs using 7-μm-thick active layer according to dyeing condition. Inset is the equivalent circuit used for fitting. EIS was conducted at 1 sun illumination, applying

a 10 mV AC modulation overlapped in DC forward bias ($-V_{OC}$) with the frequency ranging from 10^6 to 10^{-1} Hz. Charge extraction process of (b) without delay and (c) with delay represented by V_{OC} (solid line) and Q_{ext} (dashed line) as a function of progress time.

Figure 4.9 The photographs of experimental apparatus for GBS process.

Figure 4.10 The photographs of plasmon sensors at each fabrication step, (a) first, (b) second, (c) third, and (d) forth step. Figure 4.10d shows all plasmon sensors after dyeing at various conditions using 0.08 mM N719 solution.

Figure 4.11 Absorbance spectra from plasmon sensors at each fabrication step, (a) first, (b) second, (c) third, and (d) forth step.

Figure 4.12 The plane SEM images in (a) low and (b) high magnification and (c) XRD patterns of plasmon sensor at second step.

[Chapter 5]

Figure 5.1 (a) The structure and working principle of DSSB. Inset shows the molecular structures of Y123 dye, $Co^{+2/+3}(bpy)_3(PF_6)_{2/3}$, and $Cu^{+/+2}(dmp)_2TFSI_{1/2}$ at left side. (b) The schematic diagram of output voltage formation before (4 $V_{Li+/Li}$) and after (3 $V_{Li+/Li}$) surface-graphatization of $LiMn_2O_4$. (c) Cyclic voltammograms of $Li_2Mn_2O_4/LiMn_2O_4$ (deep blue), I^-/I_3^- (black), $Co^{2+/3+}(bpy)_3(PF_6)_{2/3}$ (red), and $Cu^{+/2+}(dmp)_2TFSI_{1/2}$ (blue) in 0.1 M $LiClO_4$ in acetonitrile. (d) The photo-charging profile for 5 min under one sun condition. Left shows 2-electrode position for the J_{Ch} measurement mode, where working and counter are connected with the PE and the SE, respectively. (e) Galvanostatic discharging profile at a discharging rate of −0.03 mA cm^{-2}. Right shows 2-electrode position for the galvanostatic discharging mode, where working and counter are connected with the ME and the SE, respectively.

Figure 5.2 (a) Factors influential for photo-charging and galvanostatic discharging performance. (b) The J_{inj} profile as a function of incident light intensity, estimated using the J_{Ch} and J_{Loss}. (c) Discharging rate-dependence of η_Q.

Figure 5.3 (a) Photo-charging current (J_{Ch}) and (b) charge loss current (J_{Loss}) as a function of photon flux. (c) the extracted charge amount (Q_{ext}) from the TiO_2 network at the open circuit state under the illumination

Figure 5.4 PL decay signals detected from Y123 dyed ZrO_2 layer surrounded by different redox mediator: (a) I^-/I_3^-, (b) $Co^{+2/+3}(bpy)_3(PF_6)_{2/3}$, and $Cu^{+/+2}(dmp)_2TFSI_{1/2}$.

Figure 5.5 (a) Light intensity dependent photo-energy conversion/storage efficiency ($\eta_{overall}$) of DSSBs under dim lighting. (b) Light intensity-dependence of $\eta_{IP}'_{peak}$ measured by CIMPS. Note the difference of $\eta_{IP}'_{peak}$ becomes negligible as light intensity decreases. (c, e, g) Temporal photo-charging current (J_{SC}) profiles for 5 min under dim lighting and (d, f, h) following galvanostatic discharging profiles at a discharging rate of −0.03 mA cm^{-2}, with different charge regenerator: (c, d) I^-/I_3^-, (e, f) $Co^{2+/3+}(bpy)_3$, and (g, h) $Cu^{+/2+}(dmp)_2$.

Figure 5.6 (a) Home-made lighting system using white LED, (b) Mesh plate on DSSB, and (c) Commercial desk lighting used for melody-kit operation and cycling test

Figure 5.7 Open circuit voltage monitoring for 100 h in the different discharge mode: (a) discharge mode-1 and (b) discharge mode-2. Galvanostatic discharging profiles of DSSBs with different charge regenerator: (c) I^-/I_3^-, (d) $Co^{2+/3+}(bpy)_3(PF_6)_{2/3}$, and (e) $Cu^{+/2+}(dmp)_2TFSI_{1/2}$ before and after self-discharge test.

Figure 5.8 Charge recombination time (τ_n) in TiO_2 network at the open circuit state as a function of incident photon flux.

Figure 5.9 1 sun photo-charging/discharging cycling test of DSSBs with different charge regenerator: (c) I^-/I_3^-, (d) $Co^{2+/3+}(bpy)_3$, and (e) $Cu^{+/2+}(dmp)_2$.

Figure 5.10 Desk lighting photo-charging/discharging cycling test of DSSBs with different charge regenerator: (c) I^-/I_3^-, (d) $Co^{2+/3+}(bpy)_3$, and (e) $Cu^{+/2+}(dmp)_2$. Inset shows galvanostatic discharging profiles at 1, 50, and 100 cycles. (d) Real photograph taken during the measurement.

Figure 5.11 The plane SEM images of $LiMn_2O_4$ film in a (a) low and (b) high magnification, same with that used for storage electrode in DSSBs. (c) XRD pattern of surface-graphitized $LiMn_2O_4$ powder.

Figure 5.12 (a) The real (η_{IP}', filled symbol) and imaginary (η_{IP}'', blank symbol) parts of photo-charging current efficiency frequency response at 72.8 W m^{-2} of intensity. (b) The light intensity dependent effective charge diffusion coefficient (D_n) of photo-injected electrons during the photo-charging, which is derived from charge transport time.

Figure 5.13 (a) The structure of symmetric cell used for (b) linear sweep voltammetry and (c) impedance analyses for rate constant (k_0) and ionic diffusion coefficient (D) of redox mediators, respectively.

List of Tables

[Chapter 3]

Table 3.1 Summary of photophysical and computational data for **RK-1** – **4** dyes.

Table 3.2. The photovoltaic parameters of **RK** dye-sensitized solar cells according to the active layer thickness.

Table 3.3 Dye loading amount data of each dye according to the soaking time.

Table 3.4. Calculated average exciton lifetimes and corresponding η_{reg} depending on the I^-/I_3^- couple concentration.

[Chapter 4]

Table 4.1 Dye Capacity Data according to the Dyeing Condition.

Table 4.2 Dye capacity for GBS according to gas type.

Table 4.3 Photovoltaic parameters of DSCs according to dyeing conditions.

Table 4.4 Photovoltaic parameters of DSCs prepared with 1 mM of dye solution.

Table 4.5 Fitting Parameters for Estimating Average Exciton Lifetimes from Figure 4.4

Table 4.6 Fitting Parameters from Nyquist Plots and Extracted Charge.

[Chapter 5]

Table 5.1 Hybrid Device Performances depending on the Input Power and Kinetic Parameters of All Charge Regenerators.

Table 5.2 Fitting parameters for estimating average exciton lifetimes in Y123 monolayer on ZrO_2 and regeneration efficiency according to redox mediator.

Table 5.3. Performance Data of DSSBs under Dim Lighting and Light Intensity-Dependence of $\eta_{IP}'_{peak}$, corresponding to Figure 5.5a and 5.5b.

Table 5.4 Incident light intensity and corresponding illuminance according to the number of mesh plate on an illuminometer.

Table 5.5 Kinetic Data as a function of Photon Flux, Measured from the DSSBs with Different Charge Regenerator.

Chapter 1. Introduction

1.1 Motivation

Along with global advances in industry and technology, people are gradually recognizing environmental issues. It is no longer a matter of choice to reduce the consumption of fossil fuels, whose combustion boosts global warming and pollution.[1-2] At present, one of the most pressing challenges is to find alternative ways to natural resources gradually but necessarily. The total solar energy reaching the Earth is approximately 440 exajoules per hour, which is more than the global energy consumption per year.[3] For this reason, photovoltaics (PV), which deals with the immediate conversion of sunlight into electricity, has been a subject of active research and development. The global annual photovoltaic cell production has rapidly increased since 2000 (**Figure 1.1**).

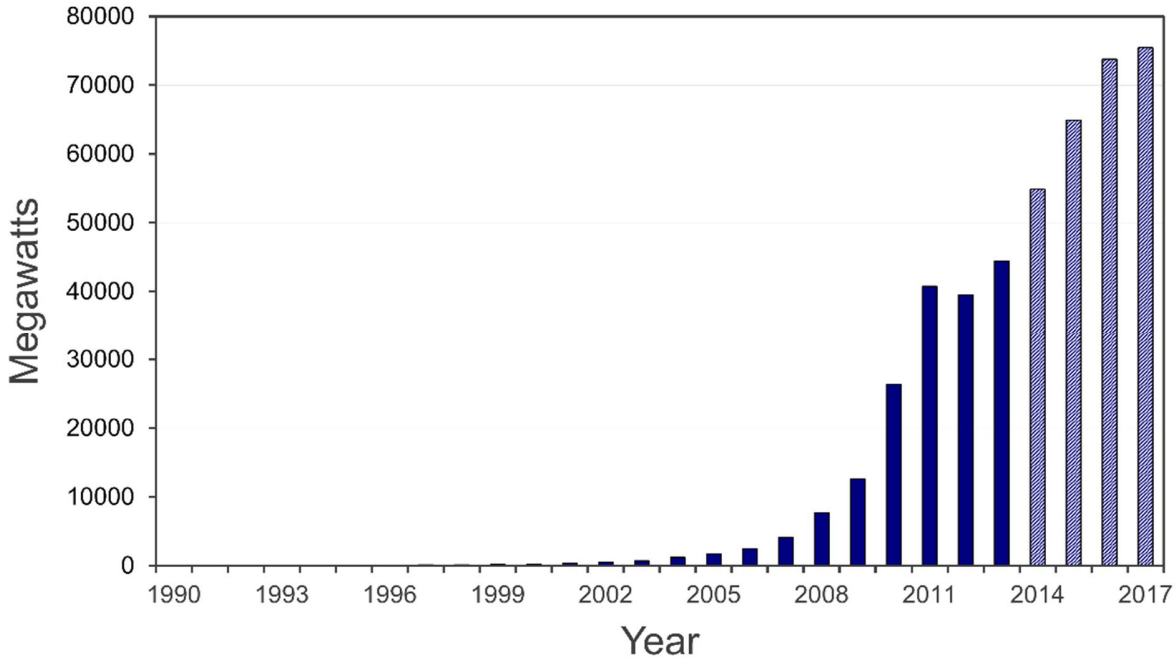

Figure 1.1 World annual solar photovoltaics cell production from 1990 to 2013, with projection to 2017 (Earth Policy Institute - www.earth-policy.org).

Over 80% of commercial PV cells for outdoor deployment are based on the crystalline silicon-based cells, classified as 1st generation PV cells. Although they have been widely employed with proven technology, there are still several technical limitations as below.

i. High cost associated with use of rare materials, purity grade, and electrode thickness
ii. Unstable performance with incident lighting condition
iii. Complicated fabrication process and heavy weight
iv. Power conversion efficiency (PCE) close to the theoretical Shockley-Queisser limit[4]

Such issues have motivated us to study on appropriate alternatives. The 2nd generation PV cells, a variety of thin film solar cells have been rapidly developed, representatively cadmium telluride (CdTe), and copper indium gallium (di)selenide (CIGS). They are characterized by not only high PCE reaching 19.4% with long-term stability, but also low cost due to small quantity of photoactive materials. However, their good performance is not reproducible in module-scale. Most of all, toxicity and rarity of essential elements, such as Cd, In, and Te, are main obstacles for commercialization. During the past decades, a great deal of effort has been dedicated to developing 3rd generation PVs. Depending on the photoactive materials and operational principle, they can be classified into organic (or polymer) solar cells, quantum dot solar cells, dye-sensitized solar cells, and perovskite solar cells. Compared with old-fashioned PVs based on *p-n* junction, they include multi-layer structure in which carriers are exchanged, so not being subject to theoretical Shockley-Queisser limit. It means that they still have plenty of room for improvement. I am convinced that they would be part of solutions to world energy crisis in the near future.

1.2 Dye-sensitized Solar Cells

Initial dye-sensitized solar cells (DSCs) based on a wide band-gap nanostructured semiconducting layer and Ru-complex sensitizers were reported in 1991 by M. Grätzel and B. O'Regan.[5] This triggered a new era of PV research. Subsequently, the PCE has reached 13% under a standard solar condition (AM1.5, 1000 W m^{-2}).[6] DSCs are characterized by transparency, multiple colors, imperviousness to lighting condition, low cost, and simple fabrication. Moreover, they are flexible and lightweight, depending on the substrate.[7-9] Considering such unique features, DSCs are appropriate for building-integrated photovoltaics (BIPV), automotive-integrated photovoltaics (AIPV), portable and indoor power generators.[10-12]

1.2.1 Structure and Working Principle

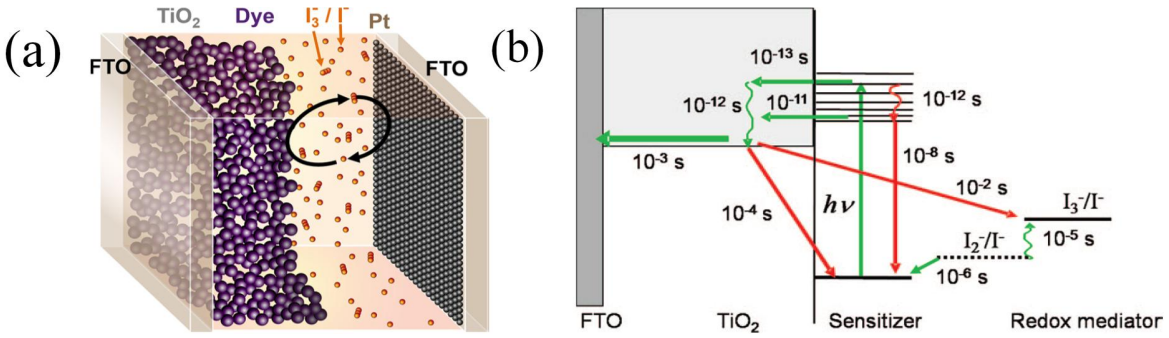

Figure 1.2 (a) Schematic of a typical DSSC and (b) Overview of processes and typical time constants under working conditions (1 sun) in a Ru-based DSC with I^-/I_3^- redox couples.[13-14]

Figure 1.2 shows the structure and working principle of general liquid-type DSCs containing I^-/I_3^- redox mediators.[13-14] Ground-state electrons in the sensitizers are photo-excited from the highest occupied molecular orbital (HOMO) to the lowest unoccupied molecular orbital (LUMO) and quickly injected into the conduction band of TiO_2 (10^{-11}–10^{-13} s). They keep migrating through the TiO_2 nanoparticle network for reaching the collecting contact (10^{-2}–10^{-4} s). The oxidized sensitizers are regenerated by reduced redox mediators, i.e., I^- in the electrolyte (10^{-6}–10^{-10} s). The oxidized redox mediators, i.e., I_3^- in the electrolyte, are reduced again at the catalytic counter-electrode (Eq.1.1), completing the circuit. The maximum open-circuit voltage (V_{OC}) corresponds to the difference between the Fermi level of TiO_2 and the standard potential of redox mediators. More precisely, an intermediate one-electron reaction (Eq.1.2) rather than a two-electron reaction is responsible for dye regeneration.[15]

$$3I^- \leftrightarrow I_3^- + 2e^- \quad (1.1)$$

$$2I^- \rightarrow I_2^{-\cdot} + e^- \quad (1.2)$$

During the operation, a number of charge losses occur through several routes, mainly via charge recombination between the photoinjected electrons and the oxidized dye molecules (10^{-4} s) or oxidized redox mediators, i.e., I_3^- in the electrolyte (10^{-2} s).[16]

1.2.2 Research Strategy

Continuous development of renewable energy technology is definitely important to overcome world energy crisis. Before that, the efficient use of given energy allows us to save a huge amount of surplus energy. Especially, energy consumption in buildings runs to nearly 40% of the whole energy consumption. For this reason, building energy management system (BEMS) industries are expected to grow up to approximately 1.5-billion-dollar scale (**Figure 1.3**), so that indoor environment-customized ubiquitous power supplies are more and more required.[10, 17-18] **Figure 1.3** schematically shows BEMS that requires so many kinds of sensors for monitoring the internal condition and acquiring the information.

Wireless sensors are essential to realize efficient BEMS. In other words, self-rechargeable function is required for them to continuously operate. Photo-energy from indoor lighting is easy to use and sustainable but mostly wasted resource. As mentioned above, photo-energy can be directly converted to electric power through PV system, but all kinds of PV are not suitable for indoor environment. I suggest the conditions of indoor-customized PV as below.

i. Efficient indoor light harvesting and conversion
ii. Imperviousness to incident light intensity and angle
iii. Aesthetic impression
iv. Being installable wherever needed
v. Flexibly controllable V_{OC}

For following reasons, DSCs definitely meet such requirements. (1) Donor-π-acceptor structured organic sensitizers provide intrinsically high molar extinction coefficient and (2) their absorption abilities, such as absorption range and initial transition energy, are easily controllable through molecular engineering. (3) In operational mechanism of DSCs, charge recombination rate is much less under low light intensity, leading

to efficient photocurrent generation. (4) Transparent semiconducting layers that have been mainly used as an electron transport layer in DSCs, representatively TiO_2, facilitate low sensitivity to lighting condition because of mesoporous nanostructure. (5) Along with the development of flexible conducting substrate, many bendable DSCs have been reported with not much deteriorated efficiency. Moreover, (6) V_{OC} of DSCs is easily controllable compared with other types of PV by controlling charge regenerator in the electrolyte. Recently, some groups demonstrated that DSCs provided much higher PCE than silicon-based solar cells under low light intensity. These works strongly suggest the potential of DSCs as indoor-customized PV.

More practical DSCs can be developed by using thin mesoporous TiO_2 film rather than thick one. The thinner the TiO_2 film is used, the higher the transparency and mechanical durability are achievable, as shown in **Figure 1.4**. It has been generalized that too thin TiO_2 film not afford the sufficient dye amount and thereby deliver the poor device performance. However, most precedent studies on DSCs have only focused on the outdoor performance (ca. 2.7×10^{21} m^{-2} s^{-1} of photon flux at 1 sun, 250000 lux). Considering the weak intensity of indoor lighting (ca. 1.7×10^{18} m^{-2} s^{-1} of photon flux at living room, 200 lux), thin mesoporous TiO_2 film is capable of sufficient dye amount for indoor power conversion (ca. 9.6×10^{19} m^{-2} of Y123 dye at 1.8-μm). For those reasons, thin TiO_2 film-based DSCs must be promising future research theme to realize indoor-customized PV.

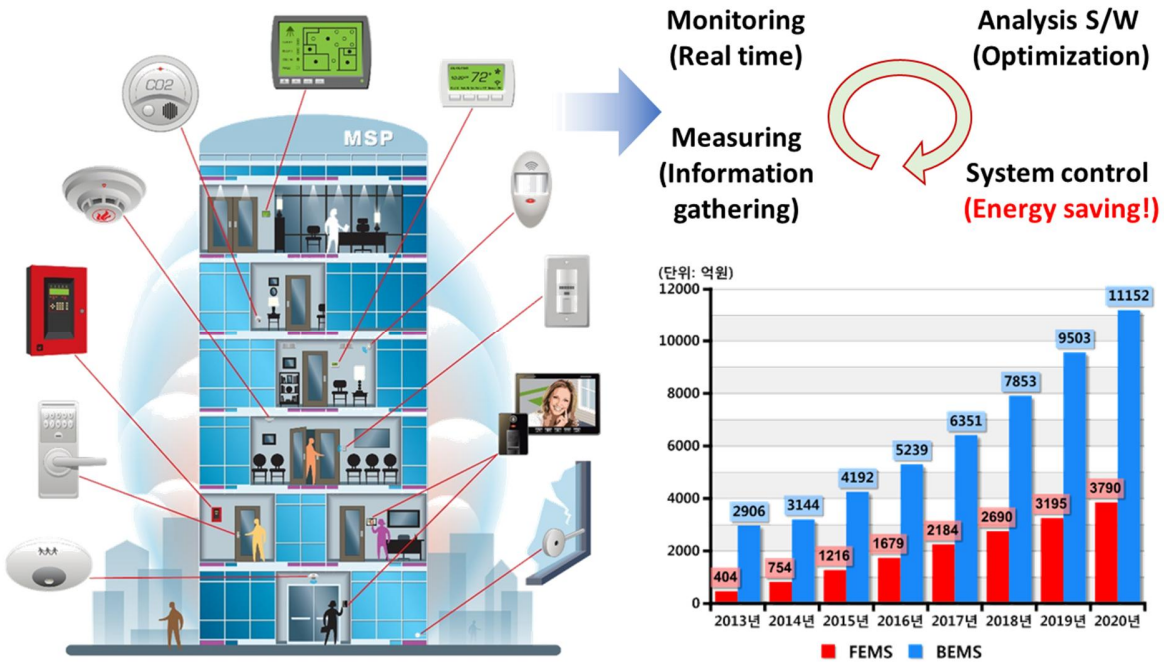

Figure 1.3 Schematic of a building energy management system (BEMS). A variety of sensors are required to operate the whole system. Along with increasing energy crisis recognition, BEMS industries are expected to rapidly grow.

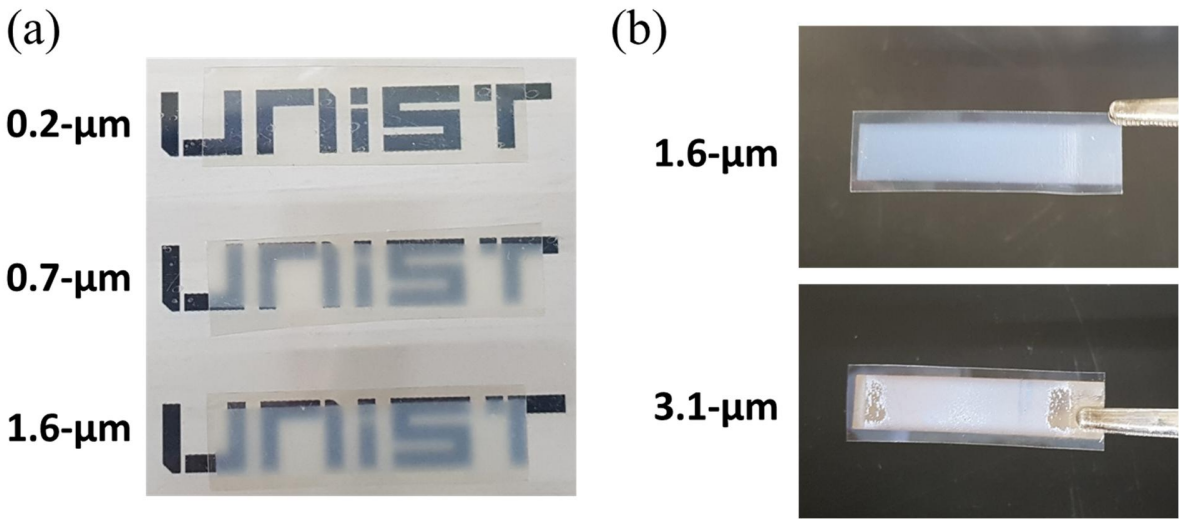

Figure 1.4 TiO_2 film thickness dependent (a) transparency and (b) film detachment after bending test. It is noteworthy that 1.6-μm TiO_2 film never detached after repeated bending test.

1.3 Hybrid Photo-rechargeable Systems

The intermittent availability is the main drawback of solar energy, so being not compatible with actual energy demand (**Figure 1.5**). Energy storage system (EES) has been combined with photo-energy converter to solve such problem. As shown in Figure 1.4, surplus solar power produced during peak hours gets stored in EES and it can be used when energy demand increases. According to the connection type between PV and EES, they can be divided two groups: (1) separated system in which PV and EES are wire-connected and (2) all-in-one system in which PV and EES share the ions across the membrane (**Figure 1.6**). Separated systems suffer from energy loss due to wire-resistance, over-charging problem, and inefficient use of a space. Crucially, they require multi-connection or module production for applying to indoor environment because of low J_{SC} from the unit PV cell. In contrast, all-in-one systems not only have no concerns about such problems but also are applicable to indoor environment even in a single unit cell.

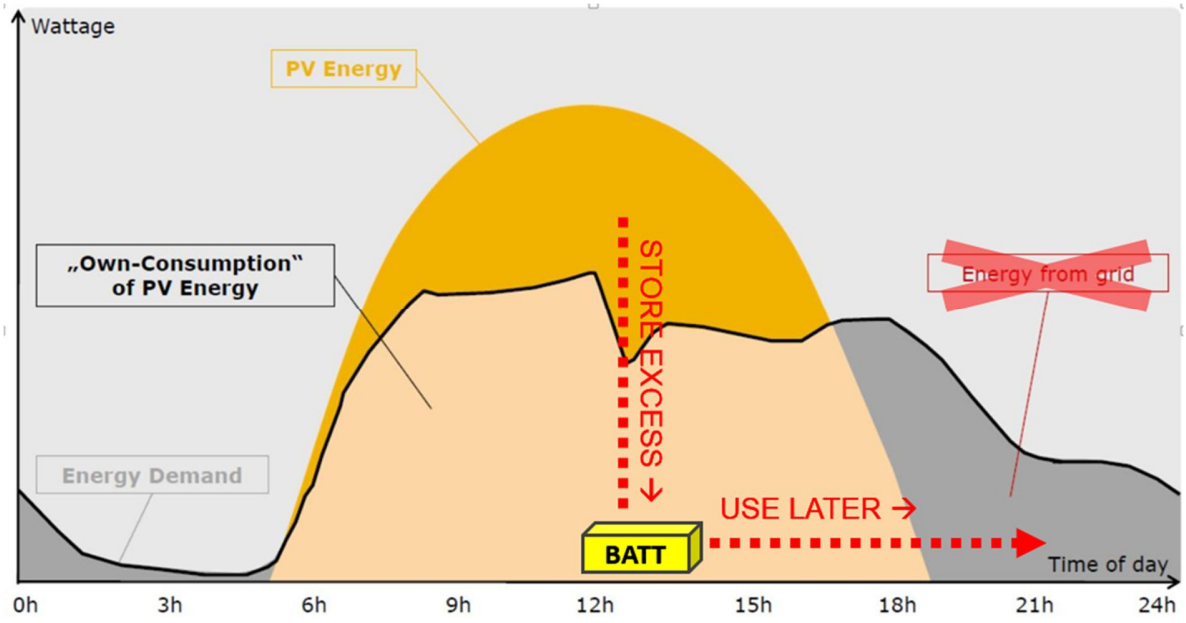

Figure 1.5 Time dependent PV energy production and energy demand curves. Excess energy (bright orange) is stored in a battery for evening use.

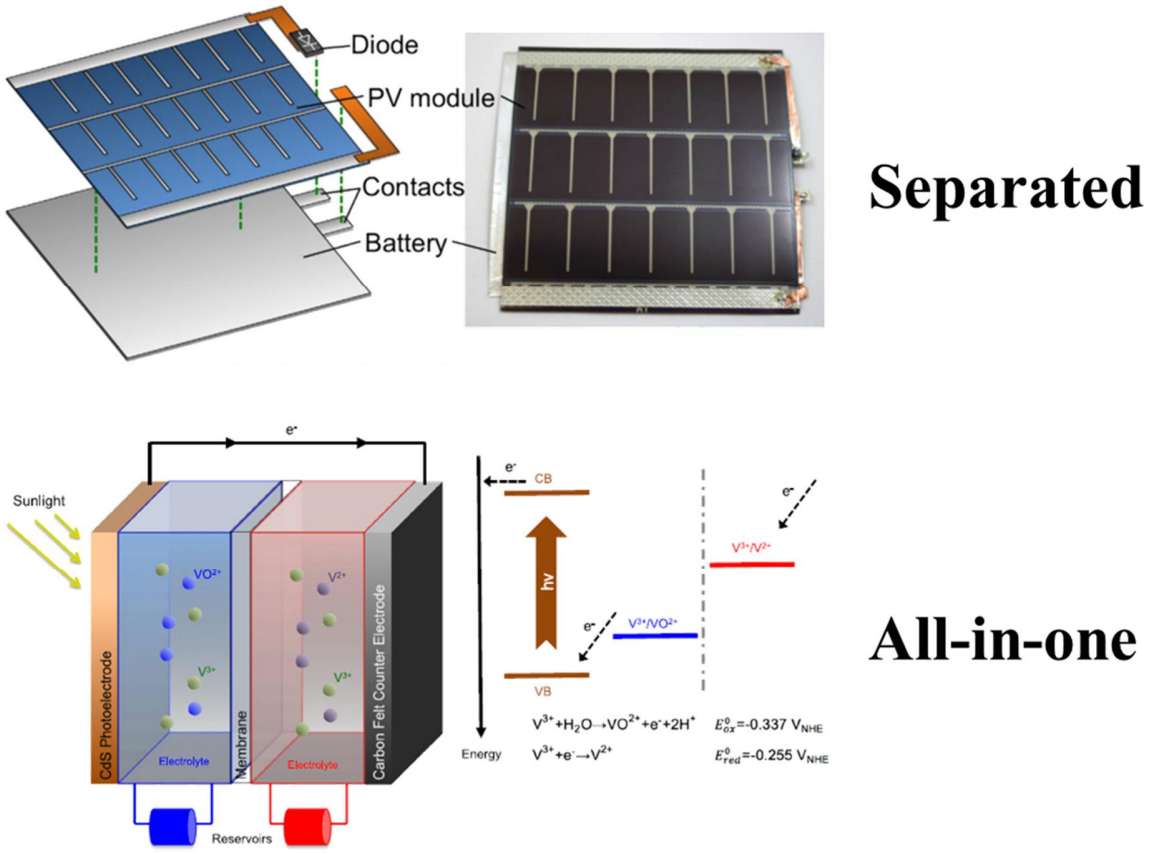

Figure 1.6 The comparison of two types of photo-rechargeable systems (separated[19] and all-in-one[20]).

For photo-energy storage, supercapacitors have been mainly employed because of their high power density.[21-31] However, they have intrinsic limitations such as low energy density and fast self-discharge.[32] Such problems can be overcome by employing kinds of batteries. There have been lots of studies on photo-rechargeable batteries since first report by Hodes *et al.* in 1976.[33] In 2002, Hauch and Orel *et al.* suggested first DSC-combined photo-rechargeable battery with WO_3 as storage material and I^-/I_3^- redox mediator.[34] They highlighted that this new concept of device had potential as indoor-customized device because of higher performance under low light intensity and electrochromic coloration. Following that, many groups have optimized DSC-combined photo-rechargeable batteries using various storage materials such as modified WO_3, conducting polymers, and solution dissolved redox active species.

Nevertheless, few groups have used general active materials for lithium ion battery (LIB) as storage material. This is attributed to energy level mismatch between active materials for LIB and photo-electrodes for DSCs. **Figure 1.7** shows Li^+ ion active potentials and record performances of reported cathode materials.[35] All materials have too high or low Li^+ ion active potential to be combined with DSCs. Based

on conduction band edge of TiO_2 (ca. −0.5 V), storage materials with higher Li^+ ion active potential cannot accept photo-charge from TiO_2 photo-electrode and ones with too lower Li^+ ion active potential cannot deliver enough output voltage that is defined as redox potential gap between charge acceptor in PV part and storage material. Instead, some groups proposed multi-connected PV pack to photo-charge LIB, in which PV pack and LIB were separated and wire-connected.[36] Aside from those, other groups suggested photo-assisted rechargeable system, in which photo-energy was used to reduce external voltage for charging.[37-39]

Most studies on photo-rechargeable system so far has focused on high performance under 1 sun condition. More strategic studies should be proceeded to boost the realization of practical photo-rechargeable system as follows: (1) Selective and focused studies should be proceeded considering the application place. As an example, for the devices that will be used inside the building, crucial characteristic parameter would be output voltage rather than capacity. (2) Storage materials with fused characteristics should be developed in order to achieve both energy and power density. For example, supercapacitors can be improved by integrating with organic radical batteries, resulting in a fast charging as well as high capacity. As a consequence, photo-rechargeable systems can be powerful electronics for daily life.

Cathode	Voltage (V)	Specific capacity (mAh g^{-1})	Specific energy (Wh kg^{-1})
$LiCoO_2$	3.9	130	507
$LiMn_2O_4$	3.95	148	585
FeF_3	2.74	712	1,951
MnF_3	2.65	719	1,905
CuF_2	3.55	528	1,874
CoF_2	2.86	553	1,578
NiF_2	2.96	554	1,435
CuO	2.25	674	1,517
CoO	1.80	715	1,287
NiO	1.81	718	1,096
RuO_2	2.18	806	1,455
CrO_3	2.02	1,608	2,297
MoO_3	1.75	1,117	1,521
V_2O_5	1.44	1,474	1,533
$LiFePO_4$	3.4	170	578
$LiMnPO_4$	4.1	171	701
$LiCoPO_4$	4.8	167	802
$LiNiPO_4$	5.1	167	852
Li_2FeSiO_4	3.3	328	1,082
Li_2MnSiO_4	4.0	333	1,332
Li_2CoSiO_4	4.3	325	1,397
Li_2NiSiO_4	4.7	326	1,530

Figure 1.7 Li^+ ion active potentials and performances of cathode materials for lithium ion battery.[35]

REFERENCE

1. Goncalves, L. M.; Bermudez, V. D.; Ribeiro, H. A.; Mendes, A. M., Dye-sensitized solar cells: A safe bet for the future. *Energy Environ. Sci.* **2008,** *1* (6), 655-667.

2. OECD-OCDE, *Medium-Term Gas Market Report 2015*. OECD Publishing; International Energy Agency: Paris, France, 2015.

3. Goldemberg, J., *World Energy Assessment: Energy and the challenge of sustainability*. United Nations Pubns: New York, USA, 2000.

4. Shockley, W.; Queisser, H. J., Detailed balance limit of efficiency of p□n junction solar cells. *J. Appl. Phys.* **1961,** *32* (3), 510-519.

5. Oregan, B.; Gratzel, M., A Low-Cost, High-Efficiency Solar-Cell Based on Dye-Sensitized Colloidal Tio2 Films. *Nature* **1991,** *353* (6346), 737-740.

6. Mathew, S.; Yella, A.; Gao, P.; Humphry-Baker, R.; Curchod, B. F. E.; Ashari-Astani, N.; Tavernelli, I.; Rothlisberger, U.; Nazeeruddin, M. K.; Gratzel, M., Dye-sensitized solar cells with 13% efficiency achieved through the molecular engineering of porphyrin sensitizers. *Nat. Chem.* **2014,** *6* (3), 242-247.

7. Brown, T. M.; De Rossi, F.; Di Giacomo, F.; Mincuzzi, G.; Zardetto, V.; Reale, A.; Di Carlo, A., Progress in flexible dye solar cell materials, processes and devices. *J. Mater. Chem. A* **2014,** *2* (28), 10788-10817.

8. Pugliese, D. New insights in Dye-sensitized Solar Cells: novel nanostructured photoanodes, metal-free dye, quasi-solid electrolytes and physics-based modeling. PhD Thesis, Politecnico di Torino, Italy, 2014.

9. Gratzel, M., Solar energy conversion by dye-sensitized photovoltaic cells. *Inorg. Chem.* **2005,** *44* (20), 6841-6851.

10. Nasiri, A.; Zabalawi, S. A.; Mandic, G., Indoor Power Harvesting Using Photovoltaic Cells for Low-Power Applications. *IEEE Trans. Ind. Electron.* **2009,** *56* (11), 4502-4509.

11. SENG, S. D. Fabrication and Optimization of Flexible Dye Sensitized Solar Cells. PhD Thesis, National University of Singapore, Singapore, 2013.

12. Fakharuddin, A.; Jose, R.; Brown, T. M.; Fabregat-Santiago, F.; Bisquert, J., A perspective on the production of dye-sensitized solar modules. *Energy Environ. Sci.* **2014,** *7* (12), 3952-3981.

13. Hagfeldt, A.; Boschloo, G.; Sun, L. C.; Kloo, L.; Pettersson, H., Dye-Sensitized Solar Cells. *Chem. Rev.* **2010,** *110* (11), 6595-6663.

14. Roy-Mayhew, J. D.; Aksay, I. A., Graphene materials and their use in dye-sensitized solar cells. *Chem. Rev.* **2014,** *114* (12), 6323-6348.

15. Boschloo, G.; Hagfeldt, A., Characteristics of the Iodide/Triiodide Redox Mediator in Dye-Sensitized Solar Cells. *Acc. Chem. Res.* **2009,** *42* (11), 1819-1826.

16. Barnes, P. R. F.; Miettunen, K.; Li, X. E.; Anderson, A. Y.; Bessho, T.; Gratzel, M.; O'Regan, B. C., Interpretation of Optoelectronic Transient and Charge Extraction Measurements in Dye-Sensitized Solar Cells. *Adv. Mater.* **2013,** *25* (13), 1881-1922.

17. Helal, S.; Mann, W.; El-Zabadani, H.; King, J.; Kaddoura, Y.; Jansen, E., The gator tech smart house: A programmable pervasive space. *Computer* **2005,** *38* (3), 50-60.

18. Haight, R.; Haensch, W.; Friedman, D., Solar-powering the Internet of Things. *Science* **2016,** *353* (6295), 124-125.

19. Ostfeld, A. E.; Gaikwad, A. M.; Khan, Y.; Arias, A. C., High-performance flexible energy storage and harvesting system for wearable electronics. *Sci. Rep.* **2016,** *6*, 26122.

20. Azevedo, J.; Seipp, T.; Burfeind, J.; Sousa, C.; Bentien, A.; Araújo, J. P.; Mendes, A., Unbiased solar energy storage: Photoelectrochemical redox flow battery. *Nano Energy* **2016,** *22*, 396-405.

21. Murakami, T. N.; Kawashima, N.; Miyasaka, T., A high-voltage dye-sensitized photocapacitor of a three-electrode system. *Chem. Commun.* **2005,** (26), 3346-8.

22. Hsu, C.-Y.; Chen, H.-W.; Lee, K.-M.; Hu, C.-W.; Ho, K.-C., A dye-sensitized photo-supercapacitor based on PProDOT-Et2 thick films. *J. Power Sources* **2010,** *195* (18), 6232-6238.

23. Bae, J.; Park, Y. J.; Lee, M.; Cha, S. N.; Choi, Y. J.; Lee, C. S.; Kim, J. M.; Wang, Z. L., Single-fiber-based hybridization of energy converters and storage units using graphene as electrodes. *Adv. Mater.* **2011,** *23* (30), 3446-3449.

24. Wee, G.; Salim, T.; Lam, Y. M.; Mhaisalkar, S. G.; Srinivasan, M., Printable photo-supercapacitor using single-walled carbon nanotubes. *Energy Environ. Sci.* **2011,** *4* (2), 413-416.

25. Chen, T.; Qiu, L.; Yang, Z.; Cai, Z.; Ren, J.; Li, H.; Lin, H.; Sun, X.; Peng, H., An Integrated "energy wire" for both photoelectric conversion and energy storage. *Angew. Chem. Int. Ed.* **2012,** *51* (48), 11977-80.

26. Sun, H.; You, X.; Deng, J.; Chen, X.; Yang, Z.; Chen, P.; Fang, X.; Peng, H., A twisted wire□ shaped dual□function energy device for photoelectric conversion and electrochemical storage. *Angew. Chem., Int. Ed.* **2014,** *53* (26), 6664-6668.

27. Xu, X.; Li, S.; Zhang, H.; Shen, Y.; Zakeeruddin, S. M.; Graetzel, M.; Cheng, Y.-B.; Wang, M., A power pack based on organometallic perovskite solar cell and supercapacitor. *ACS Nano* **2015,** *9* (2), 1782-1787.

28. Xue, Y.; Ding, Y.; Niu, J.; Xia, Z.; Roy, A.; Chen, H.; Qu, J.; Wang, Z. L.; Dai, L., Rationally designed graphene-nanotube 3D architectures with a seamless nodal junction for efficient energy conversion and storage. *Sci. Adv.* **2015,** *1* (8), e1400198.

29. Wen, Z.; Yeh, M.-H.; Guo, H.; Wang, J.; Zi, Y.; Xu, W.; Deng, J.; Zhu, L.; Wang, X.; Hu, C.; Zhu, L.; Sun, X.; Wang, Z. L., Self-powered textile for wearable electronics by hybridizing fiber-shaped nanogenerators, solar cells, and supercapacitors. *Sci. Adv.* **2016,** *2* (10), e1600097.

30. Scalia, A.; Bella, F.; Lamberti, A.; Bianco, S.; Gerbaldi, C.; Tresso, E.; Pirri, C. F., A flexible and portable powerpack by solid-state supercapacitor and dye-sensitized solar cell integration. *J. Power Sources* **2017,** *359*, 311-321.

31. Liu, R.; Wang, J.; Sun, T.; Wang, M.; Wu, C.; Zou, H.; Song, T.; Zhang, X.; Lee, S.-T.; Wang, Z. L., Silicon Nanowire/Polymer Hybrid Solar Cell-Supercapacitor: A Self-Charging Power Unit with a Total Efficiency of 10.5%. *Nano Lett.* **2017,** *17*, 4240-4247.

32. Andreas, H. A., Self-Discharge in Electrochemical Capacitors: A Perspective Article. *J. Electrochem. Soc.* **2015,** *162* (5), A5047-A5053.

33. Hodes, G.; Manassen, J.; Cahen, D., Photoelectrochemical energy conversion and storage using polycrystalline chalcogenide electrodes. *Nature* **1976,** *261* (5559), 403-404.

34. Hauch, A.; Georg, A.; Krašovec, U. O.; Orel, B., Photovoltaically self-charging battery. *J. Electrochem. Soc.* **2002,** *149* (9), A1208-A1211.

35. Hayner, C. M.; Zhao, X.; Kung, H. H., Materials for rechargeable lithium-ion batteries. *Annu. Rev. Chem. Biomol. Eng.* **2012,** *3*, 445-471.

36. Xu, J.; Chen, Y.; Dai, L., Efficiently photo-charging lithium-ion battery by perovskite solar cell. *Nat. Commun.* **2015,** *6*, 8103.

37. Yu, M.; McCulloch, W. D.; Beauchamp, D. R.; Huang, Z.; Ren, X.; Wu, Y., Aqueous lithium–iodine solar flow battery for the simultaneous conversion and storage of solar energy. *J. Am. Chem. Soc.* **2015,** *137* (26), 8332-8335.

38. Li, Q.; Li, N.; Liu, Y.; Wang, Y.; Zhou, H., High□Safety and Low□Cost Photoassisted Chargeable Aqueous Sodium□Ion Batteries with 90% Input Electric Energy Savings. *Adv. Energy Mater.* **2016,** *6* (18), 1600632.

39. Liao, S.; Shi, J.; Ding, C.; Liu, M.; Xiong, F.; Wang, N.; Chen, J.; Li, C., Photoelectrochemical regeneration of all vanadium redox species for construction of a solar rechargeable flow cell. *J. Energy Chem.* **2018,** *27* (1), 278-282.

Chapter 2. Experimental Methods

2.1 DSCs Fabrication

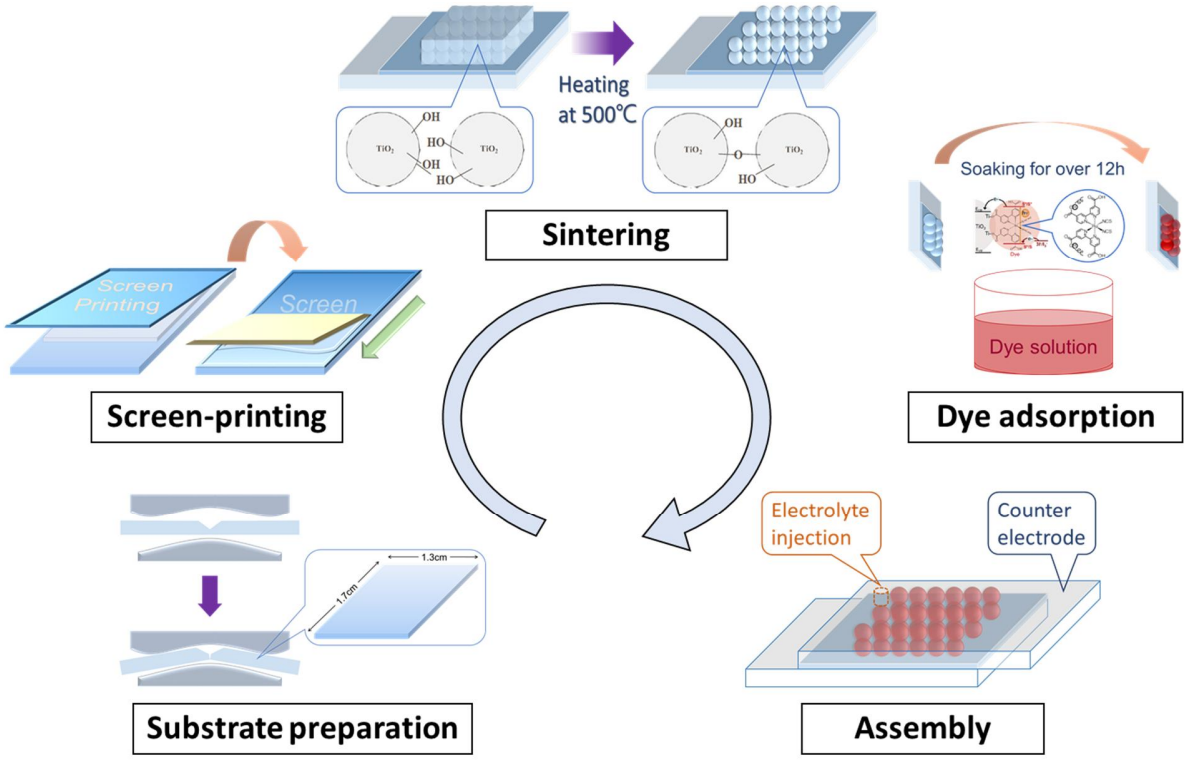

Figure 2.1 Dye-sensitized solar cell fabrication process.

The whole DSC fabrication process is shown in **Figure 2.1**. Fluorine-doped tin oxide (FTO, Nippon Sheet Glass Co., Ltd.) glass was used as substrate for all electrodes. First, FTO glass was ultrasonic-cleaned in acetone, ethanol, and DI water for 10 min, in that order. Cleaned FTO glass was immersed in an aqueous 0.04 M $TiCl_4$ solution at 70 °C for 30 min to form a compact TiO_2 layer that is helpful for interfacial adhesion force at FTO/mesoporous TiO_2 layer interface. A mesoporous TiO_2 double layer was prepared by screen-printing commercial TiO_2 paste (Ti-Nanoxide MC/SP, Solaronix SA or DONGJIN SEMICHEM CO., LTD.) and light scattering TiO_2 paste (Ti-Nanoxide R/SP, Solaronix SA) on the compact TiO_2 layer, followed by sequential heating at 150 °C for 10 min, 325 °C for 5 min, 327 °C for 5 min, 450 °C for 15 min, and 500 °C for 30 min. To control the TiO_2 film thickness, the number of screen printing was controlled

using commercial mask (MESH S/T250, Emulsion 12-μm), corresponding to 1.8-μm for one time and 3.5-μm for two times printing (Thickness was slightly different according to used paste). For a thicker mesoporous TiO_2 layer, another mask (MESH S/T150, Emulsion 50-μm) was used, which provided a 5.1-μm film for one time of printing. The area of the photo electrode was 0.16 cm^2 (0.4×0.4 cm^2) and the film thickness was measured by a surface profiler (P6, KLA-Tencor Corporation). To find the film thickness, nine samples per printing condition were measured and averaged. 2D surface scanning profiles show overall thickness of TiO_2 layer as a function of the number of printing (**Figure 2.2**). The mesoporous TiO_2 double layer was immersed again in aqueous 0.04 M $TiCl_4$ solution at 70 °C for 30 min and heated at 500 °C for 30 min. After naturally cooling to 80 °C, the TiO_2 electrodes were immersed in the dye solution (0.2 mM) and maintained at room temperature under a dark condition for 180 min for the 1.8-μm active layer and 210 min for the 3.5-μm active layer (refer to each chapter for exact information).

For the counter-electrode, the FTO glass was drilled a hole for the electrolyte injection later and ultrasonic-cleaned the same with the photo electrode. Two kinds of catalytic layers were employed, platinum (Pt) and poly(3,4-ethylenedioxythiophene) (PEDOT).[1-2] For the former, the prepared FTO glass was coated with a H_2PtCl_6 solution (0.01 M $H_2PtCl_6 \cdot 6H_2O$ in ethanol) by brushing and heated at 400 °C for 15 min. For the latter, the electrodeposition was carried out applying a constant current (+0.5 mA) for 30 s in an acetonitrile dispersion of EDOT containing 0.01 M EDOT (97%, Aldrich) and 0.1 M $LiClO_4$ (99.99% trace metals basis, Aldrich).

Finally, two electrodes were assembled into a sandwich structure and sealed using a 25-μm Surlyn® resin (Meltonix 1170-60, Solaronix SA) at 110 °C. The space between the photo and counter-electrodes was filled with the electrolyte containing redox active species by a vacuum back-filling force and subsequently sealed using a cover glass (Marlenfeld GmbH & Co.). Four kinds of charge regenerator are introduced in this thesis, such as I^-/I_3^-, $Co^{+2/+3}(bpy)_3$, and $Cu^{+/+2}(dmp)_2$, and Cs_2SnI_6 perovskite (refer to each chapter for exact information).[3-5]

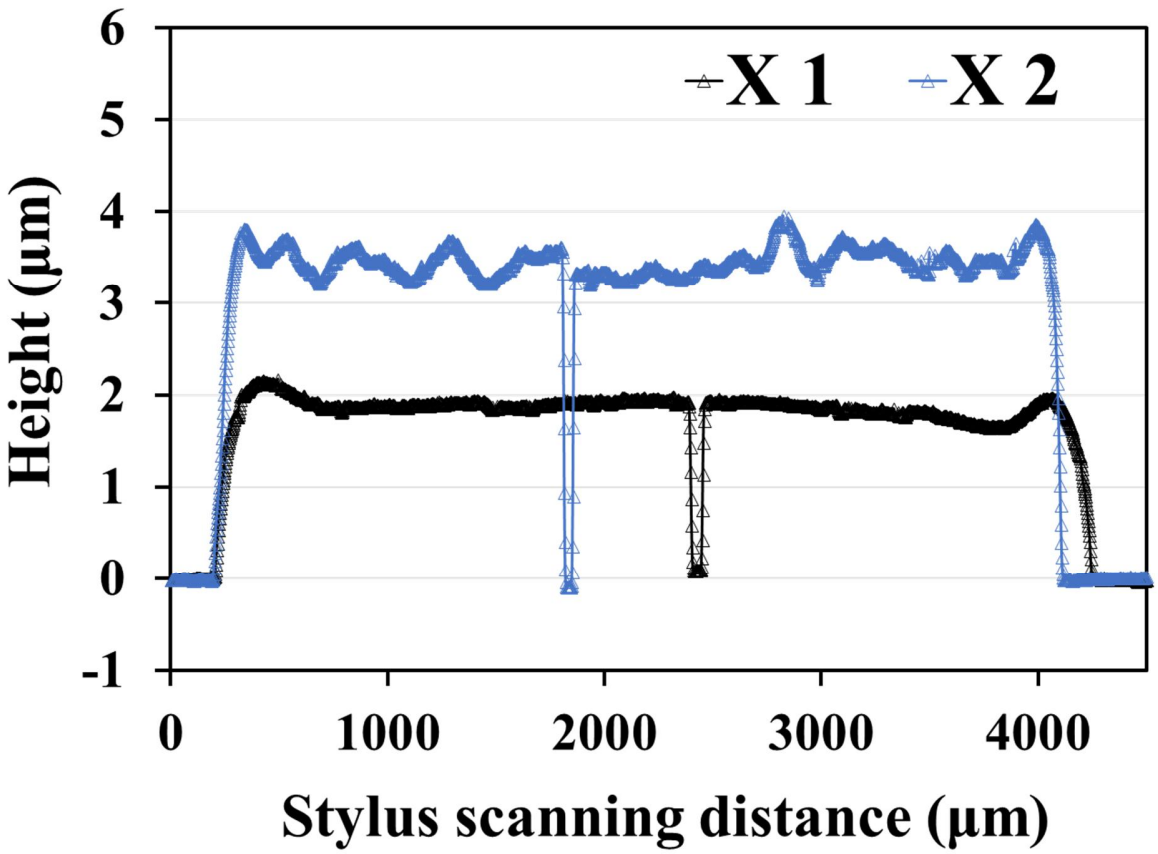

Figure 2.2 2D surface scanning profiles of TiO_2 layer according to the number of printing. An abysmal ravine near mid-point corresponds to scratching trace for the measurement. All the samples were measured after sintering. It is noted that thickness was slightly different depending on the paste.

2.2 Characterization Techniques

The appropriate evaluation of DSCs with different conditions allows a comprehensive understanding of device behavior. There are various powerful tools for characterization of DSCs from simple current-voltage measurement to small perturbation techniques. Combining these, we can expect the internal charge kinetics in a fine time scale.

2.2.1 Current-Voltage (J-V) Measurement

Under illumination, the photocurrent is determined by subtracting recombination current (I_{rec}) from the photo-charge injection current (I_{inj}). I_{rec} that flows in the opposite direction to photocurrent depends on the applied voltage as shown in Eq.2.1:[6-7]

$$I = I_{inj} - I_{rec} = I_{inj} - I_0(e^{\frac{qV}{nk_BT}} - 1) \quad (2.1)$$

Where I_0 is the diode reverse saturation current (called dark current), q is the elementary charge, V is the applied voltage, n is the ideality factor, k_B is the Boltzmann constant, and T is the absolute temperature. The open circuit potential (V_{OC}) is measured when I_{inj} and I_{rec} are the same ($I = 0$), which results in Eq.2.2:

$$V_{OC} = \frac{nk_BT}{q}\ln(\frac{I_{inj}}{I_0} + 1) \cong \frac{nk_BT}{q}\ln(\frac{I_{inj}}{I_0}) \quad (2.2)$$

Eq.2.2 shows V_{OC} is logarithmically proportional to incident light intensity. The short-circuit current (I_{SC}) is measured when the applied voltage is zero ($V = 0$), resulting in Eq.2.3:

$$I_{SC} = I_{inj} \quad (2.3)$$

Eq.2.3 shows I_{SC} is linearly proportional to incident light intensity. These relations between device parameters and light intensity agree with the experimental results as well.

Figure 2.3 shows typical J-V curve of a solar cell. The power conversion efficiency (η_{PCE}) of solar cell is determined by the ratio of maximum power density (P_{max}) to the incident light intensity (P_{in}). The concept of fill factor (*FF*) that is defined by the ratio of P_{max} to the product of I_{SC} and V_{OC} is used for simple expression. As a result, η_{PCE} can be expressed as follows:[8]

$$\eta_{PCE} = \frac{P_{max}}{P_{in}} = \frac{I_{max}V_{max}}{P_{in}} = \frac{I_{SC}V_{SC}FF}{P_{in}} \quad (2.4)$$

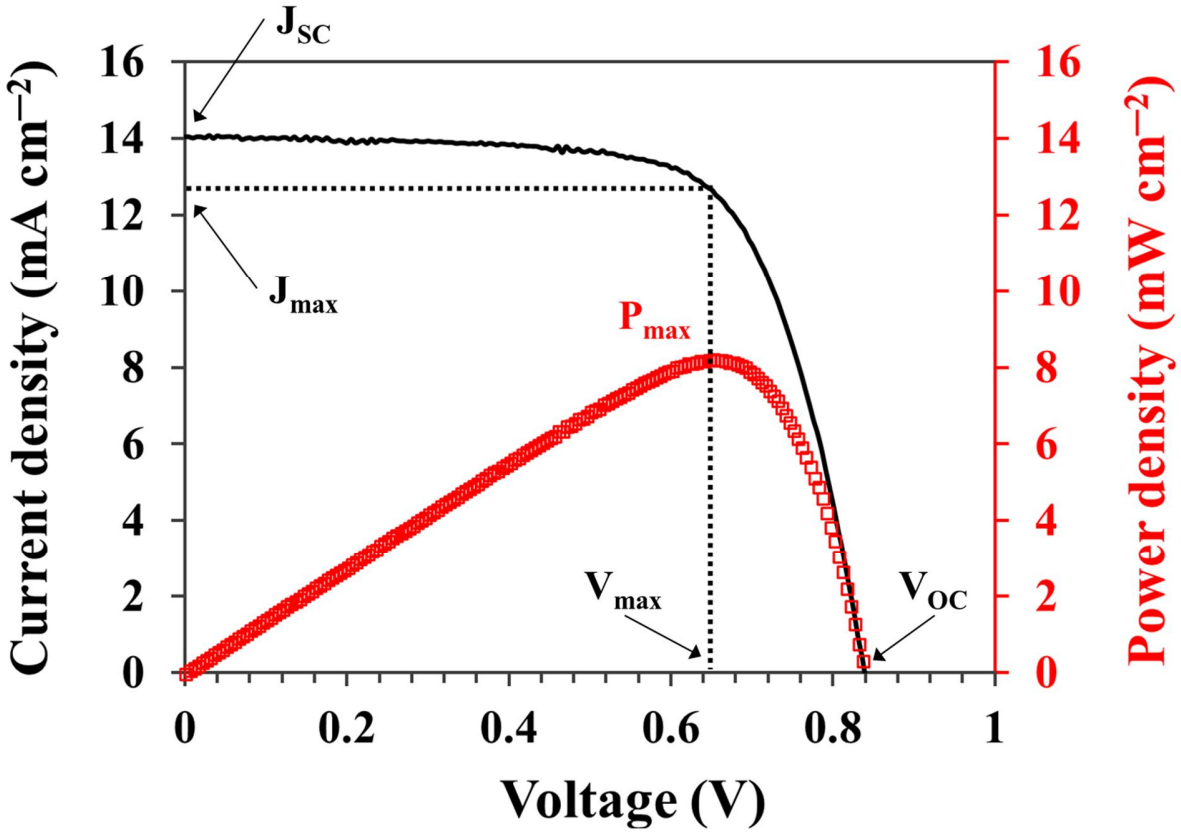

Figure 2.3 Typical current density-voltage curve from DSCs with corresponding power density.

2.2.2 Incident Photon-to-Current Conversion Efficiency (IPCE)

The incident photon-to-current conversion efficiency (IPCE), also called the external quantum efficiency (EQE), is an essential characterization method for the solar cells. It provides spectral photocurrent response at a single wavelength. If the incident light intensity at each wavelength is known (generally calibrated using reference cell), the IPCE value at a given wavelength can be calculated as follows.[9]

$$IPCE(\lambda) = \frac{1240}{\lambda}\frac{J_{SC}(\lambda)}{P_{in}(\lambda)} = \eta_{lh}\,\eta_{inj}\,\eta_{cc}\,\eta_{reg} \qquad (2.5)$$

Where λ is the wavelength, $J_{SC}(\lambda)$ is the photocurrent density at each wavelength, $P_{in}(\lambda)$ is the incident light intensity at each wavelength, η_{lh} is the light harvesting efficiency, η_{inj} is the photo-charge injection efficiency, η_{cc} is the charge collection efficiency, and η_{reg} is the charge regeneration efficiency. As shown in Eq.2.5, IPCE corresponds to product of four factors (η_{lh}, η_{inj}, η_{cc}, and η_{reg}) that is associated with temporal charge kinetics for photocurrent generation since photo-excitation of sensitizer (**Figure 2.4a**).[10-11]

There are two methods for IPCE measurement according to existence of light chopper, divided to the alternative current (AC) mode and the direct current (DC) mode. **Figure 2.4b** shows chopping frequency dependent IPCE spectra measured in the AC mode. The IPCE spectrum strongly depends on the chopping frequency of the monochromatic light. For DSCs, photo-generated charge collection is remarkably slow compared to other types of PVs ranging from milliseconds to seconds. This can be explained by trapping/de-trapping processes of photo-injected electrons in nanostructured TiO_2 network.[12-13] Considering the severe electron trapping phenomena in DSCs, IPCE of DSCs should be measured in specific conditions as below:[9, 14-15]

i. DC mode with sufficiently high photon flux (over 1.0×10^{20} m^{-2} s^{-1})

ii. AC mode at sufficiently low chopping frequency (below 2 Hz) with background lighting

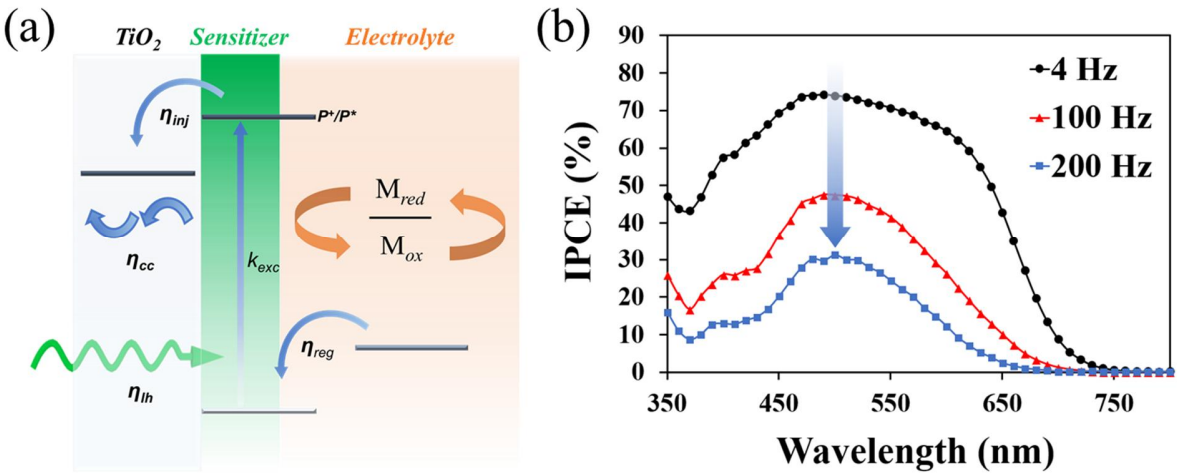

Figure 2.4 (a) Charge behavior (blue arrow for electron and orange arrow for redox mediator) for photocurrent generation since photo-excitation of sensitizer. (b) IPCE spectra of DSC based on RK-3 dye as a function of chopping frequency in AC mode.

2.2.3 Controlled Intensity Modulated Photo Spectroscopy (CIMPS)

Contrary to steady-state methods, the small chopped illumination methods drive the system out of equilibrium and the measurement during transient response provides information about internal charge kinetics on different time scales. Intensity modulated photocurrent spectroscopy (IMPS) and intensity modulated photovoltage spectroscopy (IMVS) are very useful tools to study photo-generated carrier behavior in DSCs. IMPS method measures the transient photocurrent response to a small chopped illumination with variable frequency.[6] IMVS method uses the same chopped illumination but measures the transient photovoltage response, i.e. the difference between Fermi level in the dark (E_F) and the quasi-Fermi level under illumination ($_nE_F$).[16] IMPS provides information about the electron diffusion and back reaction in TiO_2 network under short circuit state, while IMVS shows the electron lifetime under open circuit state.

Compared to traditional IMPS/VS techniques, controlled intensity modulated photo spectroscopy (CIMPS) correlates photocurrent or photovoltage responses from the cell with actual light intensity signal (P_{act}) measured by means of a photo-sensor near the cell. P_{act} can be stabilized by a continuous feedback from the photo-sensor. **Figure 2.5** shows a circuit diagram for CIMPS system and real photograph during measurement. For that reason, CIMPS is able to evaluate photo-response with much higher accuracy. Using CIMPS technique, light chopping frequency response of photocurrent efficiency (η_{IP}) and photovoltage efficiency (η_{UP}) can be measured, which are corresponding to the ratio of photocurrent (I_{SC}) to incident light intensity (P_{in}) and the ratio of photovoltage (V_{OC}) to incident light intensity (P_{in}), respectively. The AC amplitude is generally selected ~10% of light source potentiostat.

$$\eta_{IP} = I_{SC}/P_{in} \tag{2.6}$$

$$\eta_{UP} = V_{OC}/P_{in} \tag{2.7}$$

Taking the inverse of the cutoff angular frequency ($\tau = 1/\omega_{cutoff} = 1/2\pi f_{cutoff}$) in the imiginary part of CIMPS spectra, time constants for charge transport (τ_{trans}) and charge recombination (τ_{rec}) can be estimated. It is noted that such τ_{trans} and τ_{rec} derive from the short circuit and the open circuit states, respectively. Using the τ_{trans} and τ_{rec}, the effective diffusion coefficient (D_n) and collection efficiency (η_{CC}) of the photo-injected electron can be determined as below.[17]

$$D_n = \omega_{cutoff,IMPS}\, L^2/\xi \tag{2.8}$$

$$\eta_{CC} = 1 - (\tau_{trans}/\tau_{rec}) \tag{2.9}$$

Where L is the active layer thickness, and ξ is a numerical factor (ca. 2.5) that depends on the optical density of the film.[18] If D_n and τ_{rec} are known, effective diffusion length ($L_n = \sqrt{D_n\,\tau_{\mathrm{rec}}}$) is also determined. More exactly, time constant of photocurrent response (τ_{pc}, Eq.2.10) associated with both charge transport and recombination should be used to calculate the η_{CC} rather than the τ_{trans} associated with only charge transport as shown in Eq.2.11.[19-20] However, Eq.2.9 must be valid under the conditions as below.[21-22] Therefore, Eq.2.9 is mainly employed in this thesis.

i. Active layer is thin enough so that the photo-injected electrons are instantly collected

ii. The τ_{rec} is much larger than the τ_{trans}, so that the measured τ_{pc} is almost equal to the τ_{trans}

$$\frac{1}{\tau_{pc}} = \frac{1}{\tau_{trans}} + \frac{1}{\tau_{rec}} \tag{2.10}$$

$$\eta_{CC} = 1 - (\tau_{pc}/\tau_{rec}) \tag{2.11}$$

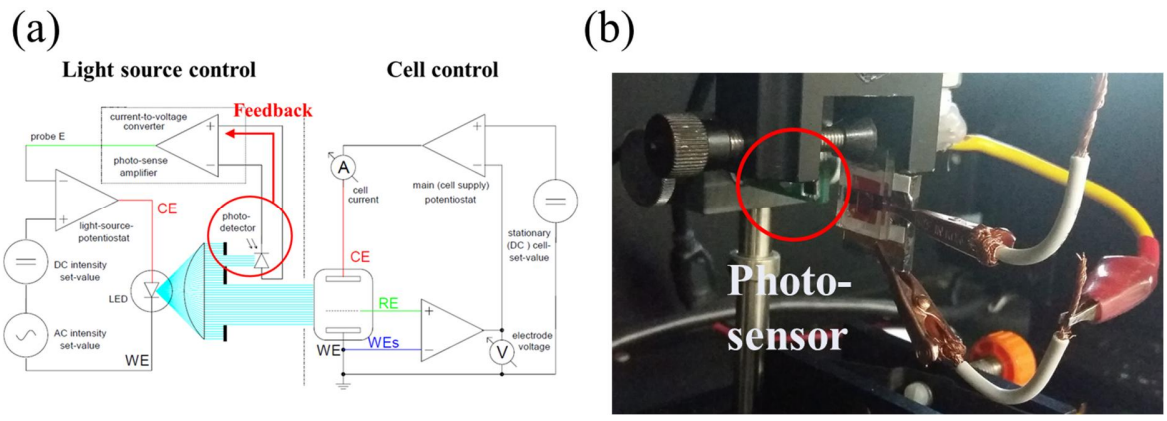

Figure 2.5 (a) Schematic of the CIMPS principle. The photo-diode detector/sense amplifier feedback loop forces the light source potentiostat to control light intensity exactly. (b) Actual photograph during the measurement. Photo-sensor is placed near the cell.

A. J. Frank and co-workers suggested that the τ_{trans} and τ_{rec} be measured at the same ${}_nE_F$ in the TiO_2 film to accurately evaluate the η_{CC}.[19] In other words, both time constants need to be measured at the same circuit state. If the τ_{rec} at open circuit state is used to evaluate the η_{CC}, the resulting value may be underestimated compared to that measured using the τ_{rec} at short-circuit states. For more accuracy, the τ_{rec} should be measured under short-circuit conditions. This can be achieved by charge extraction method under short-circuit states, in which the τ_{rec} is related to time dependent extracted charge (Q_{ext}) as Eq.2.12.[23-24] This method results in about 4 times larger τ_{rec} value compared to that measured by small amplitude modulation method (CIMPS). This difference can be explained by the fact that the CIMPS method measures a lifetime of photo-injected excess charge, while the charge extraction method measures a lifetime of resident electrons in the active layer.

$$\tau_{rec} = Q_{ext}(t)\left(\frac{dQ_{ext}(t)}{dt}\right)^{-1} \tag{2.12}$$

Figure 2.6 shows light intensity dependent frequency response of photocurrent efficiency (η_{IP}'') and photovoltage efficiency (η_{UP}'') in the complex plane, displayed in Bode plot. It is noteworthy, for both cases, that cutoff frequency gradually shifts toward high frequency region when increasing light intensity. These results indicate that τ_{trans} and τ_{rec} tend to change in the same direction along with the light intensity, so that η_{CC} nearly do not depend on the light intensity.[25]

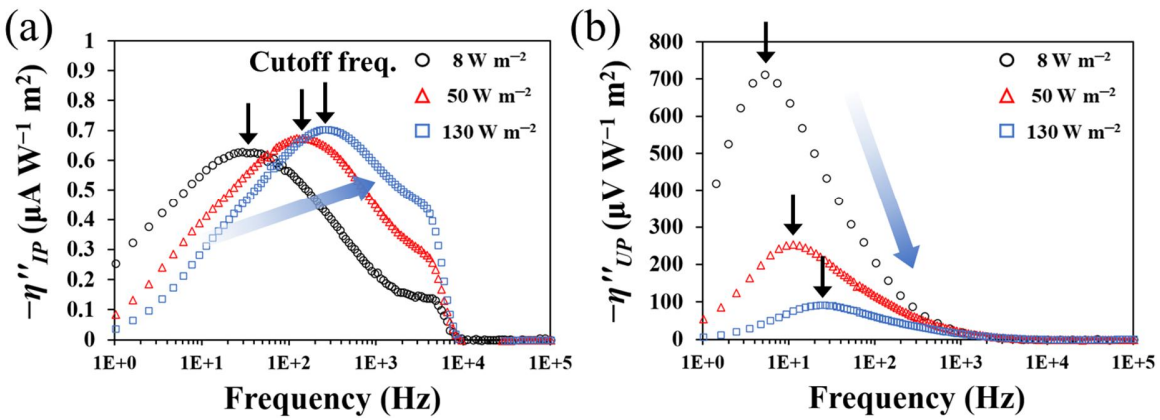

Figure 2.6 Light intensity dependent frequency response of (a) photocurrent efficiency (η_{IP}'') and (b) photovoltage efficiency (η_{UP}'') in the complex plane, displayed in Bode plot. For both η_{IP}'' and η_{UP}'', cutoff frequency gradually shifts toward high frequency region when light intensity increases.

2.2.4 Electrochemical impedance Spectroscopy (EIS)

Definition of Impedance Electrochemical impedance spectroscopy (EIS) is a powerful technique for analyzing the electrical properties of not only bulk materials but also their interfaces with different phases. Compared to steady-state polarization technique such as cyclic voltammetry that provides J-V curve whose slope determines the polarization resistance (R_P) at each point, EIS produces much more information as a function of the input potential or current frequency. It is recommended to carry out prior studies on the experimental object before impedance analysis to properly interpret a large amount of information. Combining with other studies on object: electron microscopic observation of surface morphology, composition, and DC electrochemical characterization, EIS can be much more effective analysis method. As shown in **Figure 2.7a**, the general approach is to apply an electrical stimulus (voltage or current with a small amplitude sinusoidal modulation) to the object and to detect the response signal (frequency dependent current or voltage). The actual input signals depend on the type of object. For the DSCs, V_{OC} under illumination is generally applied with small amplitude modulation (ca. 10~20 mV). The definition of resulting impedance is generally described by Eq.2.13 (**Figure 2.7b**):

$$Z(\mathrm{s}) = \frac{\mathcal{L}[E(t)]}{\mathcal{L}[i(t)]} = \frac{\overline{E}(s)}{\overline{i}(s)} = |Z|(\cos\theta + j\sin\theta) = \sqrt{(Z')^2 + (Z'')^2}\, e^{j\theta} \qquad (2.13)$$

where ☐is the Laplace transform, s is the complex frequency ($s = \sigma + j\omega$, where σ and ω are the real and imaginary parts of frequency), θ is the phase difference between input and output signal, Z' and Z'' are the real and imaginary parts of impedance.

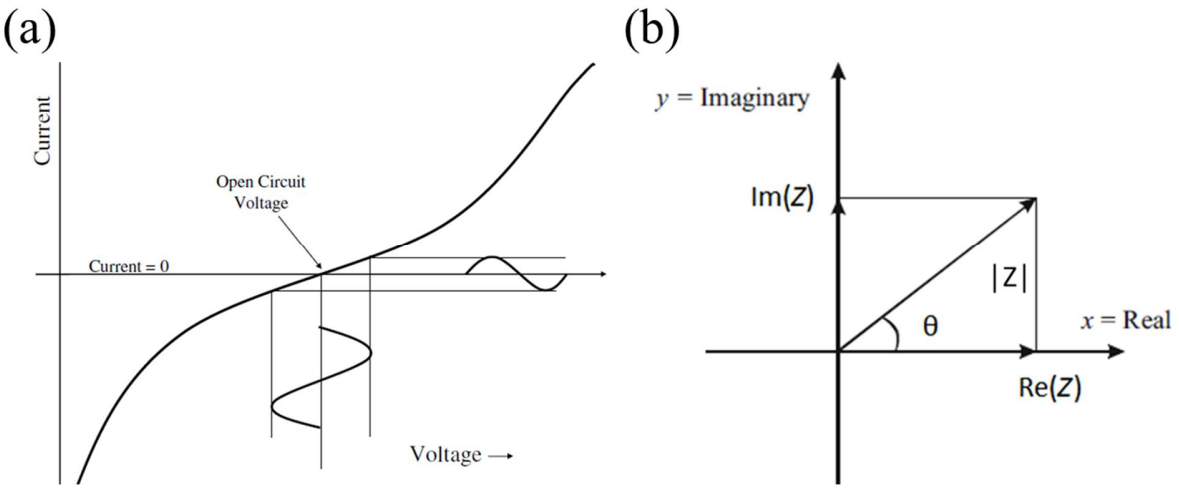

Figure 2.7 (a) Spectroscopic representation of the electrical stimulus on the object and resulting frequency response and (b) representation of vector Z on complex plane.[26-27]

Impedance Analysis of DSCs DSCs contain various electrode materials and ionic conducting layer inside them, accompanying many phase changes such as electrode/electrolyte interface. For that reason, photo-generated charge kinetics in the DSC can be strongly influenced by these interfaces. **Figure 2.8** shows typical impedance spectrum in Nyquist diagram for the DSC based on the liquid electrolyte. Inset shows the structure of DSC with an equivalent circuit elements, called transmission line model, widely used to fit the impedance spectrum of DSC.[28-29] The Nyquist diagram for the DSC consists of three semicircles in general. More specifically, the x-axis ranging from zero to the x-intercept explains series resistance (R_S) that is mainly correlated with sheet resistance of substrate and solution resistance. The first semicircle represents the charge transfer resistance (R_{CE}) and electrical double layer capacitance (C_{CE}) at the counter-electrode/electrolyte interface, respectively. The second semicircle represents the charge recombination resistance (R_{rec} or R_{CT}) and chemical capacitance (C_{μ}) at the mesoporous TiO_2 film, respectively. The third semicircle represents Z_W, which is defined as the Nernst diffusion (Warburg) impedance of redox species in the electrolyte.[30] If an applied bias is high enough so that TiO_2 film is highly conductive, the charge transport resistance (R_{trans}) can be negligible. Moreover, other interface impedances at the substrate/electrolyte (R_{TCO} and C_{TCO}) and the substrate/TiO_2 (R_{CO} and C_{CO}) may be not influential as well.[29]

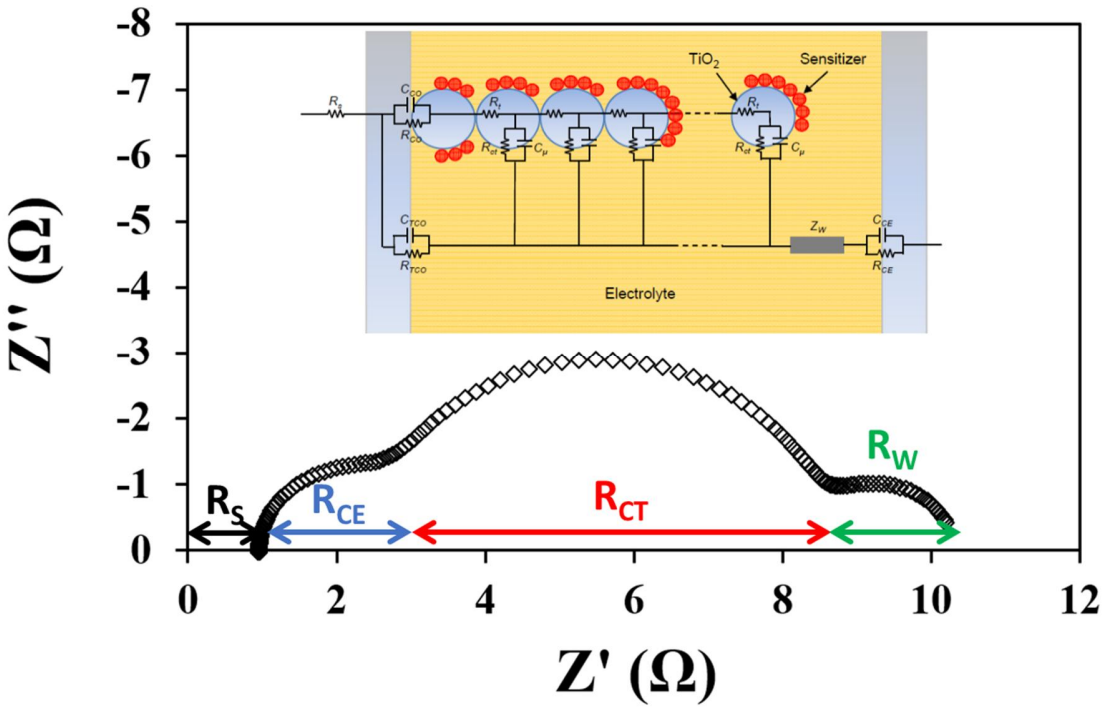

Figure 2.8 Typical Nyquist diagram obtained from liquid type DSC. Inset shows the structure of DSC with corresponding equivalent circuit (transmission line model).

In transmission line model, the impedance has the expression:

$$Z(\omega) = \left(\frac{R_{tans}\,R_{rec}}{1+j\omega/\omega_{rec}}\right)^{1/2} \coth\left[(R_{trans}/R_{rec})^{1/2}\,(1+j\omega/\omega_{rec})^{1/2}\right] \quad (2.14)$$

where ω_{rec} is the angular frequency of the charge transfer (recombination) process. Therefore, a reciprocal ω_{rec} corresponds charge recombination lifetime (τ_{rec}) and it can be expressed using R_{rec} and C_{μ}. If the R_{trans} and film thickness (L) are known, effective diffusion coefficient (D_n) is also calculated as below:

$$\tau_{rec} = {\omega_{rec}}^{-1} = R_{tans}\,C_{\mu} \quad (2.15)$$

$$D_n = L^2/R_{tans}\,C_{\mu} \quad (2.16)$$

When applying a forward bias (generally $-V_{OC}$) in the dark condition, a Fermi level gradient occurs through the TiO_2 film as described in **Figure 2.9a**. Consequently, electrons diffuse from the substrate to the electrolyte side and react with oxidized redox mediator in the electrolyte. If the DSC is illuminated with keeping a forward bias, Fermi level rapidly increases at the electrolyte side and Fermi level gradient may be different according to an applied bias (**Figure 2.9a**). In the general codition ($-V_{OC}$ DC bias and 1 sun), Fermi level gradient may be nearly flat, so that electrons diffuse from the electrolyte side to the substrate because of electron concentration distribution (**Figure 2.9b**).[20]

Figure 2.9c shows experimental impedance spectra of a D-DAHTDTT organic dye cell with a liquid electrolyte, measured by applying a forward bias (–0.65 V) with 10 mV modulation in dark and under illumination. Compared to impedance spectra from dark condition, R_{rec} corresponding to second semicircle is remarkably decreased with illumination. This is attributed to the contribution of photo-electrons from dyes under illumination. It is also noteworthy that the τ_{rec} is significantly decreased when illuminated, as evidenced in Bode plot (inset of **Figure 2.9c**) This can be explained by the difference of the oxidized redox mediator concentration inside TiO_2 film. Under illumination, the oxidized redox mediators (such as I_3^-) are generated inside the TiO_2 film after dye regeneration process, whereas in dark condition, I_3^- ions are generated at counter-electrode and diffuse toward the mesoporous TiO_2 films.[31]

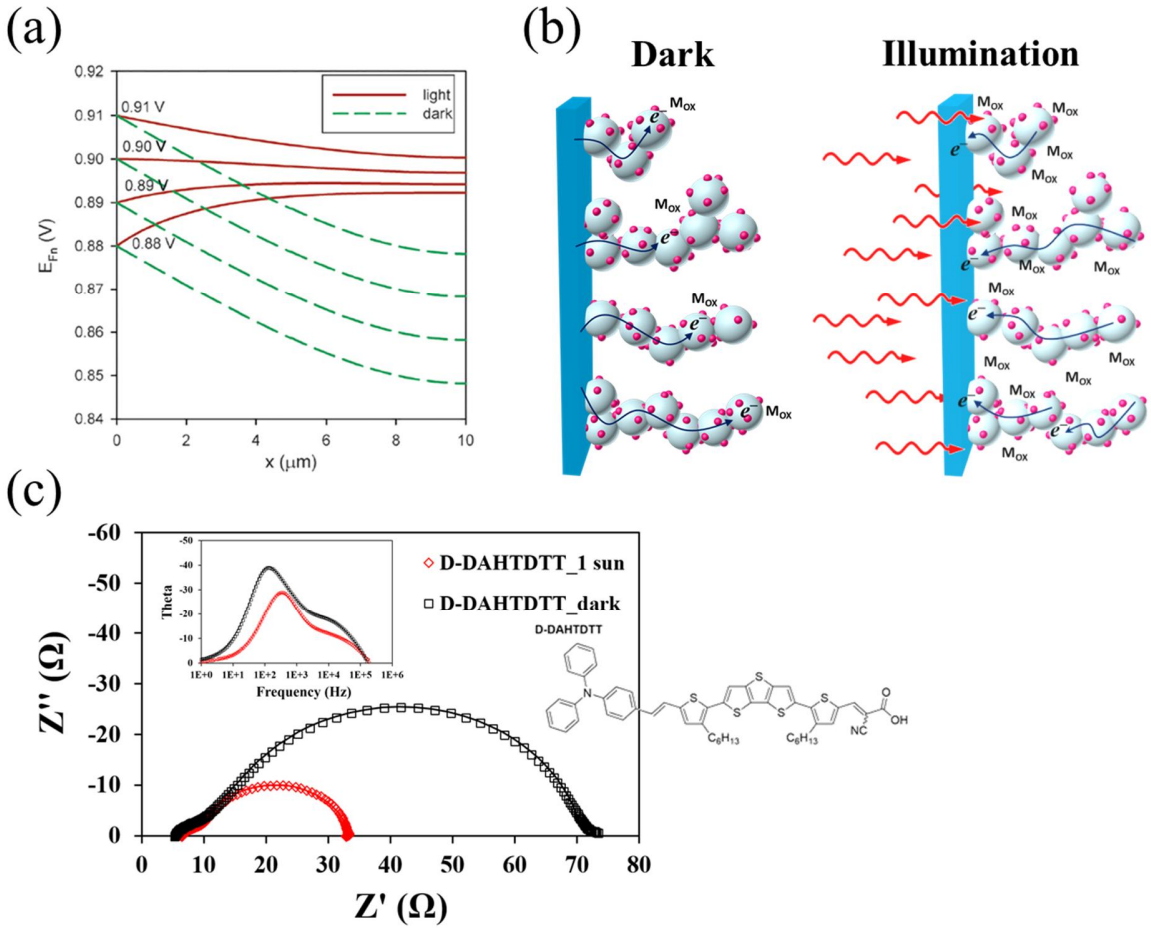

Figure 2.9 (a) The Fermi level distribution by diffusion–recombination of electrons and photogeneration in a TiO_2 film with L = 10-μm, in dark and under illumination and (b) schematic description of electron diffusion in the TiO_2 film in dark and under illumination. (c) Experimental impedance spectra of a D-DAHTDTT organic dye cell with a liquid electrolyte, measured by applying a forward bias (–0.65 V) with 10 mV modulation in dark and under illumination.

REFERENCE

1. Ahmad, S.; Dell'Orto, E.; Yum, J.-H.; Kessler, F.; Nazeeruddin, M. K.; Grätzel, M., Towards flexibility: metal free plastic cathodes for dye sensitized solar cells. *Chem. Commun.* **2012,** *48* (78), 9714-9716.

2. Ellis, H.; Vlachopoulos, N.; Häggman, L.; Perruchot, C.; Jouini, M.; Boschloo, G.; Hagfeldt, A., PEDOT counter electrodes for dye-sensitized solar cells prepared by aqueous micellar electrodeposition. *Electrochim. Acta* **2013,** *107*, 45-51.

3. Sapp, S. A.; Elliott, C. M.; Contado, C.; Caramori, S.; Bignozzi, C. A., Substituted polypyridine complexes of cobalt (II/III) as efficient electron-transfer mediators in dye-sensitized solar cells. *J. Am. Chem. Soc.* **2002,** *124* (37), 11215-11222.

4. Bai, Y.; Yu, Q.; Cai, N.; Wang, Y.; Zhang, M.; Wang, P., High-efficiency organic dye-sensitized mesoscopic solar cells with a copper redox shuttle. *Chem. Commun.* **2011,** *47* (15), 4376-4378.

5. Lee, B.; Stoumpos, C. C.; Zhou, N.; Hao, F.; Malliakas, C.; Yeh, C.-Y.; Marks, T. J.; Kanatzidis, M. G.; Chang, R. P., Air-stable molecular semiconducting iodosalts for solar cell applications: Cs2SnI6 as a hole conductor. *J. Am. Chem. Soc.* **2014,** *136* (43), 15379-15385.

6. Dloczik, L.; Ileperuma, O.; Lauermann, I.; Peter, L.; Ponomarev, E.; Redmond, G.; Shaw, N.; Uhlendorf, I., Dynamic response of dye-sensitized nanocrystalline solar cells: characterization by intensity-modulated photocurrent spectroscopy. *J. Phys. Chem. B* **1997,** *101* (49), 10281-10289.

7. Zhu, K.; Jang, S.-R.; Frank, A. J., Impact of high charge-collection efficiencies and dark energy-loss processes on transport, recombination, and photovoltaic properties of dye-sensitized solar cells. *J. Phys. Chem. Lett.* **2011,** *2* (9), 1070-1076.

8. Grätzel, M., Solar energy conversion by dye-sensitized photovoltaic cells. *Inorg. Chem.* **2005,** *44* (20), 6841-6851.

9. Guo, X.-Z.; Luo, Y.-H.; Zhang, Y.-D.; Huang, X.-C.; Li, D.-M.; Meng, Q.-B., Study on the effect of measuring methods on incident photon-to-electron conversion efficiency of dye-sensitized solar cells by home-made setup. *Rev. Sci. Instrum.* **2010,** *81* (10), 103106.

10. Zhu, K.; Neale, N. R.; Miedaner, A.; Frank, A. J., Enhanced charge-collection efficiencies and light scattering in dye-sensitized solar cells using oriented TiO2 nanotubes arrays. *Nano Lett.* **2007,** *7* (1), 69-74.

11. Katoh, R.; Furube, A., Electron injection efficiency in dye-sensitized solar cells. *J. Photochem. Photobiol., C* **2014,** *20*, 1-16.

12. Wang, Q.; Ito, S.; Gratzel, M.; Fabregat-Santiago, F.; Mora-Sero, I.; Bisquert, J.; Bessho, T.; Imai, H., Characteristics of high efficiency dye-sensitized solar cells. *Journal of Physical Chemistry B* **2006,** *110* (50), 25210-25221.

13. Bisquert, J.; Fabregat-Santiago, F.; Mora-Sero, I.; Garcia-Belmonte, G.; Gimenez, S., Electron lifetime in dye-sensitized solar cells: theory and interpretation of measurements. *J. Phys. Chem. C* **2009,** *113* (40), 17278-17290.

14. Xue, G.; Yu, X.; Yu, T.; Bao, C.; Zhang, J.; Guan, J.; Huang, H.; Tang, Z.; Zou, Z., Understanding of the chopping frequency effect on IPCE measurements for dye-sensitized solar cells: from the viewpoint of electron transport and extinction spectrum. *J. Phys. D: Appl. Phys.* **2012,** *45* (42), 425104.

15. Yang, X.; Yanagida, M.; Han, L., Reliable evaluation of dye-sensitized solar cells. *Energy Environ. Sci.* **2013,** *6* (1), 54-66.

16. Schlichthörl, G.; Huang, S.; Sprague, J.; Frank, A., Band edge movement and recombination kinetics in dye-sensitized nanocrystalline TiO2 solar cells: a study by intensity modulated photovoltage spectroscopy. *J. Phys. Chem. B* **1997,** *101* (41), 8141-8155.

17. Fisher, A.; Peter, L.; Ponomarev, E.; Walker, A.; Wijayantha, K., Intensity dependence of the back reaction and transport of electrons in dye-sensitized nanocrystalline TiO2 solar cells. *J. Phys. Chem. B* **2000,** *104* (5), 949-958.

18. Jennings, J. R.; Ghicov, A.; Peter, L. M.; Schmuki, P.; Walker, A. B., Dye-sensitized solar cells based on oriented TiO2 nanotube arrays: transport, trapping, and transfer of electrons. *J. Am. Chem. Soc.* **2008,** *130* (40), 13364-13372.

19. Schlichthörl, G.; Park, N.; Frank, A., Evaluation of the charge-collection efficiency of dye-sensitized nanocrystalline TiO2 solar cells. *J. Phys. Chem. B* **1999,** *103* (5), 782-791.

20. Van de Lagemaat, J.; Park, N.-G.; Frank, A., Influence of electrical potential distribution, charge transport, and recombination on the photopotential and photocurrent conversion efficiency of dye-sensitized nanocrystalline TiO2 solar cells: a study by electrical impedance and optical modulation techniques. *J. Phys. Chem. B* **2000,** *104* (9), 2044-2052.

21. Hagfeldt, A.; Boschloo, G.; Sun, L.; Kloo, L.; Pettersson, H., Dye-Sensitized Solar Cells. *Chem. Rev.* **2010,** *110* (11), 6595-6663.

22. Bertoluzzi, L.; Ma, S., On the methods of calculation of the charge collection efficiency of dye sensitized solar cells. *Phys. Chem. Chem. Phys.* **2013,** *15* (12), 4283-4285.

23. Duffy, N. W.; Peter, L. M.; Rajapakse, R. M. G.; Wijayantha, K. G. U., A novel charge extraction method for the study of electron transport and interfacial transfer in dye sensitised nanocrystalline solar cells. *Electrochemistry Communications* **2000,** *2* (9), 658-662.

24. Boschloo, G.; Häggman, L.; Hagfeldt, A., Quantification of the effect of 4-tert-butylpyridine addition to I-/I3-redox electrolytes in dye-sensitized nanostructured TiO2 solar cells. *J. Phys. Chem. B* **2006,** *110* (26), 13144-13150.

25. Krüger, J.; Plass, R.; Grätzel, M.; Cameron, P. J.; Peter, L. M., Charge transport and back reaction in solid-state dye-sensitized solar cells: a study using intensity-modulated photovoltage and photocurrent spectroscopy. *J. Phys. Chem. B* **2003,** *107* (31), 7536-7539.

26. Macdonald, J. R.; Barsoukov, E., *Impedance spectroscopy: theory, experiment, and applications*. John Wiley & Sons, Inc.: Canada, 2005; Vol. 1, p 1-20.

27. Lasia, A., *Electrochemical impedance spectroscopy and its applications*. Springer: New York, 2014; p 44-47.

28. Fabregat-Santiago, F.; Bisquert, J.; Garcia-Belmonte, G.; Boschloo, G.; Hagfeldt, A., Influence of electrolyte in transport and recombination in dye-sensitized solar cells studied by impedance spectroscopy. *Sol. Energy Mater. Sol. Cells* **2005,** *87* (1-4), 117-131.

29. Fabregat-Santiago, F.; Garcia-Belmonte, G.; Mora-Sero, I.; Bisquert, J., Characterization of nanostructured hybrid and organic solar cells by impedance spectroscopy. *Phys. Chem. Chem. Phys.* **2011,** *13* (20), 9083-9118.

30. Kim, B.-M.; Son, M.-K.; Kim, S.-K.; Hong, N.-Y.; Park, S.; Jeong, M.-S.; Seo, H.; Prabakar, K.; Kim, H.-J., Improved performance of CdS/CdSe quantum dot-sensitized solar cells using Mn-doped PbS quantum dots as a catalyst in the counter electrode. *Electrochim. Acta* **2014,** *117*, 92-98.

31. Wang, Q.; Moser, J.-E.; Grätzel, M., Electrochemical impedance spectroscopic analysis of dye-sensitized solar cells. *J. Phys. Chem. B* **2005,** *109* (31), 14945-14953.

Chapter 3. Performance Optimization of Thin Photoactive TiO_2 Film-based DSCs using Indoline-based Sensitizer

3.1 Introduction

Persistent efforts have been made to improve the performance of dye-sensitized solar cells (DSCs) over the past 20 years.[1-2] The sudden advent of perovskite solar cells caused a declining trend in the number of studies on DSCs due to their incredible power conversion efficiency (PCE) and low cost.[3-5] Nevertheless, it is still worthwhile to research DSCs, as they are promising integrated photovoltaic (BIPV) systems owing to their several advantages, including transparency, multicolor and flexibility, and are suitable for indoor systems because they are operable under low light intensity and impervious to incident angles.[6-7] In this respect, flexible-type cells are required for a wide range of applications. A thick active layer should be avoided because of film peeling that would limit the development of efficient flexible-type DSCs.[8-9] Therefore, it is important to achieve a high PCE value with a thin active layer.

All the parts of the DSCs are essential and profoundly affect the device performance. Sensitizers in the photo electrode, which act as light harvesters, are key components. There have been many studies on metal-free organic dyes to replace conventional metal-based dyes as the sensitizer for DSCs.[10-14] Their primary merits are a high molar extinction coefficient, tunable absorption ability, and electrochemical properties, thus having the potential for giving a high PCE with a thin active layer. To date, most organic dyes have been based on charge donor, π-bridge, and acceptor moieties to enhance the absorption range, resulting in a PCE greater than 10%.[15] However, most of the high PCEs with iodine electrolyte have appeared in an active layer over 10-μm to date, which is a far from cost-effective conditions.[16]

To overcome this issue, this work documents the design of new indoline derivatives by introducing cyclopentadithiophene units as a π-conjugated bridge, named **RK-1**, **2**, **3** and **4**. The derivatives are characterized by a high molar extinction coefficient greater than 70,000 cm^{-1} M^{-1}, enabling highly-efficient DSCs based on thin mesoporous titanium dioxide (TiO_2) film (< 2-μm) with I^-/I_3^- redox mediators. Their planar structure, as shown in **Figure 3.1**, allows high dye loading, even on a thin TiO_2 film. However, such planar types of molecules are also prone to agglomeration due to π- π stacking. Therefore, alkyl chains with different lengths ranging from a

methyl to a hexadecyl group were introduced on cyclopentadithtiophene to control dye aggregation. It has been generally recognized that alkyl chains on dyes act as a shield against the oxidized redox mediators, decreasing the back reaction rate of photoelectrons injected and improving the performance of DSCs.[17] Meanwhile, unintended dye aggregation can be induced by Van der Waals force interaction between long alkyl chains.[18] These two facts are expected to generate a trade-off between the positive and negative effects on the performance of DSCs.

These simple variables in the molecular structure caused an apparent difference in the performance of DSCs. In a 1.8-μm active and 2.5-μm scattering layer; the same scattering layer was always used together in this work, DSCs based on **RK-3** dyes with dodecyl groups exhibited the best PCE of 9.1% under one sun illumination (AM 1.5, 1000 $W \cdot m^{-2}$) with a great photocurrent density (J_{SC} = 16.2 $mA \cdot cm^{-2}$). A time-resolved photoluminescence (PL) investigation revealed that the most favorable charge injection from **RK-3** dyes facilitated the highest J_{SC}. However, when increasing the active layer thickness, the overall device performance gradually dropped while **RK-2** provided the little affected PCE (8.8% for 3.5-μm and 7.9% 5.1-μm). This was because the charge collection and regeneration became more influential than the charge injection for the device performance.

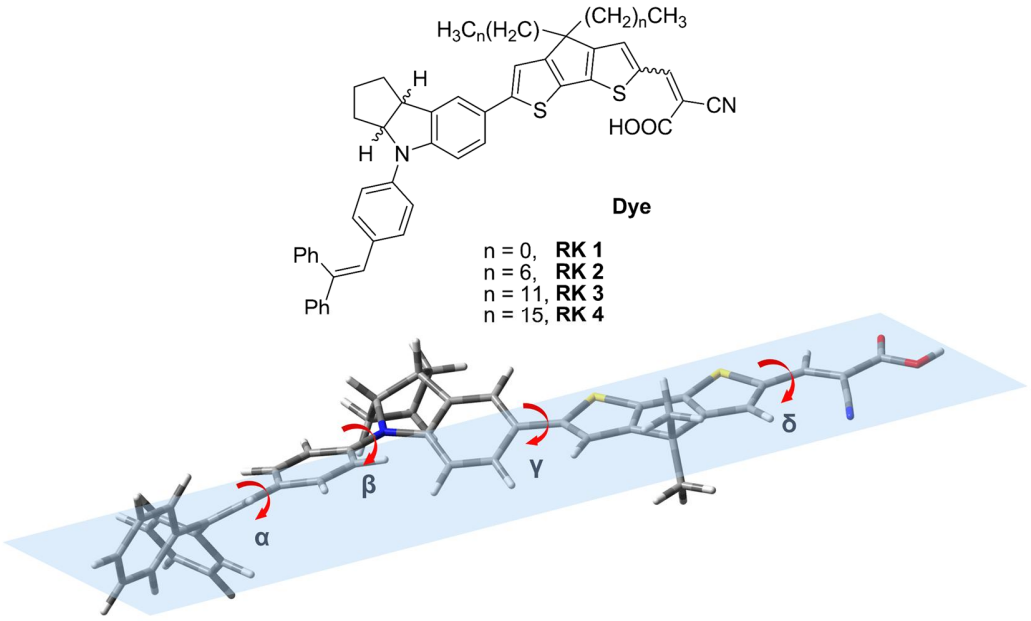

Figure 3.1 Chemical structures of the **RK-1** – **4** organic dyes. All dyes have a flat structure and no difference in the molecular structure between them except for the alkyl chain length, which increases from **RK-1** to **RK-4**. The dihedral angles are summarized in Table 3.1.

3.2 Results and discussion

Photophysical and Electrochemical Properties Photophysical properties of **RK** series were assessed through both experimental and computational methods. Absorbance and emission spectra of each dye in dichloromethane (CH_2Cl_2) containing 0.1 M triethylamine were obtained as shown in **Figure 3.2a**. With the exception of **RK-1**, all λ_{max} and λ_{onset} values for absorbance were similarly positioned at 487 nm and 555 nm, respectively. The transition energy $E_{0\text{-}0}$ of each dye was estimated using the corresponding λ_{onset} of absorbance spectroscopy (**Table 3.1**). The estimated energy gap for all dyes was very similar (ca. 2.23 V), clearly confirmed by the similarly positioned emission peaks.

The highest occupied molecular orbital (HOMO) levels were measured using cyclic voltammetry (**Figure 3.2b**), and their results were similar to each other, 0.72 V for **RK-1** and 0.74 V for **RK-2**, **3** and **4** (*vs*. NHE; in this communication, all potentials are based on NHE). Moreover, the peak-to-peak separation potential ΔE inversely proportional to the charge transfer rate was very small, only 27.32 mV for **RK-3** (98.91 mV for ferrocene used together as reference).[19] The findings indicate excellent electrochemical reactivity and stability of the **RK** series. Although the HOMO levels of **RK** series (0.72 V and 0.74 V) were even more negative than that of N719 (1.1 V)[20-22], they exhibited efficient charge regeneration with the I^-/I_3^- redox mediators (E_{redox} = ca. 0.35 V) as discussed later. The excited state potential corresponding to the lowest unoccupied molecular orbital (LUMO) level was evaluated by subtracting the transition energy $E_{0\text{-}0}$ from the ground state oxidization potentials E_{ox}. Every dye shows a sufficiently high excited state potential (ca. –1.5 V) compared to the TiO_2 conduction band edge (ca. –0.5 V), facilitating smooth electron injection.

Computational Calculations The density functional theory results strongly support the experimental results. **Figure 3.3** shows the distribution of frontier molecular orbitals in each isolated dye. In all dyes, the HOMOs were well dispersed through the D-π-A part, while the LUMOs were localized at the π-A part, a benefit of the electron injection from the dye to the TiO_2 conduction band. There is also a slight difference between the experimental and simulated values of the HOMO and LUMO levels. No difference was observed in the spin density distribution in oxidized monomeric dye, indicating a similar charge recombination rate with oxidized dyes under the assumption that all dyes have a similar arrangement and orientation on the TiO_2 (**Figure 3.4**).

Table 3.1 Summary of photophysical and computational data for **RK-1** – **4** dyes.

	Abs.[a] (ε*10^4 $cm^{-1}M^{-1}$)	*PL*[a] λ_{max} (nm)	E_{OX}[b] *vs NHE* (V)	$E_{0\text{-}0}$[c] *vs NHE* (V)	$E_{OX} - E_{0\text{-}0}$ *vs NHE* (V)	*Dihedral angle* (°) α	β	γ	δ	*Dipole moment* (D)	*Excited state lifetime*[d] (ns)
RK-1	480 (6.74), 392 (3.37)	625	0.72	2.23	-1.51	24.3	18.0	25.8	0.03	8.81	1.566
RK-2	487 (6.85), 392 (3.05)	624	0.74	2.23	-1.49	25.1	17.2	26.5	0.09	8.77	1.655
RK-3	487 (6.96), 392 (2.85)	625	0.74	2.23	-1.49	25.1	17.5	24.8	0.04	8.70	1.677
RK-4	486 (7.02), 392 (2.92)	625	0.74	2.24	-1.50	25.5	21.8	28.4	0.32	8.90	1.690

[a] All the spectra were measured in 20 μM CH_2Cl_2 solution at 298 K. [b] The onset point in anodic curve was used for estimating ground state oxidation potential. [c] The transition energy of each dye was estimated from the onset point in absorbance spectrum. All the potential were represented versus normal hydrogen electrode by adding Fc^+/Fc redox potential (+0.63 V).[3] [d] Singlet excited state lifetime of each dye was estimated from following equation. $\tau = 1.499/(f \cdot E^2)$, where E ($cm^{-1}$) is the excitation energy of the different electronic states and f is the oscillator strength of the electronic state, not giving cause for the difference in exciton self-quenching according to the alkyl chain length.

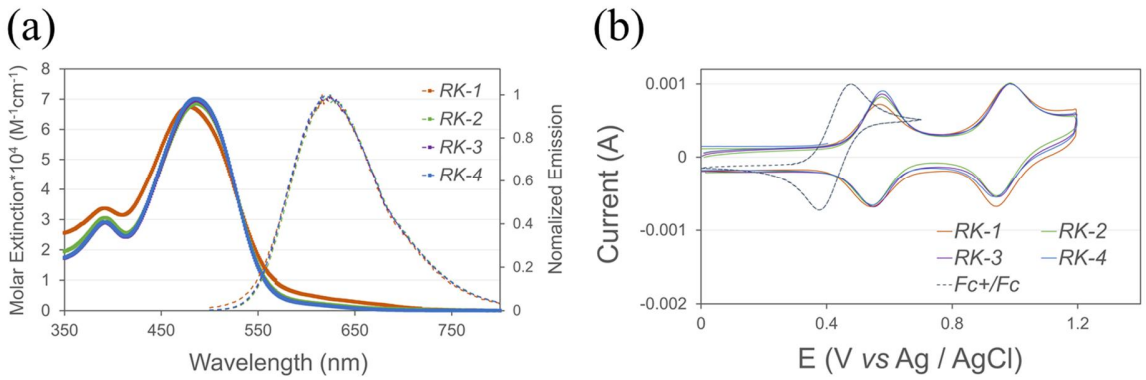

Figure 3.2 (a) UV-vis and photoluminescence spectra for **RK-1** – **4**, measured in a 20 μM CH_2Cl_2 solution containing 0.1 M triethylamine. (b) Cyclic voltammograms obtained from **RK** dye-dissolved CH_2Cl_2 solution containing tetrabutylammonium hexafluorophosphate ($TBAPF_6$,) as a supporting electrolyte. The Fc/Fc^+ redox potential was used as internal reference.

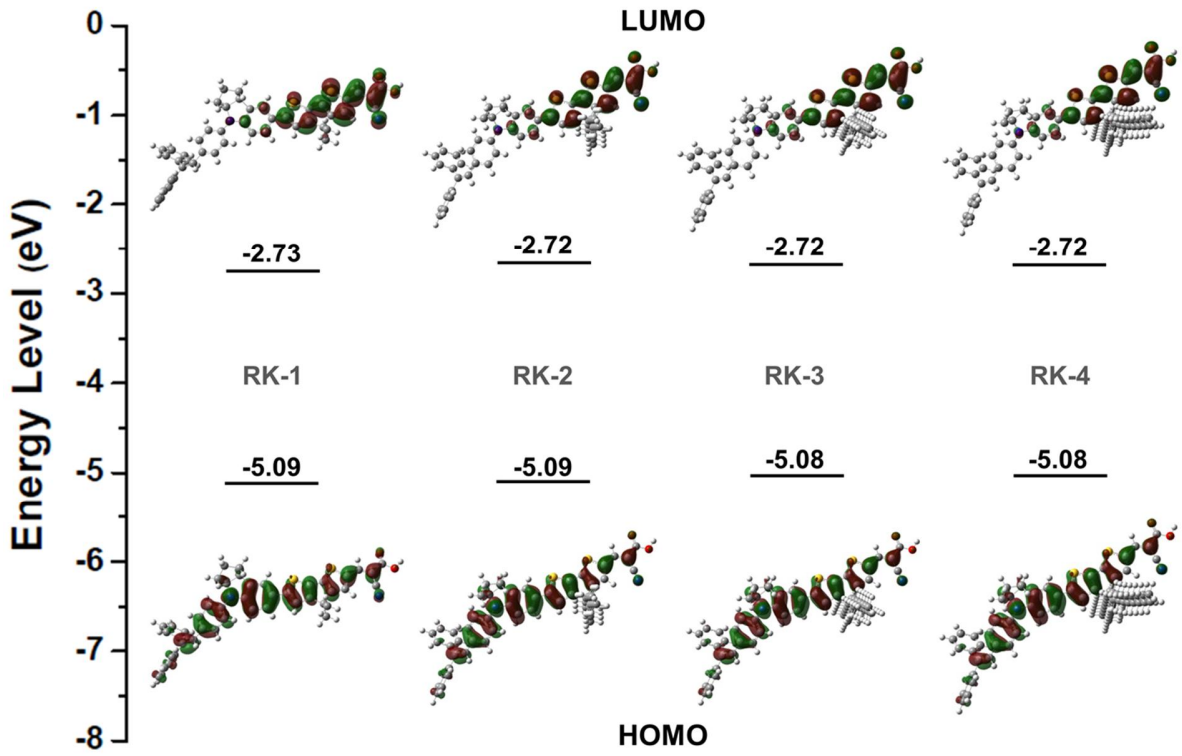

Figure 3.3 HOMO, LUMO, and electron density difference maps between the excited and ground states of **RK-1** – **4** dyes.

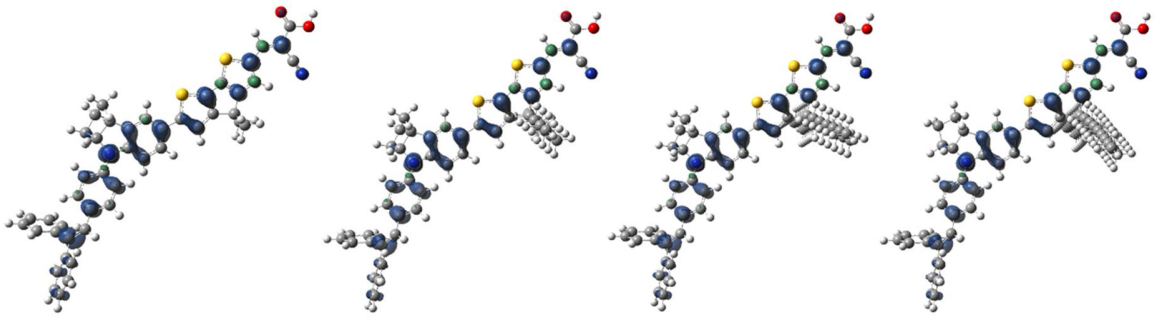

Figure 3.4 Spin density distribution in oxidized monomeric dye, corresponding to **RK-1** – **4** from left one by one. They show similar positive charge signals each other, implying similar chance for accepting electron.

Device Performances **RK** series were applied to DSCs for evaluating their photovoltaic ability in different active layer thicknesses (1.8-μm, 3.5-μm, and 5.1-μm with a 2.5-μm scattering layer) without any co-adsorbate. For preparing the photoactive TiO_2 films, screen printed mesoporous TiO_2 films were immersed in a dye solution (0.2 mM in $CHCl_3$) at room temperature under dark conditions for 2 – 2.5 hours and then assembled with a Pt-coated counter electrode into a sandwich configuration, followed by injection of electrolyte composed of 0.055 M I_2, 0.025 M LiI, 0.05M guanidine thiocyanate, 0.6 M DMPII and 0.5 M 4-tert-butylpridine in a mixture of acetonitrile and valeronitrile (v/v, 85/15).

Figure 3.5 shows the J-V curves for the four dyes studied under one sun illumination, and all performance parameters are summarized in **Table 3.2**. With a 1.8-μm active layer, **RK-3** with a dodecyl group reached the best PCE (9.1%) without any co-adsorbate, corresponding to an open circuit voltage (V_{OC}) of 0.74 V, a photocurrent density (J_{SC}) of 16.2 mA·cm^{-2}, and a fill factor (*FF*) of 0.76. To date, this is one of the best performances in a very thin TiO_2 film (1.8-μm active layer) with iodine electrolyte system. The next highest PCE (η = 8.2% with a V_{OC} of 0.73 V, J_{SC} of 14.9 mA·cm^{-2}, and *FF* of 0.75) was obtained by **RK-2** with a heptyl group, followed by **RK-4** with a hexadecyl group (η = 6.4% with a V_{OC} of 0.68 V, J_{SC} of 12.9 mA·cm^{-2}, and *FF* of 0.72) and **RK-1** with a methyl group (η = 5.7% with a V_{OC} of 0.65 V, J_{SC} of 12.1 mA·cm^{-2}, and *FF* of 0.73). With a 3.5-μm active layer, all the device performances, except for **RK-2**, generally decreased even though the active layer thickness increased. As a result, the **RK-2** provided a higher PCE (η = 8.8% with a V_{OC} of 0.74 V, J_{SC} of 15.9 mA·cm^{-2} and *FF* of 0.75) than **RK-3** (η = 8.2% with a V_{OC} of 0.74 V, the J_{SC} of 15.2 mA·cm^{-2}, and *FF* of 0.73). Compared to the case of 1.8-μm active layer, **RK-2** showed a *ca.* 7% improved PCE while that of **RK-3** decreased *ca.* 10% due to the dramatic decrease in J_{SC}. Even after further increasing the active layer thickness to 5.1-μm, the order of PCE was the same as that of 3.5-μm, **RK-2** > **RK-3** > **RK-4** > **RK-1**, but all device performances decreased markedly. Nevertheless, **RK-2** maintained a good PCE (η = 7.9% with a V_{OC} of 0.73 V, J_{SC} of 15.1 mA·cm^{-2}, and *FF* of 0.72).

In summary, **RK-3** achieved the best PCE (9.1%) in a 1.8-μm active layer with no co-adsorbate, but a much lower PCE when increasing the active layer thickness to 3.5-μm (8.2%) and 5.1-μm (6.6%). In contrast, **RK-2** obtained the optimized PCE (8.8%) with a 3.5-μm active layer. These results suggest that **RK-3** with an unprecedented PCE in thin TiO_2 film (1.8-μm) could be an ideal and economical candidate for flexible DSCs. However, the enhanced performance in thinner films

is very unusual compared to a previously reported trend in organic dyes.[23] In addition, depending on the alkyl chain length, especially **RK-2** and **3**, their device performances and trends are quite different. For a full understanding, more detailed experiments and explanations are outlined in Experiment Section.

Table 3.2. The photovoltaic parameters of **RK** dye-sensitized solar cells according to the active layer thickness.

	Film thickness (*μm*)	V_{OC} (V)	J_{SC} (mA cm^{-2})	*FF* *(%)*	η (%)	η_{avg} *(%)*
RK-1	1.8 + 2.5	0.65	12.13	73.1	5.72	5.43
RK-2		0.73	14.86	75.4	8.15	7.84
RK-3		0.74	16.19	75.5	9.07	8.80
RK-4		0.68	12.94	72.0	6.38	6.13
RK-1	3.5 + 2.5	0.63	12.06	71.6	5.44	5.22
RK-2		0.74	15.94	74.5	8.78	8.40
RK-3		0.74	15.19	72.8	8.20	8.02
RK-4		0.66	12.75	73.8	6.21	5.96
RK-1	5.1 + 2.5	0.59	12.19	72.5	5.19	4.83
RK-2		0.73	15.06	72.2	7.91	7.61
RK-3		0.73	12.81	71.1	6.62	6.29
RK-4		0.61	11.82	73.9	5.41	4.97

For the measurement of η_{PCE}, a black mask (0.5 × 0.5 cm^2) was always attached to the DSCs for preventing the overestimation. All dye solutions were composed of 0.2 mM **RK-1** – **4** in $CHCl_3$ without a co-adsorbate. The electrolyte was composed of 0.055 M I_2, 0.025 M LiI, 0.05 M guanidine thiocyanate, 0.6 M DMPII and 0.5 M 4-tert-butylpridine in a mixture of acetonitrile and valeronitrile (v/v, 85/15).

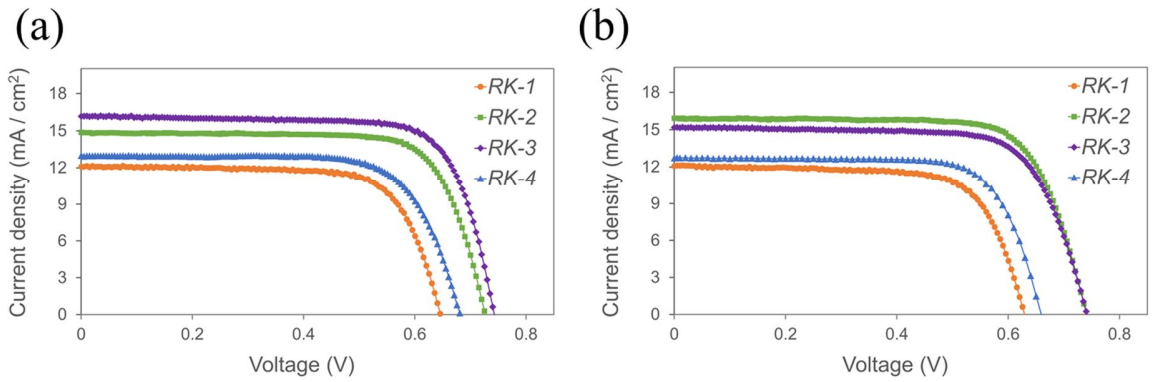

Figure 3.5 J-V curves of DSCs based on **RK** organic dyes according to the active layer thickness: (a) 1.8-μm and (b) 3.5-μm.

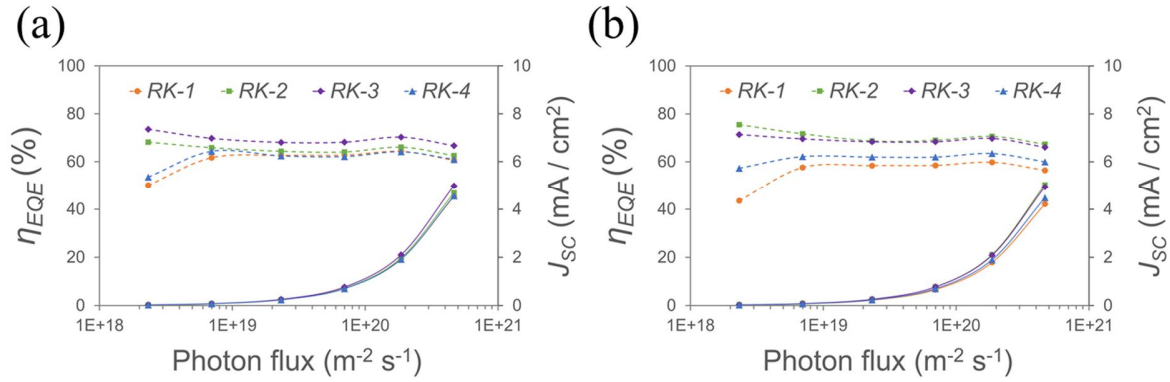

Figure 3.6 Photocurrent density of **RK** DSCs with (a) 1.8-μm and (b) 3.5-μm TiO_2 film as active layer, measured according to incident light intensity. For certainty, corresponding external quantum efficiency is also presented, automatically calculated by Thales software using spectral responsivity equation. See the experimental part for references.

Device Analysis In the device performance trend, the most noticeable point is the competition between **RK-2** and **3**. With a 1.8-μm active layer, **RK-3** provides a much higher J_{SC} (16.2 mA·cm^{-2}) than **RK-2** (14.9 mA·cm^{-2}), but the reversed trend was observed after increasing the active layer thickness to 3.5-μm (15.9 mA·cm^{-2} for **RK-2** and 15.2 mA·cm^{-2} for **RK-3**). This J_{SC} trend becomes clearer when using a 5.1-μm active layer. The J_{SC} of the **RK-3** DSC considerably decreased from 15.2 mA·cm^{-2} to 12.8 mA·cm^{-2} while that of **RK-2** a little reduced from 15.9 mA·cm^{-2} to 15.1 mA·cm^{-2}. To ensure this point, we measured their J_{SC} values and corresponding external quantum efficiencies (η_{EQE}) as a function of the incident light intensity using a monochromatic light source (λ = 463 nm, close to the absorption peak of **RK** series). The tendency of J_{SC} was consistent with that under one sun illumination, as shown in **Figure 3.6**. The corresponding η_{EQE} values show that clearly. J_{SC} is commonly expressed by Eq.3.1:[24-25]

$$J_{SC} = q\,\eta_{lh}\,\eta_{inj}\,\eta_{cc}\,\eta_{reg}\,I_0 \tag{3.1}$$

Where q is the elementary charge, I_0 is the incident photon flux, η_{lh} is the light harvesting efficiency, η_{inj} is the charge injection efficiency, η_{cc} is the charge collection efficiency, and η_{reg} is the regeneration yield. Excluding the two constants q and I_0, the product of four factors, η_{lh}, η_{inj}, η_{cc}, and η_{reg}, is generally defined as η_{EQE}.[24-25] Analyzing these factors could explain why the J_{SC} trend between **RK-2** and **3** changes along the active layer thickness. η_{cc} and η_{reg} is proposed to become more and more decisive for J_{SC} with increasing active layer thickness because of an increase in the contact area of the TiO_2 nanoparticles with the electrolyte and travelling distance of iodide ions for reaching the oxidized dyes. Furthermore, the impact of alkyl chain length on η_{cc} and η_{reg} also becomes more decisive with increasing active layer thickness. However, under the thin active layer, η_{inj} could play a major role in the J_{SC}. These assumptions reasonably explain the tendency of J_{SC} and were clarified by the following analyses.

The charge injection efficiency (η_{inj}) can be quantitatively estimated by η_{EQE}, absorption coefficient (α), charge diffusion length (L_n) and active layer thickness (d), as shown in Eq.3.2 that Piers R. F. Barnes et al. introduced.[26] **Figure 3.7** illustrates that η_{inj} was determined as a function of the incident photon flux. The maximum η_{inj} was achieved by **RK-3** in both 1.8-μm (avg. 0.75) and 3.5-μm (avg. 0.78) active layers, which did not follow the J_{SC} trend. **RK-3** has a lower J_{SC}

(15.2 mA·cm^{-2}) than **RK-2** (15.9 mA·cm^{-2}) with a 3.5-μm active layer. Nevertheless, η_{inj} for **RK-3** is always greater than that for **RK-2**. These results can be explained by the degree of dye aggregation.

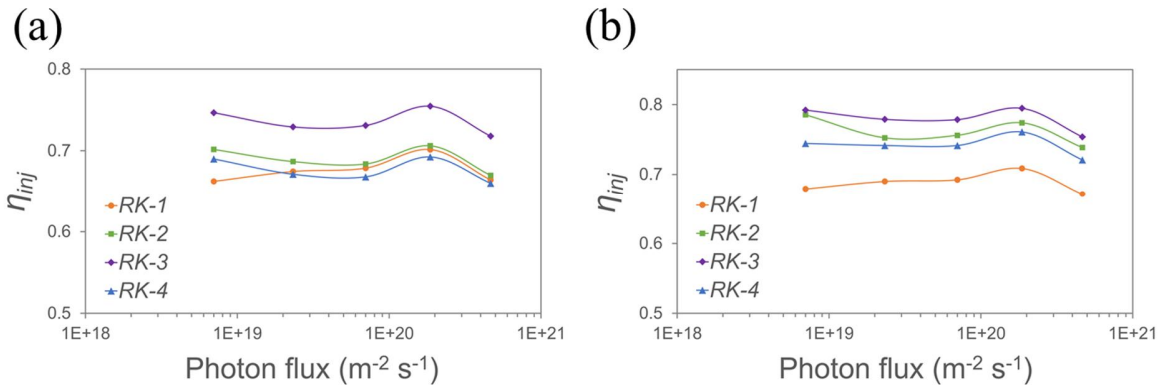

Figure 3.7 Charge injection efficiency of **RK** DSCs with (a) 1.8-μm and (b) 3.5-μm TiO_2 film as active layer, calculated from Eq.3.2 Piers R. F. Barnes *et al.* reported.[26] For semiconducting electrode side illumination charge injection efficiency is determined as follows.

$$\eta_{inj} = \frac{\eta_{EQE}(L_n^2\alpha^2-1)(1+e^{2d/L_n})}{L_n\alpha e^{-\alpha d}(1-R_{SE})\{e^{(\alpha d+2d/L_n)}(L_n\alpha-1)+e^{\alpha d}(L_n\alpha+1)-2L_n\alpha e^{d/L_n}\}}$$

Where L_n is the charge diffusion length, d is the active layer thickness and α is the absorption coefficient defined as follows.

$$\alpha(\lambda) = -\frac{1}{d}\ln\frac{T_{dye/TiO_2(\lambda)}}{T_{TiO_2(\lambda)}}$$

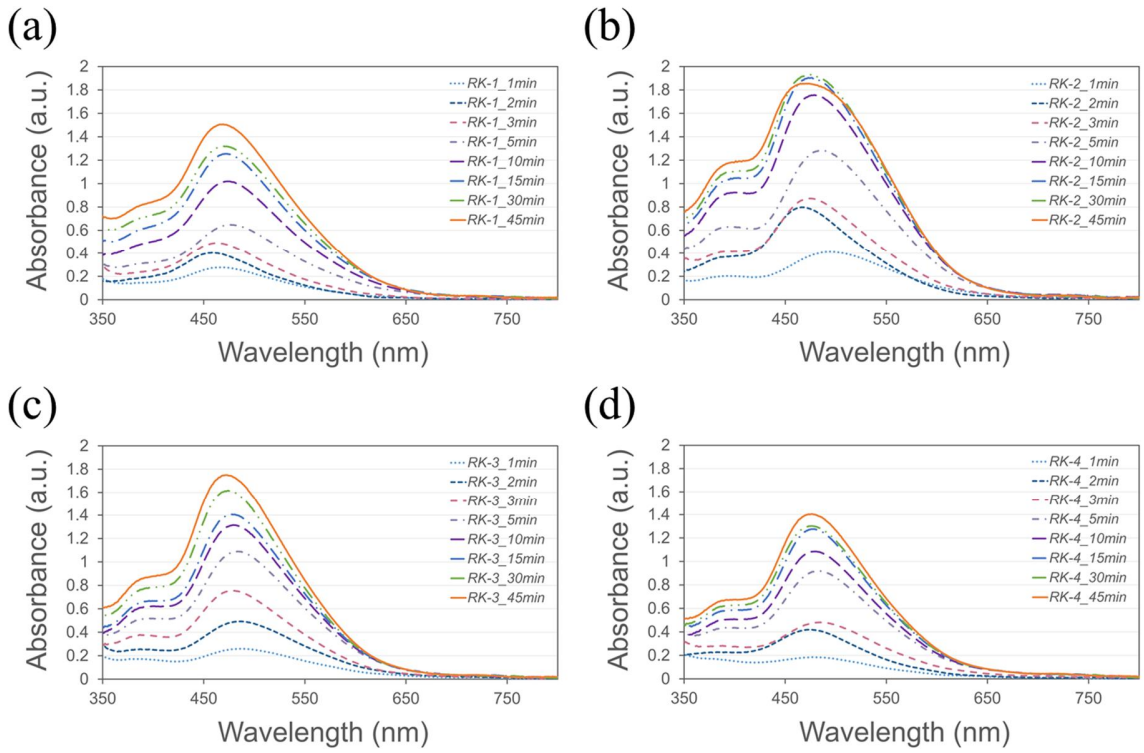

Figure 3.8 Absorbance spectra of **RK** dye-sensitized TiO_2 film (1.8-μm) as a function of soaking time. Note initial states until 3 min.

Figure 3.8 shows the absorbance spectra of each RK dye-sensitized TiO_2 film, differentiated by the soaking time and sensitizer. The aim of this section is to understand the degree of dye aggregation depending on the alkyl chain length from the change in absorbance spectra of dye monolayer on the TiO_2 surface. Thus, **RK-1** with the methyl groups is not a subject of debate. It has been commonly recognized that the blue and red-shift of absorption peak originate from head to head (H-type) and head to tail (J-type) aggregation, respectively. Therefore, the absorption peak position is determined by the ratio between H and J-type agglomerates. All the dyes show similar trend in which absorption peaks are eventually blue-shifted within a few minutes. Interestingly, the order of blue-shift between dyes was variable, but no longer changing from 10 min with overall gradual blue-shift along with time. It was attributed to continuous dye adsorption without co-adsorbate, not giving the information about dye aggregation anymore. So, we focused on the change of absorption peaks until 3 min.

Table 3.3 Dye loading amount data of each dye according to the soaking time.

	Film absorption test (1.8 μm)								DSCs	
	1 min	2 min	3 min	5 min	10 min	15 min	30 min	45 min	120 min (1.8 μm)	150 min (3.5 μm)
	$\times 10^{-8}$ mol cm^{-2}[a]								$\times 10^{-8}$ mol cm^{-2}[a]	
RK-1	0.251	0.487	0.645	0.721	1.263	1.593	1.866	2.286	3.625	5.839
RK-2	0.285	0.745	0.864	1.309	2.008	2.312	2.603	2.628	4.414	7.861
RK-3	0.234	0.369	0.543	0.775	1.017	1.181	1.356	1.597	3.412	5.046
RK-4	0.087	0.241	0.357	0.687	0.884	1.054	1.164	1.316	2.957	3.775

[a] Dye loading amount was estimated using Beer Lambert law ($A = \varepsilon lc$), where A is the absorbance intensity of desorption solution, ε is the molar extinction coefficient, l is the optical path length and c is the dye molar concentration. For acquiring the absorbance data of desorption solution, we firstly immersed TiO_2 film substrate in 0.2 mM dye solution and then in desorption solution (0.1 M triethylamine in CH_2Cl_2) again for over 3 days. The absorbance of prepared desorption solution was recorded by UV-vis spectrophotometer.

For an exact comparison, the absorbance spectra were normalized and separated by soaking time (**Figure 3.9**). After 1 min, **RK-4** (477 nm) showed drastic blue-shift despite the lowest dye loading amount, followed by **RK-3** (487 nm) and **2** (492 nm). This indicates the severe H-aggregation of **RK-4** due to the longest alkyl chain. However, the absorption peak of **RK-2** (466 nm) rapidly blue-shifted over the rest (487 nm for **RK-3** and 474 nm for **RK-4**) after 2 min, which was attributed to the largest dye amount as shown in **Table 3.3**. In contrast, the absorption peak of **RK-3** in 2 min was still non-shifted from that (487 nm) of 20 μM solution state, indicating the least H-aggregation. After 3 min, **RK-3** started a blue-shift to 478 nm, but less than **RK-2** (475 nm). These results suggest that the largest dye adsorption of **RK-2** leads to the more H-aggregation than **RK-3**. Hence, the only **RK-2** exhibited the saturated absorption intensity from 30 min. Based on these results, we proposed dye adsorption processes for **RK-2** and **3** (**Figure 3.10**). The **RK-2** showed a high dye adsorption rate on the TiO_2 surface from 1 min and formed the compact dye monolayer within 2 min. In case of **RK-3**, similar trend is observed, but with slower dye adsorption rate and thereby, formed relatively less aggregated layer than **RK-2**. These results were further confirmed by transient photoluminescence (PL) study later.

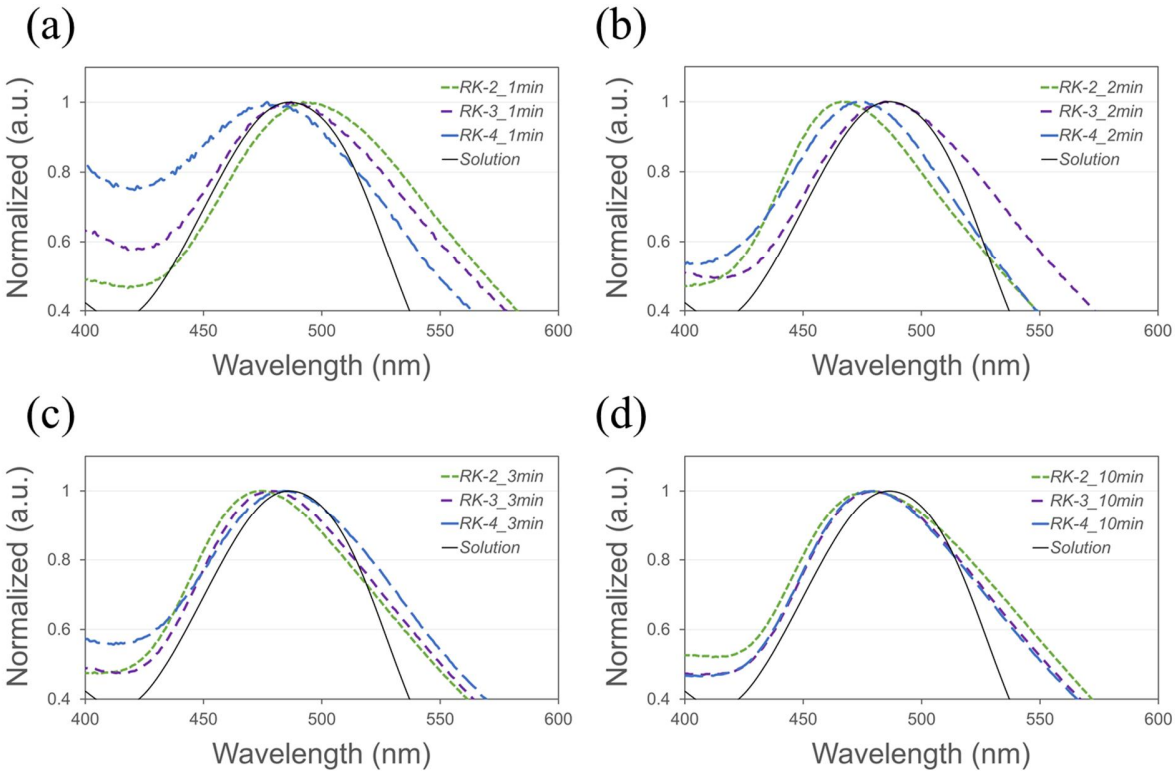

Figure 3.9 Normalized absorbance spectra separated by the soaking time until 10 min, derived from **Figure 3.8**. Focus on the change in order of blue-shift of absorption peak. All the dye loading amount values are summarized in **Table 3.3**.

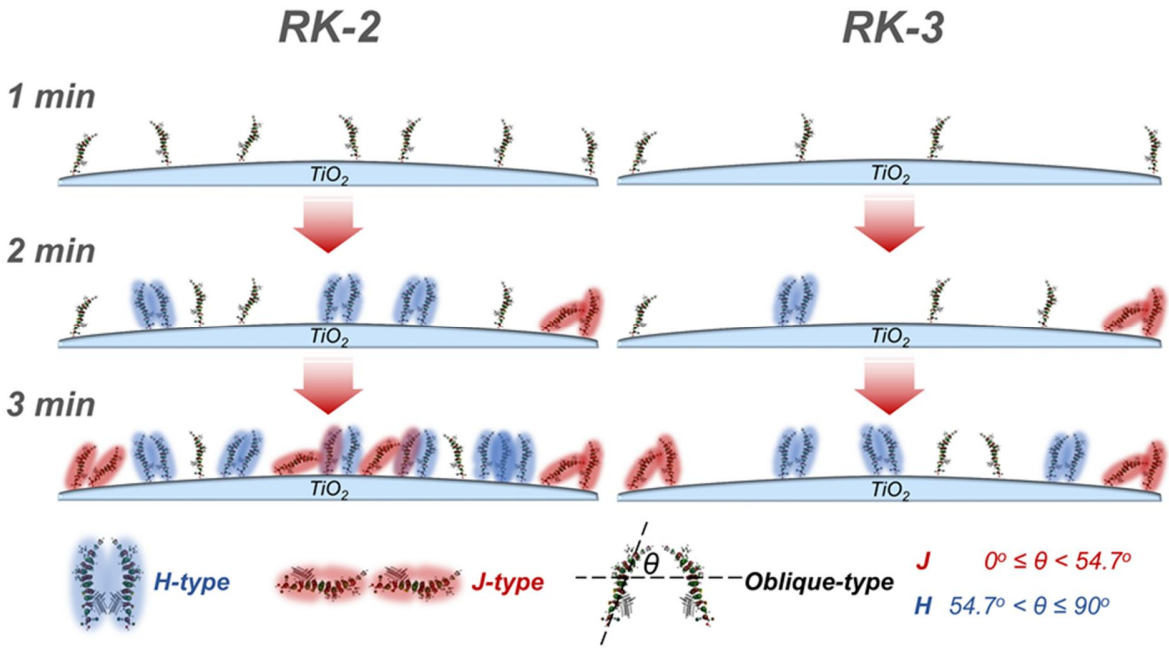

Figure 3.10 Proposed dye adsorption processes according to the alkyl chain length. **RK-2** is featured by low aggregation rate and fast adsorption rate. In case of **RK-3**, similar trend is shown with slower adsorption rate. Lower part shows various aggregation type, H-type, J-type and oblique-type. The ratio between them determines the position of absorption peak. Any co-adsorbate was not used.

Time-correlated single photon counting (TCSPC) was employed for acquiring each exciton lifetime, which informed that the degree of dye aggregation. Dummy cells were prepared, which consisted of FTO glass including a dyed zirconium dioxide (ZrO_2) layer and pure FTO glass as the counterpart and were filled with the inert electrolyte containing only additives as illustrated in **Figure 3.15**. In the dummy cell, the excited photoelectrons are not injected into the conduction band of the ZrO_2 nanoparticles because of their higher energy level. In this case, exciton lifetime in dye is strongly affected by surrounding dyes. The **RK-3** dummy cells exhibited the longest average exciton lifetime (739 ps) followed by **RK-2** (391 ps), **4** (222 ps) and **1** (185 ps), as shown in **Figure 3.11** and **Table 3.4**. This indicates the least self-quenching by aggregation in the **RK-3** based film and thus, the highest η_{inj} with **RK-3**, well matching with the calculated η_{inj} as well as film absorption trend.

The light harvesting efficiency (η_{lh}) was determined by the molar extinction coefficient and dye loading amount per projected region in the film ($\eta_{lh} = 1 - 10^{-\varepsilon lc} = 1 - 10^{A}$).[27] All dyes exhibited a negligible difference in the molar extinction coefficient from 6.74 to 7.02 × 10^4 $cm^{-1} \cdot M^{-1}$. Therefore, only dye loading can affect η_{lh}. The dye loading amount is presented in **Table 3.3**. **RK-2** with heptyl groups provides the highest dye loading amount (4.41 × 10^{-8} $mole \cdot cm^{-2}$ for 1.8-μm and 7.86 × 10^{-8} $mole \cdot cm^{-2}$ for 3.5-μm TiO_2 film) after the same soaking time. **RK-1** and **3** provide a similar amount while **RK-4** shows the smallest amount. These trends correspond to η_{lh}, as shown in **Figure 3.12**. **RK-2** achieved the highest η_{lh} in both 1.8-μm and 3.5-μm TiO_2 film, despite the slightly blue-shifted onset point in the η_{lh} spectra compared to other dyes.

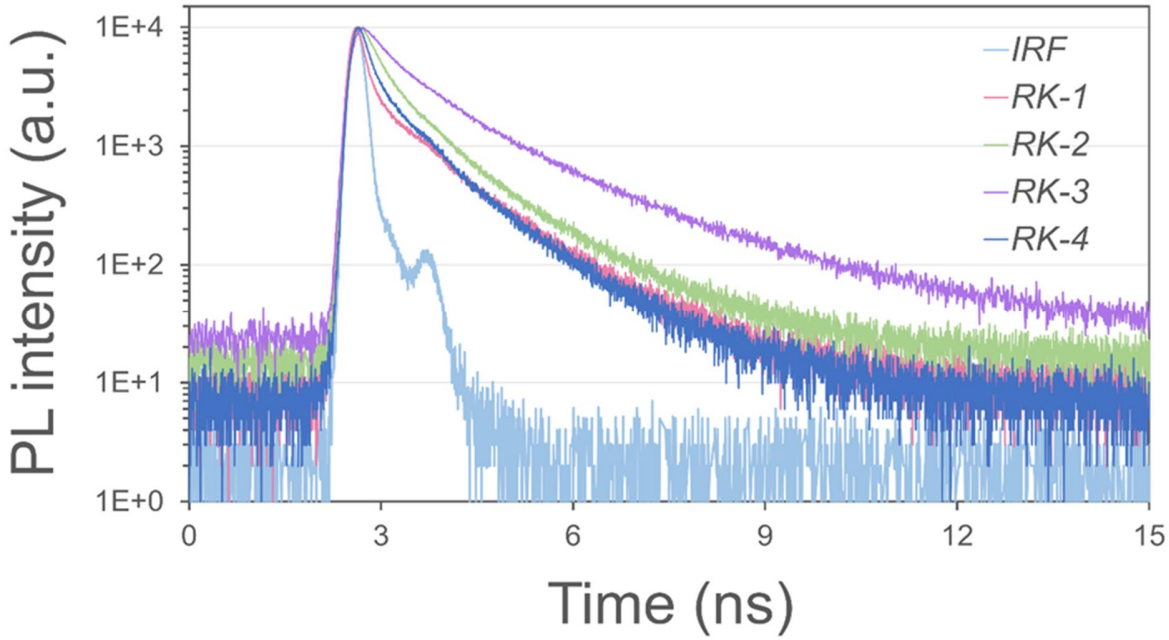

Figure 3.11 Time-resolved PL signals from the **RK** dye-sensitized ZrO_2 layer surrounded by inert electrolyte. The excitation and detection were at 506 nm and 680 nm.

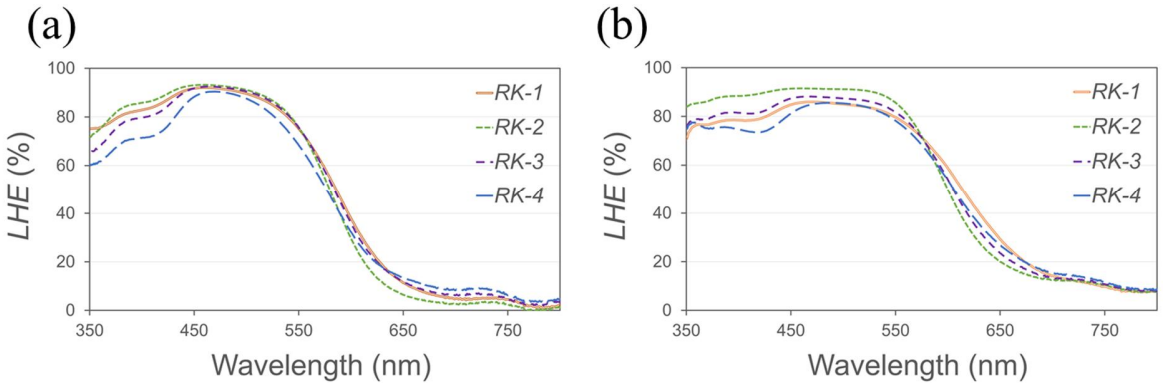

Figure 3.12 Light harvesting efficiency of **RK** dye-sensitized TiO_2 film according to film thickness: (a) 1.8-μm and (b) 3.5-μm. Taking account of only semiconductor side irradiation, diffuse reflectance and transmission of dyed TiO_2 film were measured for evaluating η_{lh} of **RK** series. Using those it was possible to obtain accurate information because not only specular but scattering rays were caught for characterizing optical ability. Excluding optical losses by the FTO and mesoporous TiO_2 layer, we obtained absorption data from the only dye monolayer.

The charge transfer kinetics in the active layer has been considered one of the most influential factors in the performance of DSCs. The competition between charge collection and recombination is quantitatively explained using charge transport time (τ_d) and recombination time (τ_{rec}). Controlled intensity modulated photo spectroscopy (CIMPS) was employed for the estimations, and the experimental details are described in the Supporting Information. **Figure 3.13a–3.13d** show the τ_d and τ_{rec} of photoinjected electrons as a function of the J_{SC} and charge amount stored in the active layer. As shown in **Figure 3.13a** and **3.13b**, except for the case of **RK-1**, all τ_d values were very similar, regardless of film thickness. However, **RK-2** DSCs exhibited the longest τ_{rec} in both the 1.8-μm and 3.5-μm active layers, followed by **RK-3**, **4** and **1**, as shown in **Figure 3.13c** and **3.13d**. Using the τ_d and τ_{rec} collected from the IMPS / IMVS responses, the diffusion length ($L_n = \sqrt{D_n \tau_{rec}}$) and collection efficiency ($\eta_{cc} = 1 - \tau_d/\tau_{rec}$) of the photoinjected electrons were determined, respectively.[28] As a result, **RK-2** achieved the longest L_n in both the active layer thicknesses, as shown in **Figure 3.13e** and **3.13f**, due to the longest τ_{rec}. The maximum η_{cc} was achieved with **RK-2** in both active layer thicknesses, followed by **RK-3** (**Figure 3.13g** and **3.13h**). Although the difference of η_{cc} between **RK-2** and **3** was very small, there was a clear distinction in diffusion length. The outstanding charge transfer characteristics in the **RK-2** DSCs was attributed to the compact dye surface coverage on the TiO_2 nanoparticles.

The compact dye surface coverage minimizes the interfacial area contacting the electrolyte, resulting in the highest η_{cc} for **RK-2**, but it can be detrimental to the charge injection. Accordingly, **RK-2** manifests a far superior τ_{rec} and thus L_n at both active layer thicknesses, but better J_{SC} was provided by **RK-3** at the 1.8-μm active layer. This result indicates that the η_{cc} is more influential in the J_{SC} than η_{inj} with increasing active layer thickness.

To confirm this result, an additional investigation of the charge collection process was performed in terms of the charge recombination resistance (R_{rec}) using electrochemical impedance spectroscopy (EIS). The obtained Nyquist plots with respect to both active layer thickness are presented in **Figure 3.14a** and **3.14b**. At both active layer thicknesses, the largest R_{rec} values (105.5 Ω for 1.8-μm and 265.6 Ω for 3.5-μm) were produced by **RK-2** DSCs, followed by **RK-3**, **4**, and **1**, which was attributed to the compact dye surface coverage. Additionally, the trend of τ_{rec} measured by EIS corresponds to that by IMVS.

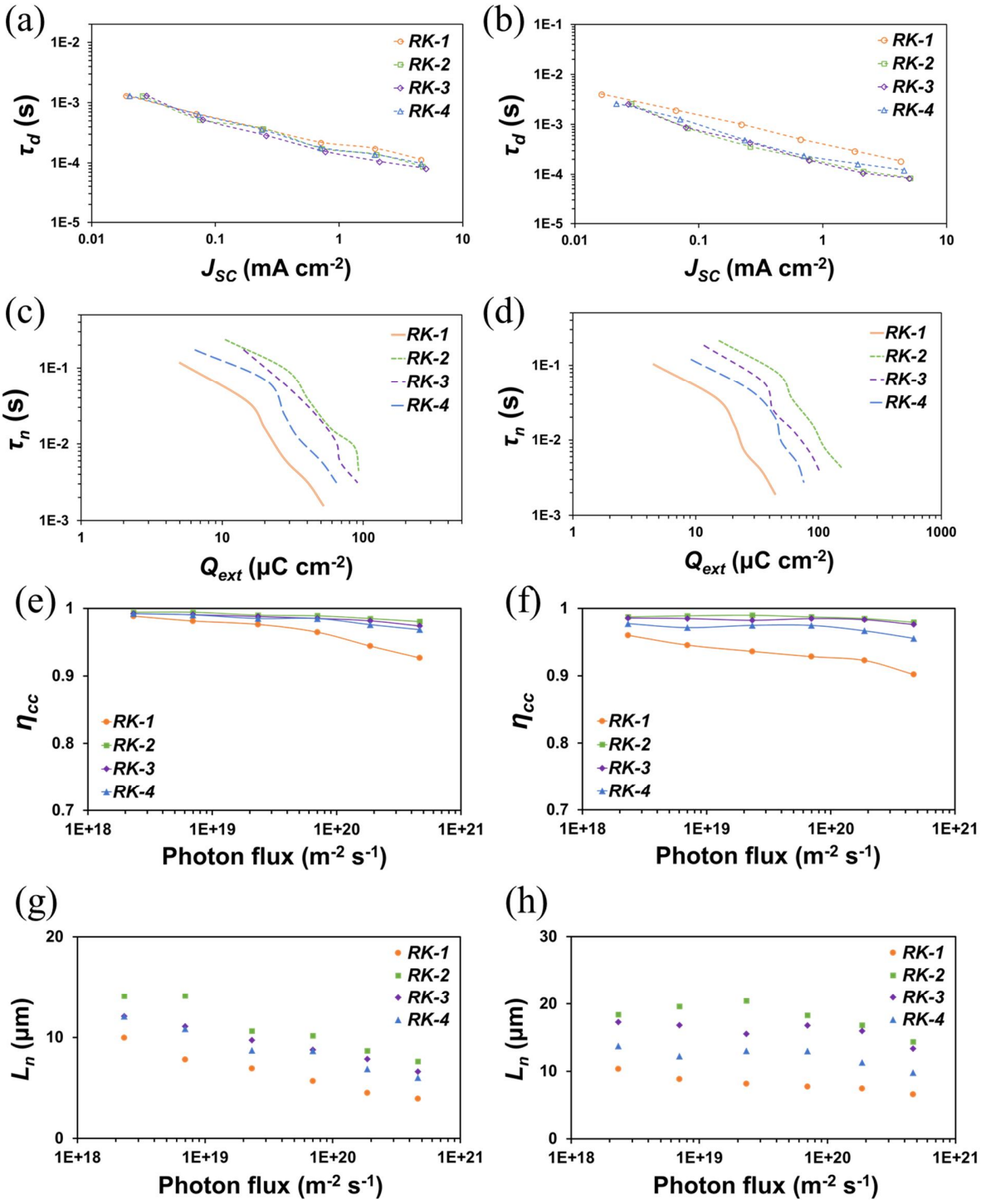

Figure 3.13 The trend of charge transport time, recombination time, collection efficiency, and diffusion length depending on the TiO_2 thickness: (a, c, e, g) 1.8-μm and (b, d, f, h) 3.5-μm.

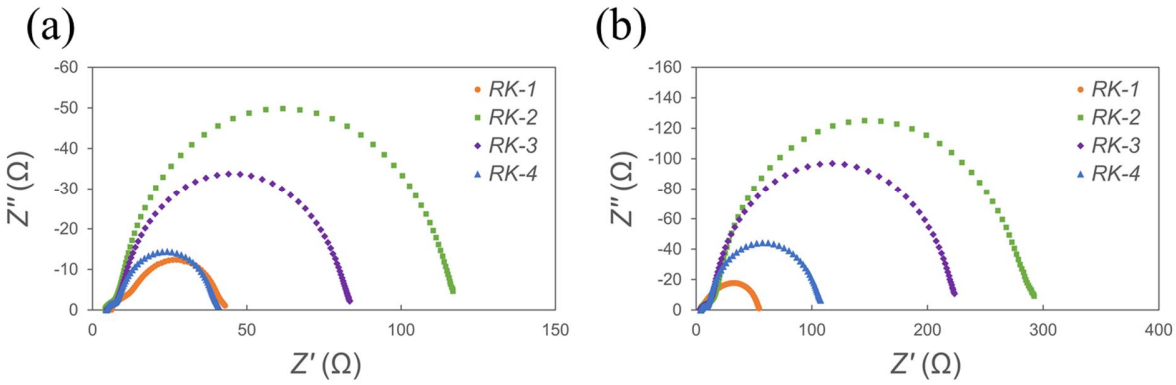

Figure 3.14 Impedance spectra in Nyquist plots depending on the TiO_2 thickness: (a) 1.8-μm and (b) 3.5-μm. EIS was measured under a dark condition, applying a 10 mV AC sinusoidal modulation superimposed on constant DC bias (-0.6 V) with the frequency ranging from 10^5 to 10^{-1} Hz.

The regeneration yield (η_{reg}) was also carefully considered as a main factor for the J_{SC} trend.[29-30] The ZrO_2-based dummy cells used for studying the dye aggregation were employed both with I^-/I_3^- couples (iodine electrolyte) and without (inert electrolyte). With an inert electrolyte, the exciton lifetime was dependent on the degree of dye aggregation. However, with the iodine electrolyte, better charge regeneration of the oxidized dye can result in a reduced exciton lifetime. **Figure 3.15** illustrates the structure of dummy cells and the mechanism for data acquisition. With these, η_{reg} is estimated as Eq.3.2:

$$\eta_{reg} = 1 - (\tau_{Iodine}/\tau_{Inert}) \quad (3.2)$$

where τ_{Iodine} is the exciton lifetime obtained from the dummy cells filled with the iodine electrolyte and τ_{Inert} is one with an inert electrolyte containing only additives. In this manner, the changes in η_{reg} depending on the ratio of I─/I3─ couple concentration was first studied in iodine electrolyte compared to the standard (100%) iodine electrolyte. **Figure 3.16** shows the PL decay signals from the **RK-2** dye-sensitized ZrO_2 layer as a function of the percentage of the I^-/I_3^- couple in the iodine electrolyte versus standard iodine electrolyte. The transient PL spectra show a gradually increasing gradient with increasing I^-/I_3^- couple concentration. All quantitative values are summarized in **Table 3.4**. The average exciton lifetime obtained from the **RK-2** dummy cells

gradually decreases from 391 ps for the inert electrolyte to 312 ps for 1%, 147 ps for 10%, and 47 ps for 100% iodine electrolyte, corresponding to 0.20, 0.62, and 0.88 η_{reg}, respectively. These sensitive changes imply that our newly developed method provides reliable information and can be applied to evaluating η_{reg}. Considering the small free energy gap between the HOMO level of **RK-2** and I^-/I_3^- redox potential, a good η_{reg} of **RK-2** may be related to the high electrochemical reactivity and stability of **RK** series. As shown in **Table 3.4**, **RK-2** dummy cells provide the highest η_{reg} (0.88) as followed by **RK-3** (0.83), **4** (0.78) and **1** (0.71). The tendency of η_{reg} is overall consistent with the alkyl chain length except for **RK-1**. **RK-1** dyes with methyl groups suffer from serious intermolecular stacking on the ZrO_2 film and have trouble in the regeneration process. Based on these findings, the alkyl chain interrupts the redox ion diffusion, thus causing unexpected bottlenecks in the operation of DSCs, such as mass transfer of I^- ions during the regeneration process and I_3^- ion escape from the active layer after regenerating dyes. These undesirable effects become stronger with increasing active layer thickness, as shown in the performance of DSCs with a 5.1-μm active layer.

To clearly understand the difference in device performance depending on the active layer thickness, all factors (η_{inj}, η_{lh}, η_{cc}, and η_{reg}) affecting the J_{SC} were considered. As mentioned above, at both active layer thicknesses, **RK-3** achieved the best η_{inj} while **RK-2** obtained the best η_{lh}, η_{cc}, and η_{reg}. As for the PCE, **RK-3** provided the highest PCE (9.1%) in the 1.8-μm active layer, which means that η_{inj} played a dominant role in the performance of DSC. In contrast, **RK-2** provided the best PCE (8.8%) in a 3.5-μm active layer because the charge collection and regeneration became more important as the film thickness increased.

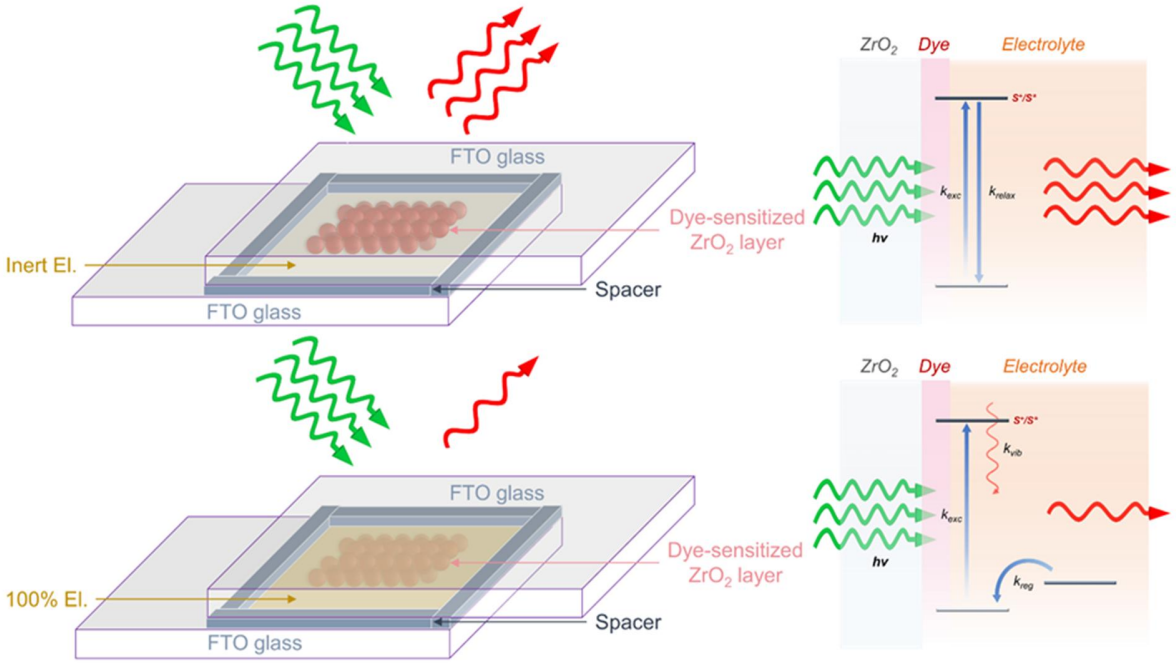

Figure 3.15 Structure of the dummy cell used for the exciton lifetime and regeneration yield acquisition. Excited photoelectrons in the dyed ZrO_2 layer self-relax through radiative emission (upper). Addition of I^-/I_3^- couples into the electrolyte leads to a decrease in radiative emission because the electron vacancy, i.e., hole, is occupied during the regeneration process with stray photoexcited electrons thermalized (lower).

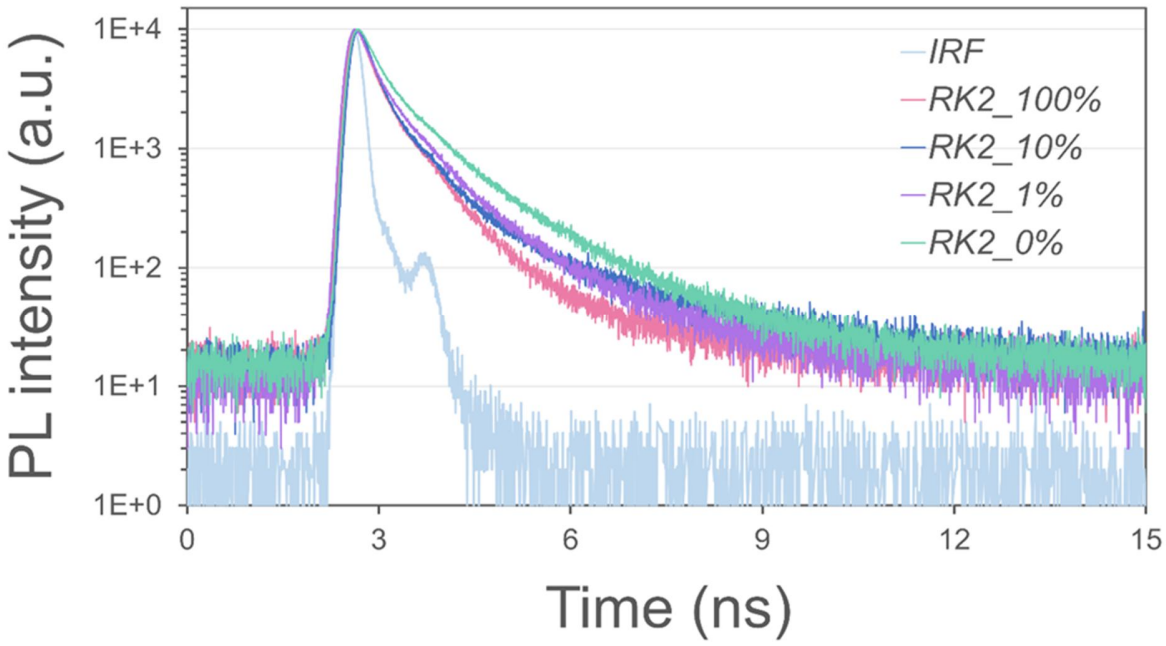

Figure 3.16 Time-resolved PL signals from the **RK-2** dye-sensitized ZrO_2 layer depending on the iodine electrolyte concentration. The excitation and detection were at 506 nm and 680 nm.

Table 3.4. Calculated average exciton lifetimes and corresponding η_{reg} depending on the I^-/I_3^- couple concentration. All η_{reg} values were calculated using the inert electrolyte as a standard.

	Iodine 0% (Inert)		Iodine 1%		Iodine 10%		Iodine 100% (Standard)	
	τ_{ext}[a] (ps)	η_{reg}	τ_{ext}[a] (ps)	η_{reg}	τ_{ext}[a] (ps)	η_{reg}	τ_{ext}[a] (ps)	η_{reg}
RK-1	185	0	N/A	N/A	N/A	N/A	54	0.71
RK-2	391	0	312	0.20	147	0.62	47	0.88
RK-3	739	0	N/A	N/A	N/A	N/A	125	0.83
RK-4	222	0	N/A	N/A	N/A	N/A	49	0.78

[a] Exciton lifetime was estimated by fitting transient PL spectra, followed by equalization of the whole spectra. FlouFit software was employed for fitting with a multi exponential model, $I(t) = \int_{-\infty}^{t} IRF(t') \sum_{t=1}^{n} A_i e^{-(t-t'/\tau_i)}\, dt'$, where *IRF(t')* is the experimentally measured instrument response function (lamp function), A_i is the amplitude of the i^{th} component at time zero in counts, τ_i is the lifetime of the i^{th} component and t is the time shift between *IRF(t')* and decay. For determining the average exciton lifetime, three exponential functions were used and quantitative values were derived from the resulting fitting signals by equalizing fitting signals as follows: $I(t) = A_1 e^{-(t/\tau_1)} + A_2 e^{-(t/\tau_2)} + A_3 e^{-(t/\tau_3)}$.

Finally, the J_{SC} trend was confirmed by the incident photon to current conversion efficiency (IPCE) measurement, as shown in **Figure 3.17**. The overall spectra matches the η_{lh} profile with spectral response onsets at approximately 750 nm. At both active layer thicknesses, the tendency of IPCE is in accordance with the J_{SC} variation. In the 1.8-μm active layer, **RK-3** exhibited the highest IPCE values followed by **RK-2**, **4**, and **1** while in the 3.5-μm active layer, **RK-2** achieved the highest IPCE values, followed by **RK-3**, **4**, and **1**. Notably, the IPCE was measured under no bias light and a chopping frequency of 4 Hz was used because of instrument limitations. Xiao-Zhi Guo et al. recommended that the IPCE measurement be performed under white bias light using low chopping frequency below 1 Hz for DSCs due to their slow response time.[31] Under these measurement conditions, the IPCE would be considerably underestimated. Nevertheless, a reliable J_{SC} trend was observed and conforming to that obtained under a one sun condition, supporting our analyses.

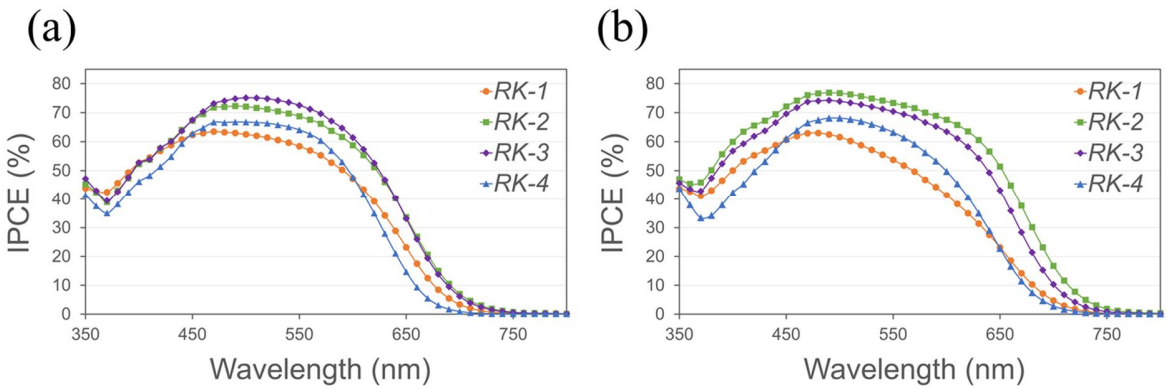

Figure 3.17 Incident photon-to-current conversion efficiency of **RK** DSCs, presented according to the TiO_2 film thickness: (a) 1.8-μm and (b) 3.5-μm.

3.3 Conclusion

New indoline derivatives were successfully synthesized and applied to dye-sensitized solar cells (DSCs) as sensitizers, named **RK-1**, **2**, **3** and **4**. The derivatives have a planar structure and high molar extinction coefficient, facilitating a high power conversion efficiency (PCE), even with a very thin TiO_2 film. Alkyl chain groups with a variable length were introduced to prevent serious intermolecular stacking and to optimize the performance of DSCs. Too Long alkyl chain groups caused dye aggregation and decreased the dye loading amount, also blocked I^- ion diffusion during the regeneration. However, the moderate alkyl chains facilitated the compact dye surface coverage, shielding photoelectrons injected against the oxidized redox mediators. Thus, DSC performances according to the alkyl chain length showed varying photocurrent densities (J_{SC}) as well as dependence on the active layer thickness. As a result, **RK-3** showed superior J_{SC} only at a 1.8-μm active layer and thus the best PCE of 9.1% (V_{OC} = 0.74 V, J_{SC} = 16.2 mA· cm^{-2} and FF = 0.76) under one sun illumination (AM 1.5, 1000 W·m^{-2}) because of the most favorable charge injection kinetics. To the best of our knowledge, this is the best performance of DSCs at the same film thickness. However, **RK-2** provided the best PCE of 8.8% when increasing the active layer thickness to 3.5-μm. These results imply that the most influential factor for J_{SC} was charge injection in a very thin active layer (1.8-μm), but charge collection and regeneration gradually became more influential with increasing active layer thickness.

In summary, at a very thin active layer (< 2-μm), charge injection plays a major role in determining the device performance of indoline-based **RK** series that have a large molar extinction coefficient with a large planar geometry. By increasing the active layer thickness, the device performance of **RK** series gradually decreased and the charge collection and regeneration became dominant factors as opposed to the charge injection. Thus, this study guides the future research on organic sensitizer design for thin film and flexible-type DSCs.

3.4 Experimental Section

Dummy cell fabrication The whole process is similar to the DSC fabrication process. For preparing photoactive ZrO_2 films, FTO glass was first ultrasonically cleaned with acetone, ethanol, and DI water for 10 min, in that order. Cleaned FTO glass was covered with ZrO_2 paste by the screen printing method, followed by sintering at 500 °C for 30 min. ZrO_2 paste was produced as follows: 0.4 ml of acetic acid, 0.6 ml of acetylacetone, 3.33 g of α-terpineol, 5 g of ethyl cellulose, and 1 g of ZrO_2 powder were added to ethanol with magnetic stirring followed by ultrasonic treatment for 3 h. The mixture solution was then vigorously stirred for 24 h for good dispersion of ZrO_2 nanoparticles. The resulting solution was gradually evaporated at 50 °C with magnetic stirring until a paste was properly formed. Screen printed mesoporous ZrO_2 film was immersed in a dye solution (0.2 mM in $CHCl_3$) at room temperature under a dark condition for 150 min and then assembled with perforated pure FTO glass into a sandwich configuration, followed by injection of the same iodine electrolyte. For testing, the concentration of I_2, LiI, and DMPII was controlled with the others remaining the same.

Photoelectrochemical characterization The current density-voltage (J-V) characteristic was evaluated using a digital source meter (Series 2600A, Keithley Instruments, Inc.) under one sun illumination (AM 1.5, 1000 $W \cdot m^{-2}$) simulated by a photovoltaic efficiency measurement system (IQE-200, Newport Corporation). For preventing overestimation, a black mask (0.5 × 0.5 cm^2) was attached to the DSCs each time.

Controlled intensity modulated photo spectroscopy (CIMPS) spectra were acquired from the electrochemical workstation (ZENNIUM XPOT, ZAHNER-elektrik GmbH & Co. KG) with a frequency response analyzer under an intensity-controlled monochromatic LED (463 nm). The photocurrent density and corresponding external quantum efficiency (η_{EQE}) as a function of the monochromatic light intensity were measured under black mask as well using the same electrochemical workstation. The measurement was performed under the low light intensity to minimize the side effects, such as the Stark effect[32] and RC limitation[33] at excess charge concentration, such that more exact information was acquired. The η_{EQE} was automatically calculated by Thales software (ZAHNER-elektrik GmbH & Co. KG) using a spectral responsivity equation ($\eta_{EQE} = J_{SC} \cdot h \cdot c / P \cdot \lambda \cdot q_e$), where J_{SC} ($mA \cdot cm^{-2}$) is the short circuit current density, h ($J \cdot s$) is the natural Plank constant, c ($m \cdot s^{-1}$) is the vacuum speed of light, P ($W \cdot m^{-2}$) is the specific light intensity, λ (m) is the wavelength and q_e (C) is the electron's elementary charge.[34]

Electrochemical impedance spectroscopy (EIS) was performed on the electrochemical analysis system (Model 1287A Potentiostat and 1260A Impedance / Gain-phase analyzer combined, Solartron Analytical, AMETEK, Inc.) in a dark condition, applying a 10 mV AC sinusoidal signal superimposed on constant

forward bias with the frequency ranging from 10^5 to 10^{-1} Hz. Z View software (Scribner Associates, Inc.) was used for fitting Nyquist plots.

Time-correlated single photon counting (TCSPC) was performed with a tunable Ti:sapphire laser (Mira900, Coherent) as an excitation source. The PL signal was spectrally resolved by a monochromator (SP-2150i, Acton) and corresponding signals were quickly detected by the TCSPC module (PicoHarp, PicoQuant) with a MCP-PMT (R3809U-59, Hamamatsu). Time-resolved PL signals were fit using fluorescence decay data analysis software (FlouFit, PicoQuant).

Incident photon to current conversion efficiency (IPCE) measurements were performed using an EQE system (Model QEX7, PV Measurements, Inc.) in the AC mode with a chopping frequency of 4 Hz under a dark condition.

Film absorption test All the dye solutions were sonicated before sensitization to disintegrate stacked dye molecules. To catch even the fine distinctions, we repeatedly used identical TiO_2 film samples for absorption test after refreshing every time by immersing in desorption solution (0.1 M triethylamine in CH_2Cl_2) for 30 min, washing with CH_2Cl_2, and lastly sintering at 500 °C for 30 min in air. This must minimize the error range that results from the fine difference in TiO_2 film thickness between samples. For estimating dye loading amount, dye-adsorbed TiO_2 films were firstly immersed in desorption solution (0.1 M triethylamine in CH_2Cl_2) for over 3 days. The absorbance spectra of prepared desorption solution were recorded by UV-vis spectrophotometer. Finally, dye concentrations were calculated using Beer Lambert law ($A = \varepsilon lc$), where A is the absorbance intensity of desorption solution, ε is the molar extinction coefficient, l is the optical path length and c is the molar concentration.

REFERENCE

1. Ito, S.; Murakami, T. N.; Comte, P.; Liska, P.; Grätzel, C.; Nazeeruddin, M. K.; Grätzel, M., Fabrication of thin film dye sensitized solar cells with solar to electric power conversion efficiency over 10%. *Thin Solid Films* **2008,** *516* (14), 4613-4619.

2. Hagfeldt, A.; Boschloo, G.; Sun, L.; Kloo, L.; Pettersson, H., Dye-sensitized solar cells. *Chem. Rev.* **2010,** *110* (11), 6595-6663.

3. Kojima, A.; Teshima, K.; Shirai, Y.; Miyasaka, T., Organometal halide perovskites as visible-light sensitizers for photovoltaic cells. *J. Am. Chem. Soc.* **2009,** *131* (17), 6050-6051.

4. Barrows, A. T.; Pearson, A. J.; Kwak, C. K.; Dunbar, A. D.; Buckley, A. R.; Lidzey, D. G., Efficient planar heterojunction mixed-halide perovskite solar cells deposited via spray-deposition. *Energy Environ. Sci.* **2014,** *7* (9), 2944-2950.

5. Yang, W. S.; Noh, J. H.; Jeon, N. J.; Kim, Y. C.; Ryu, S.; Seo, J.; Seok, S. I., High-performance photovoltaic perovskite layers fabricated through intramolecular exchange. *Science* **2015,** *348* (6240), 1234-1237.

6. Nasiri, A.; Zabalawi, S. A.; Mandic, G., Indoor power harvesting using photovoltaic cells for low-power applications. *IEEE Trans. Ind. Electron.* **2009,** *56* (11), 4502-4509.

7. Lee, K.; Park, S. W.; Ko, M. J.; Kim, K.; Park, N.-G., Selective positioning of organic dyes in a mesoporous inorganic oxide film. *Nat. Mater.* **2009,** *8* (8), 665.

8. Snaith, H. J.; Schmidt□Mende, L., Advances in liquid□electrolyte and solid□state dye□sensitized solar cells. *Adv. Mater.* **2007,** *19* (20), 3187-3200.

9. Han, H.-G.; Weerasinghe, H. C.; Kim, K. M.; Kim, J. S.; Cheng, Y.-B.; Jones, D. J.; Holmes, A. B.; Kwon, T.-H., Ultrafast fabrication of flexible dye-sensitized solar cells by ultrasonic spray-coating technology. *Sci. Rep.* **2015,** *5*, 14645.

10. Hara, K.; Sayama, K.; Ohga, Y.; Shinpo, A.; Suga, S.; Arakawa, H., A coumarin-derivative dye sensitized nanocrystalline TiO2 solar cell having a high solar-energy conversion efficiency up to 5.6%. *Chem. Commun.* **2001,** (6), 569-570.

11. Hara, K.; Sato, T.; Katoh, R.; Furube, A.; Yoshihara, T.; Murai, M.; Kurashige, M.; Ito, S.; Shinpo, A.; Suga, S., Novel Conjugated Organic Dyes for Efficient Dye□Sensitized Solar Cells. *Adv. Funct. Mater.* **2005,** *15* (2), 246-252.

12. Wang, Z.-S.; Koumura, N.; Cui, Y.; Takahashi, M.; Sekiguchi, H.; Mori, A.; Kubo, T.; Furube, A.; Hara, K., Hexylthiophene-functionalized carbazole dyes for efficient molecular photovoltaics: tuning of solar-cell performance by structural modification. *Chem. Mater.* **2008,** *20* (12), 3993-4003.

13. Dessì, A.; Calamante, M.; Mordini, A.; Peruzzini, M.; Sinicropi, A.; Basosi, R.; de Biani, F. F.; Taddei, M.; Colonna, D.; Di Carlo, A., Organic dyes with intense light absorption especially suitable for application in thin-layer dye-sensitized solar cells. *Chem. Commun.* **2014,** *50* (90), 13952-13955.

14. Chai, Z.; Wu, M.; Fang, M.; Wan, S.; Xu, T.; Tang, R.; Xie, Y.; Mei, A.; Han, H.; Li, Q., Similar or Totally Different: the Adjustment of the Twist Conformation Through Minor Structural Modification, and Dramatically Improved Performance for Dye□Sensitized Solar Cell. *Adv. Energy Mater.* **2015,** *5* (18).

15. Yao, Z.; Zhang, M.; Li, R.; Yang, L.; Qiao, Y.; Wang, P., A Metal□Free N□Annulated Thienocyclopentaperylene Dye: Power Conversion Efficiency of 12% for Dye□Sensitized Solar Cells. *Angew. Chem., Int. Ed.* **2015,** *127* (20), 6092-6096.

16. Ito, S.; Miura, H.; Uchida, S.; Takata, M.; Sumioka, K.; Liska, P.; Comte, P.; Péchy, P.; Grätzel, M., High-conversion-efficiency organic dye-sensitized solar cells with a novel indoline dye. *Chem. Commun.* **2008,** (41), 5194-5196.

17. Nishida, J.-i.; Masuko, T.; Cui, Y.; Hara, K.; Shibuya, H.; Ihara, M.; Hosoyama, T.; Goto, R.; Mori, S.; Yamashita, Y., Molecular design of organic dye toward retardation of charge recombination at semiconductor/dye/electrolyte interface: introduction of twisted π-linker. *J. Phys. Chem. C* **2010,** *114* (41), 17920-17925.

18. Kanetada, N.; Matsumura, C.; Yamazaki, S.; Adachi, K., Mechanism of Peripheral Substituent Effects on Adsorption–Aggregation Behaviors of Cationic Porphyrin Dyes on Tungsten (VI) Oxide Nanocolloid Particles. *ACS Appl. Mater. Interfaces* **2013,** *5* (24), 12991-12999.

19. Seo, S. H.; Jeong, E. J.; Han, J. T.; Kang, H. C.; Cha, S. I.; Lee, D. Y.; Lee, G.-W., Efficient low-temperature transparent electrocatalytic layers based on graphene oxide nanosheets for dye-sensitized solar cells. *ACS Appl. Mater. Interfaces* **2015,** *7* (20), 10863-10871.

20. Boschloo, G.; Hagfeldt, A., Characteristics of the iodide/triiodide redox mediator in dye-sensitized solar cells. *Acc. Chem. Res.* **2009,** *42* (11), 1819-1826.

21. Feldt, S. M.; Wang, G.; Boschloo, G.; Hagfeldt, A., Effects of driving forces for recombination and regeneration on the photovoltaic performance of dye-sensitized solar cells using cobalt polypyridine redox couples. *J. Phys. Chem. C* **2011,** *115* (43), 21500-21507.

22. Katoh, R.; Furube, A., Electron injection efficiency in dye-sensitized solar cells. *J. Photochem. Photobiol., C* **2014,** *20*, 1-16.

23. Kwon, T.-H.; Armel, V.; Nattestad, A.; MacFarlane, D. R.; Bach, U.; Lind, S. J.; Gordon, K. C.; Tang, W.; Jones, D. J.; Holmes, A. B., Dithienothiophene (DTT)-based dyes for dye-sensitized solar cells: synthesis of 2, 6-dibromo-DTT. *J. Org. Chem.* **2011,** *76* (10), 4088-4093.

24. Zhu, K.; Neale, N. R.; Miedaner, A.; Frank, A. J., Enhanced charge-collection efficiencies and light scattering in dye-sensitized solar cells using oriented TiO2 nanotubes arrays. *Nano Lett.* **2007,** *7* (1), 69-74.

25. Yella, A.; Lee, H.-W.; Tsao, H. N.; Yi, C.; Chandiran, A. K.; Nazeeruddin, M. K.; Diau, E. W.-G.; Yeh, C.-Y.; Zakeeruddin, S. M.; Grätzel, M., Porphyrin-sensitized solar cells with cobalt (II/III)–based redox electrolyte exceed 12 percent efficiency. *Science* **2011,** *334* (6056), 629-634.

26. Barnes, P. R.; Anderson, A. Y.; Koops, S. E.; Durrant, J. R.; O'Regan, B. C., Electron injection efficiency and diffusion length in dye-sensitized solar cells derived from incident photon conversion efficiency measurements. *J. Phys. Chem. C* **2008,** *113* (3), 1126-1136.

27. Yum, J.-H.; Baranoff, E.; Kessler, F.; Moehl, T.; Ahmad, S.; Bessho, T.; Marchioro, A.; Ghadiri, E.; Moser, J.-E.; Yi, C., A cobalt complex redox shuttle for dye-sensitized solar cells with high open-circuit potentials. *Nat. Commun*. **2012,** *3*, 631.

28. Fabregat-Santiago, F.; Garcia-Belmonte, G.; Mora-Seró, I.; Bisquert, J., Characterization of nanostructured hybrid and organic solar cells by impedance spectroscopy. *Phys. Chem. Chem. Phys*. **2011,** *13* (20), 9083-9118.

29. Clifford, J. N.; Palomares, E.; Nazeeruddin, M. K.; Grätzel, M.; Durrant, J. R., Dye dependent regeneration dynamics in dye sensitized nanocrystalline solar cells: evidence for the formation of a ruthenium bipyridyl cation/iodide intermediate. *J. Phys. Chem. C* **2007,** *111* (17), 6561-6567.

30. Ziółek, M.; Martín, C.; Sun, L.; Douhal, A., Effect of electrolyte composition on electron injection and dye regeneration dynamics in complete organic dye sensitized solar cells probed by time-resolved laser spectroscopy. *J. Phys. Chem. C* **2012,** *116* (50), 26227-26238.

31. Guo, X.-Z.; Luo, Y.-H.; Zhang, Y.-D.; Huang, X.-C.; Li, D.-M.; Meng, Q.-B., Study on the effect of measuring methods on incident photon-to-electron conversion efficiency of dye-sensitized solar cells by home-made setup. *Rev. Sci. Instrum.* **2010,** *81* (10), 103106.

32. Pazoki, M.; Hagfeldt, A.; Boschloo, G., Stark effects in D35-sensitized mesoporous TiO2: influence of dye coverage and electrolyte composition. *Electrochim. Acta* **2015,** *179*, 174-178.

33. O'Regan, B. C.; Bakker, K.; Kroeze, J.; Smit, H.; Sommeling, P.; Durrant, J. R., Measuring charge transport from transient photovoltage rise times. A new tool to investigate electron transport in nanoparticle films. *J. Phys. Chem. B* **2006,** *110* (34), 17155-17160.

34. Rogalski, A.; Adamiec, K.; Rutkowski, J., *Narrow-Gap Semiconductor Photodiodes*. SPIE Press: Bellingham, Washington, USA, 2000; Vol. 77.

Chapter 4. Control and Monitoring of Dye Distribution in Mesoporous TiO_2 Film Improving Photovoltaic Performance

4.1 Introduction

The development of efficient, large-scale facility for inexpensive electricity generation using solar energy has attracted great research interest.[1] While a large proportion of supplied solar modules are silicon-based, the dye-sensitized solar cell (DSC) is a promising alternative. The DSC has unique advantages, such as multiple colors, transparency, flexibility, and impervious to the incident light intensity and angle.[2] The commercialization of DSCs requires efficient fabrication methods.[3-5] During the conventional fabrication procedure, the soaking process for dyeing the metal oxide film—which is usually mesoporous TiO_2—still has plenty of room for improvement. The conventional method of overnight soaking (OS) produces an unbalanced dye distribution in the porous TiO_2 film, in spite of the considerable length of time it requires. The reason is that during OS the dye molecules gradually infiltrate the film and occupy the free sites from the top to the bottom, causing severe localization of dye-occupied sites near the top.[6] Efforts to overcome these shortcomings include: using a syringe to pump dye solution into the sealed cells,[7] acid treatment to positively polarize the TiO_2 surface,[8] and activation of dye molecules using supercritical CO_2.[9] Although these methods could produce devices with outstanding power conversion efficiency (PCE) in a few minutes, they are inadequate for commercialization in terms of sustainability, mass production, and cost. Furthermore, most methods developed so far have not solved the problem of uneven dye distribution within the TiO_2 film.

In this communication, we introduce a new dye arrangement process, gas bubbling soaking (GBS), which not only provides even dye dispersion in the porous TiO_2 film for the first time, but also dramatically shortens the device fabrication time. GBS is also applicable to thick TiO_2 films (over 20-μm), suggesting its wide range of application. Consequently, the resulting device could achieve higher PCE than the best values of those produced using OS, despite a lower dye capacity. Such findings are attributed to the even dye distribution and the resulting large surface covered with dye inside the porous TiO_2 film, leading to decreased recombination of photoinjected electrons.[6] We noted that the dye capacity was not linear to the TiO_2 film thickness, especially in the case of OS. This means a large portion of dye molecules resided near the top of TiO_2 film, not the inside. Such uneven dye distribution is the main cause of limited performance in devices with thick TiO_2 film, a problem that has been little researched, but successfully overcame by GBS. We

used highly sensitive plasmon sensors to directly observe the dye infiltration into the porous nanostructure, in conjunction with time-of-flight secondary ion mass spectrometry (TOF-SIMS) depth profiles. The impact of GBS on the performance of DSCs was also intensively investigated using various photoelectrochemical analyses.

4.2 Results and discussion

Dye Capacity In the GBS process (upper part, **Figure 4.1**), the injected gas flow generates pressure across the porous TiO_2 film, carrying the dye molecules to the bottom of the film. Therefore, the running gas spreads the dye molecules widely within the porous TiO_2 film, while in OS (lower part, **Figure 4.1**) most dye molecules are localized near the top. Referring to the Langmuir adsorption model, the surface coverage of dye molecules on the film is expressed as:

$$\theta_{dye} = K_{eq}P_{dye}/1 + K_{eq}P_{dye} \quad (4.1)$$

Where θ_{dye} is the fraction of surface sites covered with dye molecules, K_{eq} is the equilibrium constant, and P_{dye} is the dye's partial pressure in the adsorption system.[10]

We first checked the adsorption capacity in the porous TiO_2 film for two dyes: a ruthenium-based dye (N719)[11] and an organic dye (DAHTDTT).[12] The results of different dyeing methods and times are summarized in **Table 4.1**. GBS consistently produces a much higher dye capacity than OS for the same soaking time. When using dilute dye solution (0.04 mM), 15 min of GBS treatment produced a dye capacity that corresponds to that of 4 h of OS in the 1.8-μm-thick TiO_2 films. It is especially more effective for thicker TiO_2 films (7-μm), indicating efficient dye infiltration into the porous nanostructure. For N719, the dye capacity after 15 min of GBS was similar to that after 7 h of OS (0.88×10^{-7} and 0.84×10^{-7} mol cm^{-2}, respectively). The variation in tonal contrast in **Figure 4.2** visually shows the different dye adsorption rates in 7-μm-thick TiO_2 films using GBS and OS. Since different carrier gases (N_2, CO_2, and air) produced similar dye capacities (**Table 4.2**), we believe that the GBS effect originates from the physical driving force of gas flow, not any chemical processes. Such findings suggest that the GBS method is promising for commercialization in terms of fabrication cost and time.

Table 4.1 Dye Capacity Data according to the Dyeing Condition

Dye	*Conc. (mM)*	*Thick. (μm)*	*Type*	*Dye capacity* [a] (× 10^{-7} mol cm^{-2})											
				Minute					Hour						
				2	4	8	15	30	1	1.5	2	3	4	5	7.5
DAHTDTT	0.04	1.8	GBS	0.14	0.16	0.26	0.37								
			OS				0.04		0.19	0.24	0.26	0.32	0.37	0.44	
	0.2	1.8	GBS	0.27	0.47	0.57	0.69	0.79							
			OS						0.63	0.71	0.89	0.99	1.08	1.24	
		7	GBS	0.39	0.51	0.89	1.20	1.43							
			OS						0.72	1.01	1.25	1.67		1.86	2.26
	1	1.8	OS	0.43	0.49	0.51	0.57	0.63	0.69		0.72				
				Minute					Hour						
					4	8	15	30	1	1.5	3	5	7	11	15
N719	0.3	1.8	GBS		0.26	0.31	0.37	0.44							
			OS					0.34	0.36	0.38	0.44	051	0.54	0.63	0.83
		7	GBS		0.57	0.81	0.88	0.91	1.02						
			OS					0.34	0.41	0.50	0.59	0.68	0.84	1.06	1.31

[a] Dye capacities were calculated from Beer–Lambert law ($A = \varepsilon lc$), where A is the absorbance intensity of desorption solution, ε is the molar extinction coefficient, l is the optical path length and c is the molar concentration. For desorption solution, we immersed dyed TiO2 film substrate in a mixture of ethanol and DI water (v/v, 7/3) containing 0.1 M NaOH for a day in case of N719 or dichloromethane containing 0.1 M trimethylamine for 3 days in case of DAHTDTT. The absorbance spectra of resulting desorption solutions were recorded by UV–vis–NIR spectrophotometer.

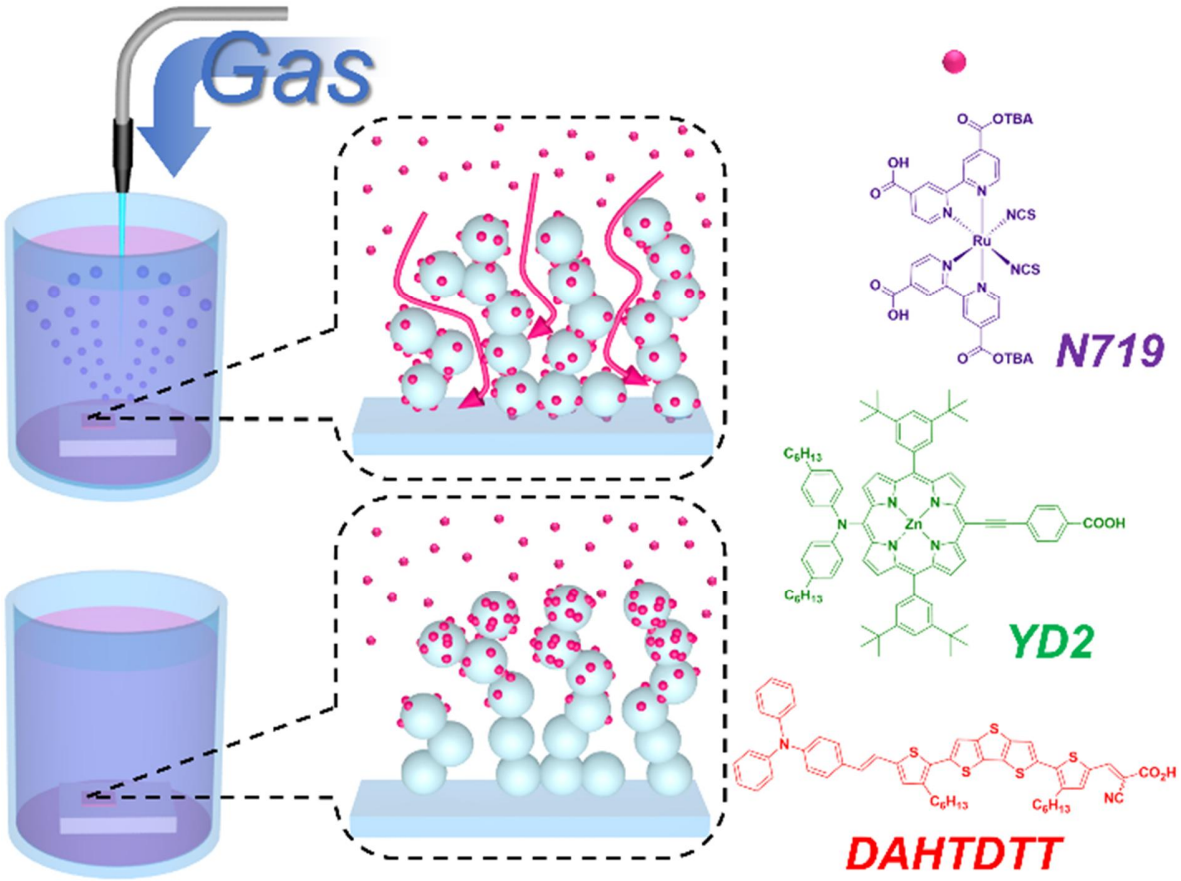

Figure 4.1 Proposed dyeing mechanisms of GBS (upper) and OS (lower), and the molecular structures of three dyes used, N719, YD2, and DAHTDTT (right). The injected gas flow pushes dye molecules deep inside the porous TiO_2 film, while the dye molecules slowly spread in the case of OS. Note that these two methods produce different dye distributions.

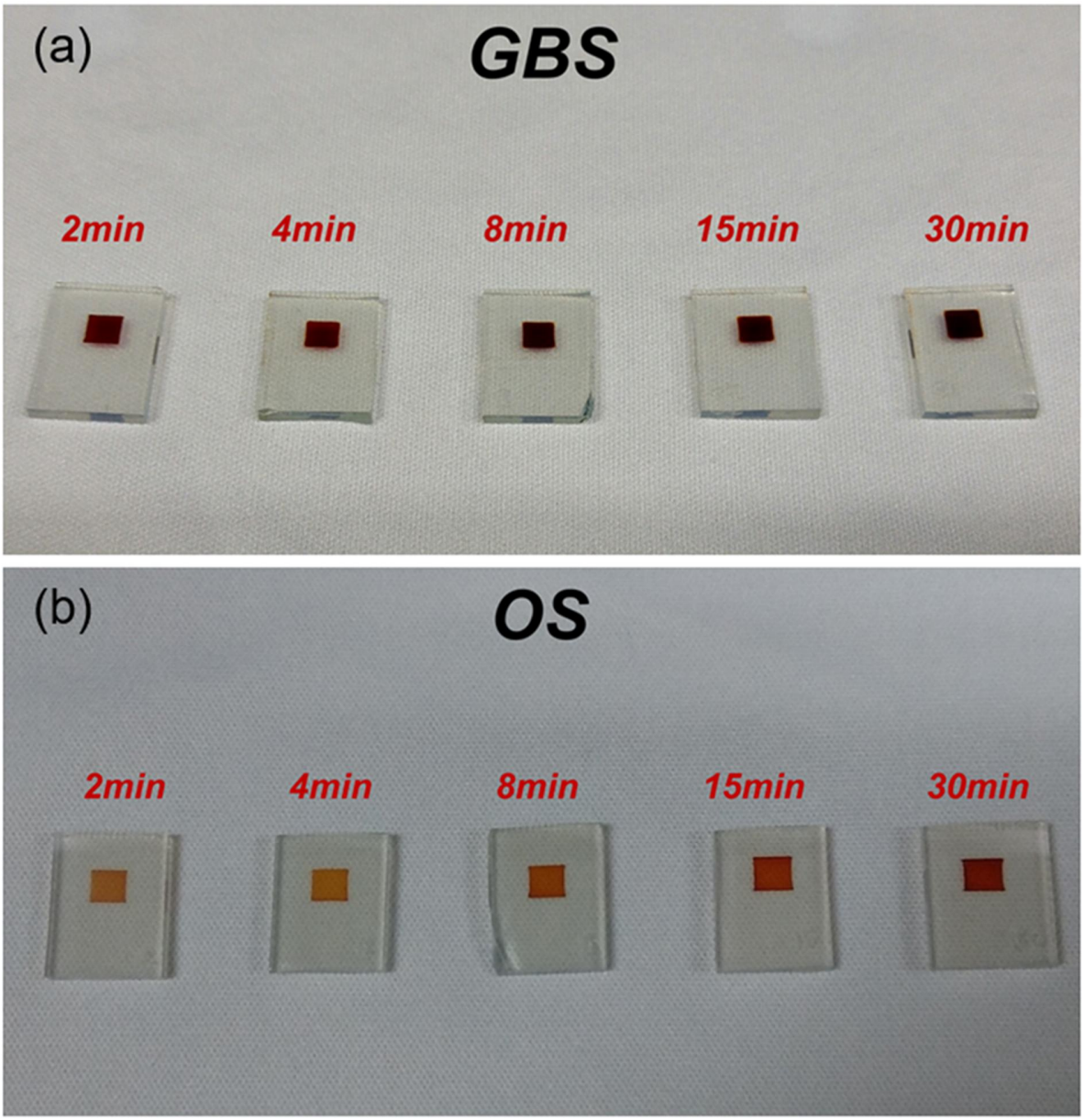

Figure 4.2 The difference in tonal contrast of 7-μm TiO_2 film according to dyeing method, (a) GBS and (b) OS, for the same time.

Table 4.2 Dye capacity for GBS according to gas type.

Dye	*Conc.* (*mM*)	*Thick.* (*μm*)	*Gas type*	*Dye capacity* [a] ($\times 10^{-7}$ mol cm^{-2})	
				Hour	
				0.5	1
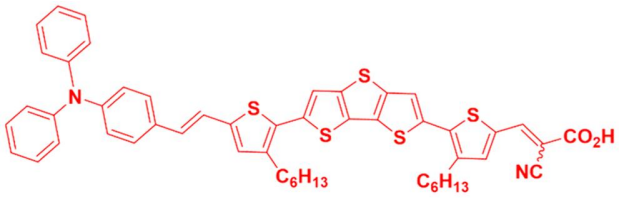 DAHTDTT	0.2	7	CO_2	1.85	2.03
			Air	1.67	2.09
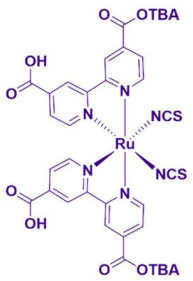 N719	0.3		CO_2	1.06	1.37
			Air	1.20	1.56

[a] Dye capacities were calculated from Beer Lambert law ($A = \varepsilon lc$), where A is the absorbance intensity of desorption solution, ε is the molar extinction coefficient, l is the optical path length and c is the molar concentration. For desorption solution, we immersed dyed TiO_2 film substrate in a mixture of ethanol and DI water (v/v, 7/3) containing 0.1 M sodium hydroxide for a day in case of N719 or dichloromethane containing 0.1 M trimethylamine for 3 days in case of DAHTDTT. The absorbance spectra of resulting desorption solutions were recorded by UV–vis–NIR spectrophotometer.

Device Performance **Table 4.3** shows the photovoltaic performance for N719- and DAHTDTT-based devices with 1.8-μm and 7-μm active layers, respectively. Both the open circuit voltage (V_{OC}) and photocurrent density (J_{SC}) gradually increased along with GBS time. In the 1.8-μm-thick active layer with DAHTDTT, only 2 min of GBS treatment was sufficient to produce devices with PCE values similar to that from the optimal OS treatment (5 h) and enhanced performance (η = 7.2%, V_{OC} = 0.68 V, J_{SC} = 15.5 mA·cm^{-2}, and fill factor (FF) = 0.69) was achieved after 30 min of GBS. In the 7-μm-thick active layer, only 15 min of GBS was needed to achieve higher PCE values than the best results from OS (7.5 h for DAHTDTT and 15 h for N719). The best performance of N719-based device (η = 8.1%, V_{OC} = 0.72 V, J_{SC} = 15.7 mA·cm^{-2}, and FF = 0.72) was achieved after 30 min of GBS. No improvement in PCE was observed after more than 30 min of GBS.

For further enhancement, we applied the GBS method to a co-sensitization process using both N719 and a porphyrin dye (YD2).[13] Using 30 min as the optimal GBS duration, we treated the 7-μm-thick porous TiO_2 film first with 20 min in N719 and then 10 min in YD2. The cooperation between the dyes led to highly enhanced PCE (η = 9.0%, V_{OC} = 0.72 V, J_{SC} = 16.4 mA·cm^{-2}, and FF = 0.76) in the device, corresponding to ~17% enhancement compared with that after a much longer dual-OS treatment (10 h for N719 and 5 h for YD2). The J-V curves with the best performance are shown in **Figure 4.3**. Moreover, in OS the dye adsorption could be significantly accelerated by using highly concentrated dye solutions (1 mM) according to Eq.4.1. However, the corresponding device performance gradually deteriorated with increasing soaking time (**Table 4.4**), which was attributed to severe dye aggregation.[14] This problem was solved in GBS, demonstrated by time-resolved fluorescence measurement. Detailed explanation is presented with **Figure 4.4** as below.

Table 4.3 Photovoltaic parameters of DSCs according to dyeing conditions.

Dye	*Conc. (mM)*	*Thick. (μm)*	*Method*	*Soaking time*	V_{OC} *(V)*	J_{SC} *(mA cm^{-2})*	*FF (%)*	η^a *(%)*	*Dye capacity* (× 10^{-7} mol cm^{-2})
N719	0.3	1.8	GBS	4 min	0.71	6.8	74.6	3.6	0.26
				8 min	0.71	8.2	74.1	4.3	0.31
				15 min	0.75	9.9	70.2	5.2	0.37
				30 min	0.78	10.1	69.7	5.5	0.44
			OS	12 h	0.77	9.3	73.6	5.3	0.83
		7	GBS	4 min	0.70	7.7	75.7	4.1	0.57
				8 min	0.71	9.8	76.3	5.3	0.81
				15 min	0.72	13.2	74.5	7.1	0.88
				30 min	0.72	15.7	72.2	8.1	0.91
				60 min	0.74	14.6	72.9	7.8	1.02
			OS	15 h	0.72	13.2	73.2	6.9	1.31
N719* + *YD2	0.3 + 0.2	7	GBS	20 + 10 min	0.72	16.4	75.6	9.0	N/A
			OS	10 + 5 h	0.67	15.5	74.1	7.7	N/A
DAHTDTT	0.2	1.8	GBS	2 min	0.65	13.5	70.1	6.2	0.39
				4 min	0.65	13.6	72.1	6.4	0.47
				8 min	0.67	13.9	69.7	6.5	0.57
				15 min	0.67	14.3	69.6	6.7	0.69
				30 min	0.68	15.5	68.6	7.2	0.79
			OS	5 h	0.67	12.9	71.1	6.2	1.24
		7	GBS	2 min	0.66	7.9	73.2	3.8	0.39
				4 min	0.63	10.9	73.9	5.1	0.51
				8 min	0.65	11.6	73.7	5.5	0.89
				15 min	0.66	13.4	73.2	6.4	1.20
				30 min	0.67	13.9	73.4	6.9	1.43
			OS	7.5 h	0.67	13.4	70.6	6.4	2.26

[a] The power conversion efficiency was evaluated as $\eta = (V_{OC} \cdot J_{SC} \cdot FF)/P_{in}$, where P_{in} is the incident light intensity (1000 W·m^{-2}), V_{OC} is the open circuit voltage, J_{SC} is the photocurrent density, and FF is the fill factor. A black mask (0.5 cm × 0.5 cm) was always attached on the DSCs to prevent overestimation. The electrolyte was composed of 0.055M iodine, 0.025M lithium iodide, 0.05M guanidine thiocyanate, 0.6M 1,2-dimethyl-3-propylimidazolium iodide and 0.5M 4-tert-butylpridine in a mixture of acetonitrile and valeronitrile (v/v, 85/15)

Table 4.4 Photovoltaic parameters of DSCs prepared with 1 mM of dye solution.

Dye	*Conc. (mM)*	*Thick. (μm)*	*Method*	*Soaking time*	V_{OC} *(V)*	J_{SC} *(mA cm^{-2})*	*FF (%)*	η^a *(%)*	*Dye capacity (× 10^{-7} mol cm^{-2})*
DAHTDTT	1	1.8	OS	2 min	0.69	12.4	72.4	6.2	0.43
				4 min	0.69	12.4	71.1	6.1	0.49
				8 min	0.69	12.1	70.6	5.9	0.51
				15 min	0.69	11.1	70.3	5.4	0.57
				30 min	0.68	10.9	70.8	5.2	0.63
				60 min	0.67	10.6	71.7	5.1	0.69

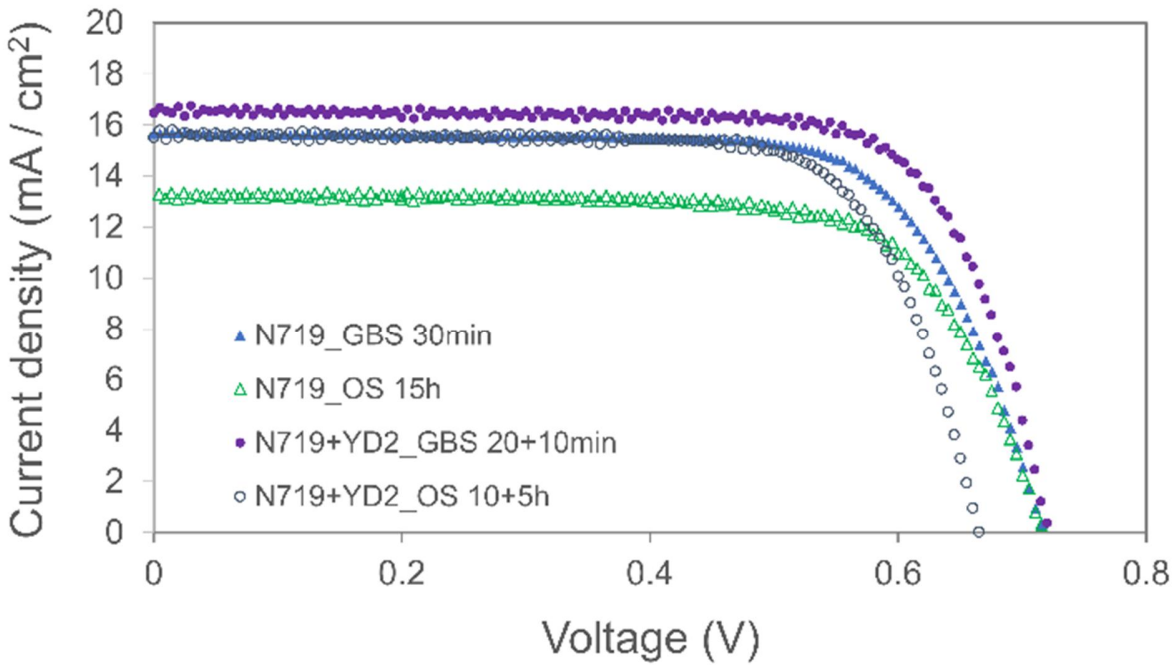

Figure 4.3 Photocurrent density-voltage curves of DSCs with 7-μm-thick active layer based on single (N719) and co-dyes (N719 + YD2), using different dyeing conditions.

Dyeing Method Dependent Dye Aggregation In dyed TiO_2 film, the exciton lifetime in dye monolayer is strongly influenced by the intermolecular distance because charge separation (nonradiative self-quenching) easily occurs between closely neighboring dye molecules. We prepared the dummy cells consisted of dyed zirconium dioxide (ZrO_2) film-coated FTO glass and pure one as the counterpart, which were filled with the inert electrolyte. We compared three dyeing conditions, such as 15 min of GBS (0.2 mM), 90 min of OS (0.2 mM), and 60 min of OS (1 mM), because similar dye capacities were obtained in these conditions (**Table 4.1**). According to dyeing condition, average exciton lifetimes were clearly different, despite the same dye (DAHTDTT). **Figure 4.4** shows fluorescence decay signals and corresponding fitting parameters are summarized in **Table 4.5**. The longest exciton lifetime is provided by GBS_0.2 mM_15 min (224 ps), followed by GBS_0.2 mM_90 min (74 ps) and OS_1 mM_60 min (18 ps). This indicates that the least intermolecular self-quenching occurs after 15 min of GBS (0.2 mM) process. This is attributed to well-balanced dye dispersion in ZrO_2 film, leading to low probability of dye aggregation. These results are well agreeing with other findings as mentioned later.

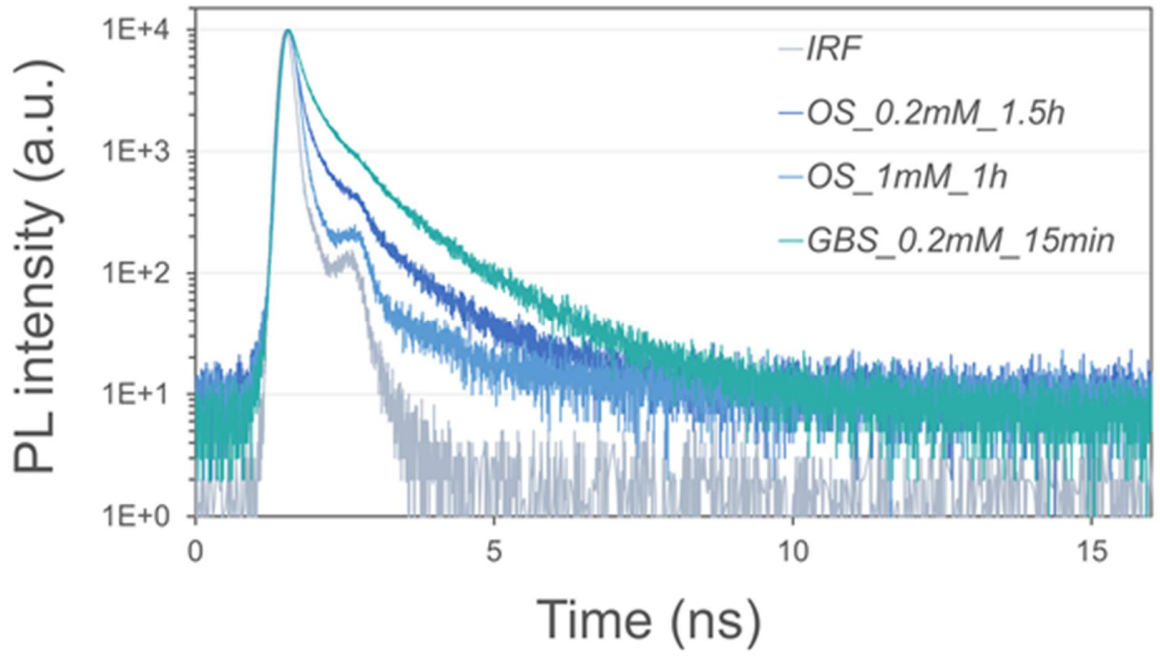

Figure 4.4 Transient PL signals obtained from the dyed ZrO_2 film surrounded by inert electrolytes.

Table 4.5 Fitting Parameters for Estimating Average Exciton Lifetimes from Figure 4.4

	τ_1 (ns)	A_1	τ_2 (ns)	A_2	τ_3 (ns)	A_3	τ_{exc} (ns)
GBS_0.2mM_15min	1287	1.572	29829.6	0.103	8365.6	0.451	0.224
OS_0.2mM_1.5h	993.2	1.165	76542.9	0.044	7898.7	0.233	0.074
OS_1mM_1h	121.7	1.716	218449.7	0.012	19115.3	0.069	0.018

The most noticeable finding here is the inverse correlation between J_{SC} and dye capacity. For N719, the highest J_{SC} was obtained after 30 min of GBS for the 1.8 and 7-μm active layers despite a lower dye capacity. A more extreme difference was observed with DAHTDTT. Although 5 h of OS produced a dye capacity of 1.24×10^{-7} mol cm^{-2} in the 1.8-μm active layer, which is more than three times that after 2 min of GBS (0.39×10^{-7} mol cm^{-2}), the device fabricated using GBS exhibited higher J_{SC} values. Therefore, the enhanced performance cannot be explained in terms of increased dye capacity. Instead, we propose the following mechanism for GBS. Gas flow generates a physical driving force through the porous TiO_2 film, pushing the dye molecules to the bottom of the film and accelerates the dye infiltration. The result is dispersed dye molecules deep inside the porous TiO_2 film, which increases the surface coverage of dye. The high dye coverage reduces charge recombination, owing to decreased contact area between the TiO_2 particles and the electrolyte. This hypothesis is supported by the experimental results as discussed below.

Plasmon Sensor Study of Dye Infiltration We first fabricated plasmon sensors as shown in **Figure 4.5**, consisting of ca. 20-μm-thick porous TiO_2 film and Au nanoparticle-coated fluorine-doped tin oxide (FTO) substrate (see Experimental Section for details).[15] In **Figure 4.5e**, energy-dispersive X-ray spectroscopy (EDX) data confirmed the existence of Au nanoparticles at the interface between FTO and TiO_2 film. The nanoparticles exhibited intrinsic absorbance peak near 650 nm due to their localized surface plasmon resonance (LSPR). According to previous studies, the plasmon oscillational frequency (energy) is proportional to the free electron density at the surface of each metallic nanoparticle.[16-17]

In our case, a gradual blue-shift and proportionally growing amplitude in the LSPR peak were observed with increasing soaking time, indicative of increased oscillational electron density near the Au nanoparticles.[18] This was attributed to the photoelectron injection from the anchored dye molecules: if dye molecules could pass through the porous TiO_2 film during soaking to reach the oscillational range of Au nanoparticles at the bottom of the film, they would supply additional photoelectrons under electromagnetic radiation to further activate the LSPR.[19] Therefore, we used the blue-shift of LSPR peak after dyeing to investigate the amount and speed of dye infiltration into the porous TiO_2 film. **Figure 4.6** shows the absorbance spectra from the plasmon sensors before and after treating with 0.08 mM N719, and the overall results are summarized in **Figure 4.5**f. Remarkable blue-shift (from 652 to 647 nm) appeared in the LSPR peak after only 8 min of GBS and became quickly saturated after 15 min with 8 nm of blue-shift. In contrast, even after 30 min of OS the blue-shift was slight (from 649 to 647 nm) and saturated in 1 h with a maximum shift of 6 nm. These results all imply that GBS permits better dye infiltration across the porous TiO_2 film than OS.

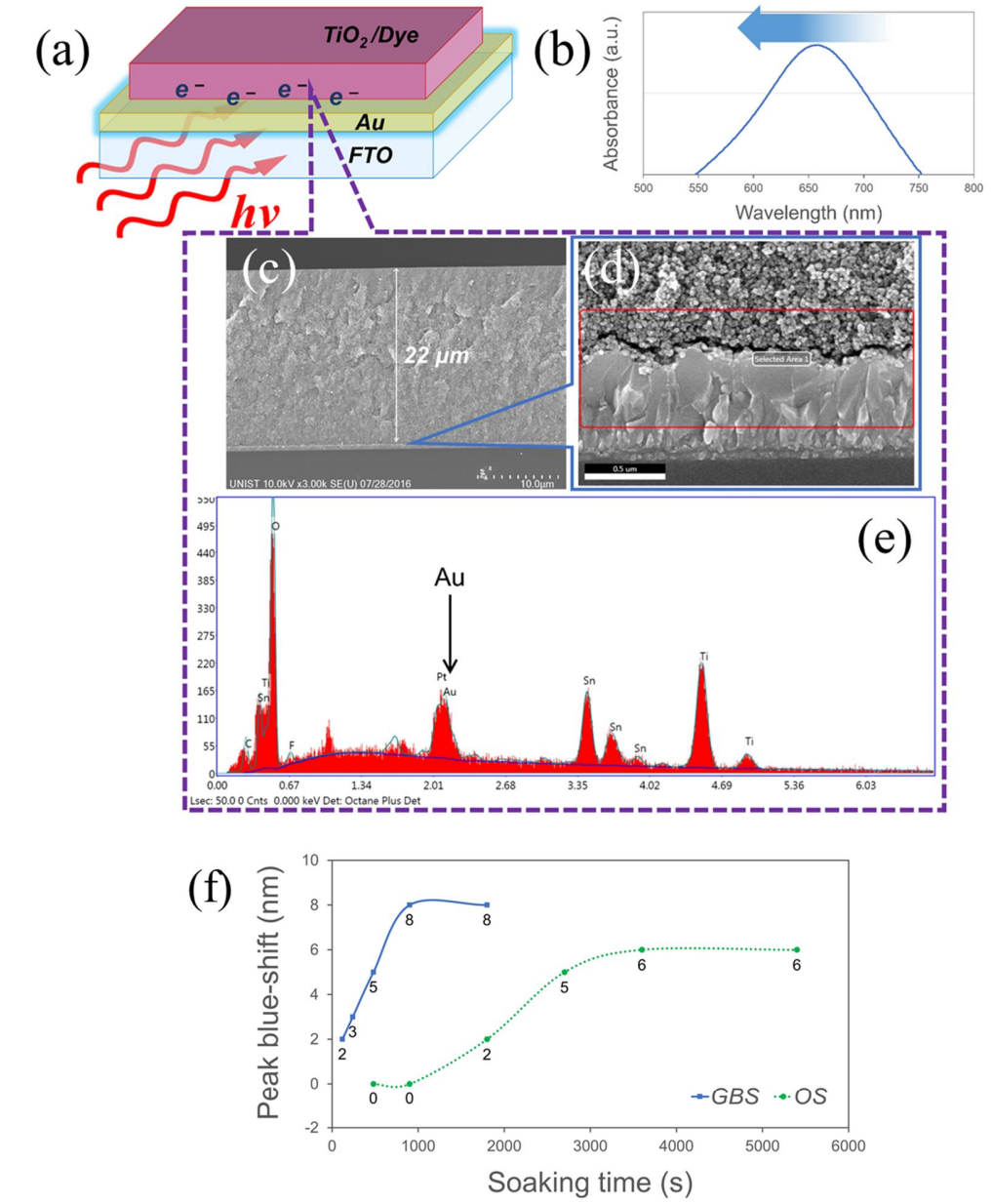

Figure 4.5 (a) Schematic representation of plasmon sensor consisted of FTO layer, Au nanoparticle layer, and dyed porous TiO_2 layer: (b) In plasmon sensor, dyes supply photoelectrons under electromagnetic radiation so that intrinsic LSPR peak is blue-shifted. (c) Cross section SEM image of plasmon sensor. (d) Enlargement of interface between FTO and porous TiO_2 layer. (e) EDX result in the selected area (red rectangle in Figure 3d), indicating the existence of Au. (f) LSPR peak blue-shift according to GBS and OS soaking time. Note that GBS gives much faster initiation, saturation, and higher maximum values of peak blue-shift than OS. TOF-SIMS depth profiles of N719-sensitized TiO_2 films according to dyeing condition: (g) 15 min of GBS and (h) 1 h of OS. Note the difference in Ru^+ signals (Purple square) between them.

Dye Distribution from TOF-SIMS Analysis TOF-SIMS was employed to directly map the density of dye molecules, by presenting the depth-dependent signal intensities of cations extracted at different depths in the porous TiO_2 film.[20] The samples were prepared with ~7-μm porous TiO_2 film on FTO glass, dyed in 0.08 mM N719 solution using either 15 min of GBS (**Figure 4.5g**) or 1 h of OS (**Figure 4.5h**).

Strong Ti^+ signal appeared on the top of the porous TiO_2 film, with weak Si^+ signal corresponding to a trace amount of SiO_2 impurity. The Ru^+ signals was simultaneously detected in both samples, corresponding to the N719 molecules. However, in the sample treated with OS, the Ru^+ signal rapidly decayed with depth, while in that treated with GBS the decay continued to a depth of ~7-μm. When the signal of Ru^+ decayed completely, those of Sn^+ and Si^+ dramatically increased, indicating the exposure of the FTO glass. These findings clearly suggest that GBS creates a more even dye distribution inside the porous TiO_2 film, which is in good agreement with the findings from the LSPR study and strongly supports our hypothesis.

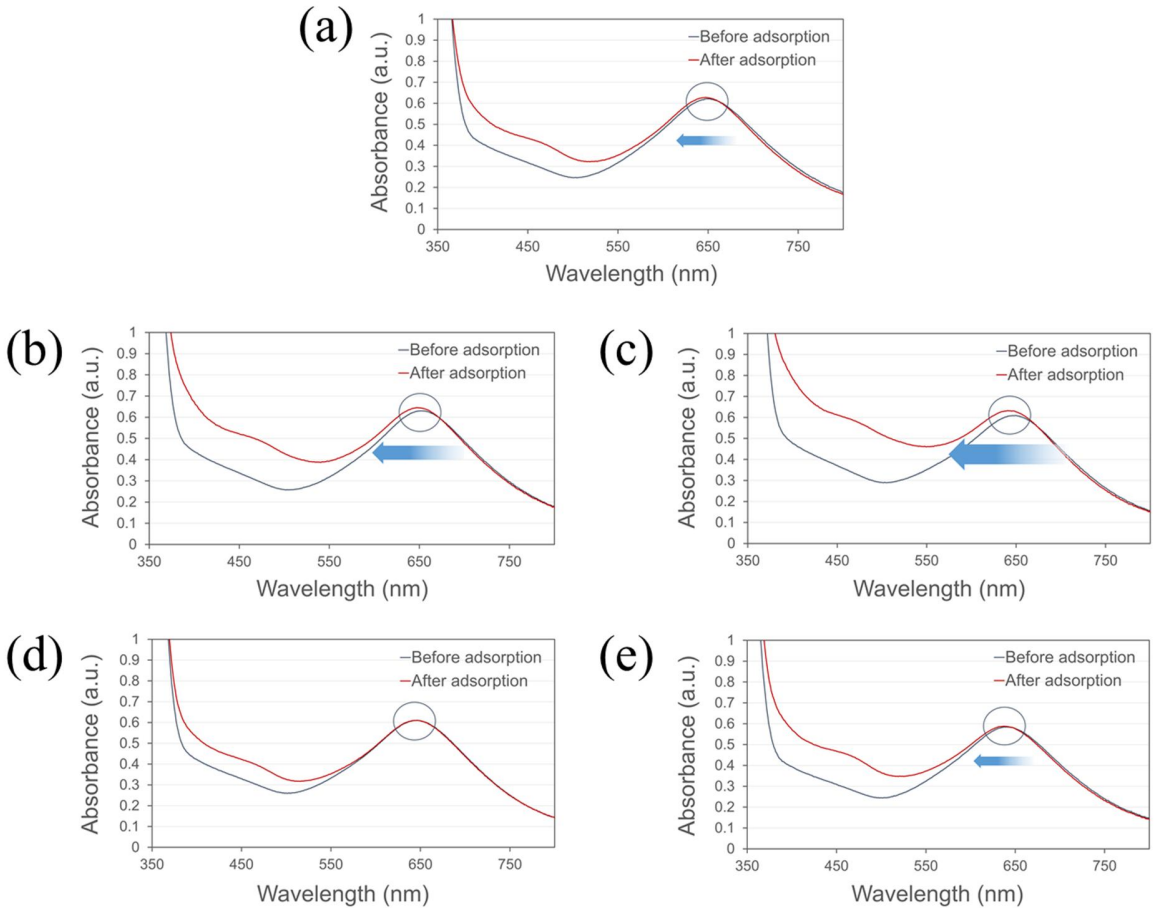

Figure 4.6. The evolutions of absorbance peak of plasmon sensors after dyeing, presented according to dyeing condition, such as (a) 2 min of GBS, (b) 8 min of GBS, (c) 15 min of GBS, (d) 15 min of OS, and (e) 30 min of OS. Note the same peak blue-shift (2 nm) between 2 min of GBS and 30 min of OS, indicative of much faster dye infiltration when using GBS.

The Influence of Dye Distribution on Charge Transport Uneven distribution of dye molecules in the active layer causes many dye-free sites, which retard the charge transport in the DSCs.[21] **Figure 4.7a** schematically shows that the charge transport is slower across a longer series of dye-free sites (left, uneven dye distribution) and vice versa. We investigated the transport of photoinjected electrons in a 7-μm-thick active layer, using controlled intensity modulated photo spectroscopy (CIMPS).

The charge transport time (τ_d) and the minimum angular frequency (f_{min}) in CIMPS response are related by $\tau_d = 1/\omega_{min} = 1/2\pi f_{min}$.[22] **Figure 4.7b** shows the estimated τ_d as a function of the incident photon flux (λ = 503 nm). As expected, charge transport in the active layer becomes faster with longer GBS treatment. A GBS duration of only 15 min is sufficient to produce a shorter τ_d value than that after 15 h of OS. The shortest τ_d was recorded in DSCs fabricated using 30 min of GBS. Another simple comparison criterion is the frequency-dependent photocurrent efficiency, namely the ratio of imaginary part of photocurrent response to the light intensity (130 W m^{-2}), which is presented in **Figure 4.7c** as a function of the sinusoidal frequency superimposed on the DC bias of the light source.[23] The peak frequency gradually increases with increasing GBS time, implying a trend of decreasing dye-free sites as the sample is treated.

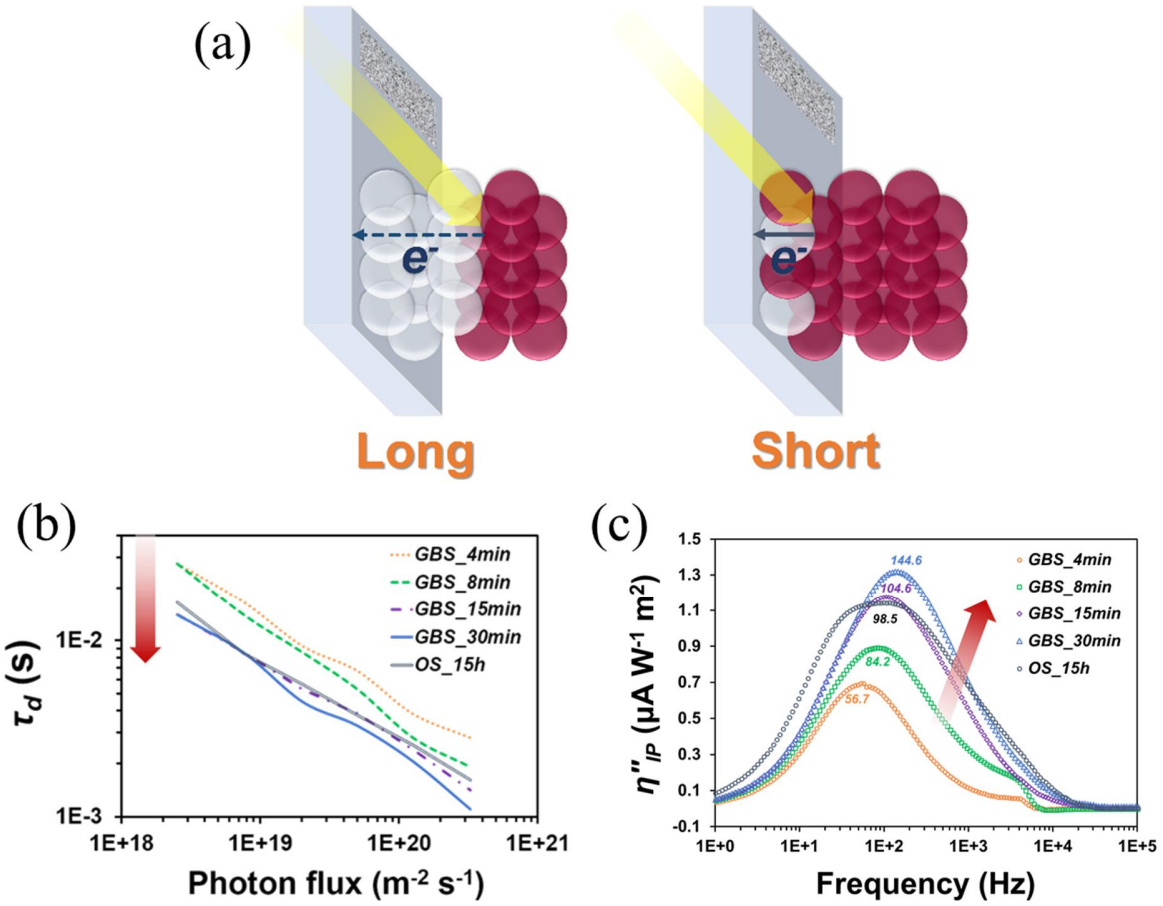

Figure 4.7 (a) Difference in charge collection kinetics according to the dye distribution, slow (left) and fast (right) charge transport with long and short dye-free sites, respectively. (b) Charge transport times from N719-based DSCs using a 7-μm-thick active layer as a function of incident photon flux (503 nm, 130 W m^{-2}) and (c) corresponding imaginary component of photocurrent response depending on the modulation frequency applied on the light source bias. Faster charge transport with increasing GBS time indicates more occupied dye-free sites.

Impedance Analysis of Dye Surface Coverage Ultimately, the dye distribution inside the active layer affects charge transport as well as the dye coverage on the surface of TiO_2 nanoparticles, which is associated with the recombination rate between photoinjected electrons and oxidized redox mediators. Electrochemical impedance spectroscopy (EIS) analysis was performed under one sun condition, in order to study the dye surface coverage in terms of charge transfer resistance (R_{CT}) and chemical capacitance (C_μ). The resultant Nyquist plots and fitting parameters are presented in **Figure 4.8a** and **Table 4.6**, respectively.

The value of R_{CT} in the porous TiO_2 film, as the emerging semicircle form at intermediate frequency regime, gradually decreases with increasing GBS time. A minimum R_{CT} value of 12.52 Ω was recorded in the DSC using 30 min of GBS, while that using 15 h of OS was 13.21 Ω. We highlight a correlation between the dye capacity and C_μ, which represents the charge accumulation in the TiO_2 phase.[24-25] Considering the condition of one sun illumination, C_μ should be proportional to the amount of anchored dye molecules. However, the contrary trend was observed: 30 min of GBS produced the highest C_μ value, even though the corresponding dye capacity was less than that after 15 h of OS.

This extraordinary situation can be explained in terms of the charge recombination time ($\tau_{rec} = 1/\omega_{min} = 1/2\pi f_{min}$), estimated from the inverse of minimum angular frequency in Nyquist plots. The trend of τ_{rec} is in accordance with that of C_μ, meaning that longer τ_{rec} (low charge loss) is the decisive factor to achieve high C_μ. The resident dye molecules deep inside the TiO_2 film are expected to reduce the exposure of TiO_2 particles to the electrolyte, thereby reducing the back reaction between the photoinjected electrons and oxidized redox mediators. Therefore, it is a key factor for improved device performance, in conjunction with fast charge collection.

Table 4.6 Fitting Parameters from Nyquist Plots and Extracted Charge

	R_S (Ω)	R_{dl} (Ω)	R_{CT} (Ω)	C_μ (μF)	τ_{rec} (ms)	Q_{ext} [a] *delay 0s* ($\mu C\ cm^{-2}$)	Q_{ext} [a] *delay 5s* ($\mu C\ cm^{-2}$)	*Dye capacity* ($\times 10^{-7}$ mol cm^{-2})
GBS_4min	6.29	9.69	20.84	178.11	2.52	28.81	6.63	0.57
GBS_8min	6.44	6.12	18.43	285.13	3.18	26.30	6.29	0.81
GBS_15min	7.15	5.58	16.75	394.85	3.56	32.68	9.39	0.88
GBS_30min	6.83	5.92	12.52	472.91	4.49	39.01	17.08	0.91
OS_15h	7.43	5.71	13.21	361.62	3.56	50.01	11.78	1.31

[a] Charge extraction was performed in shielded black box using monochromatic light source (λ_{max} = 503 nm, 100 W m^{-2}). Discharging current was fixed at 10 μA.

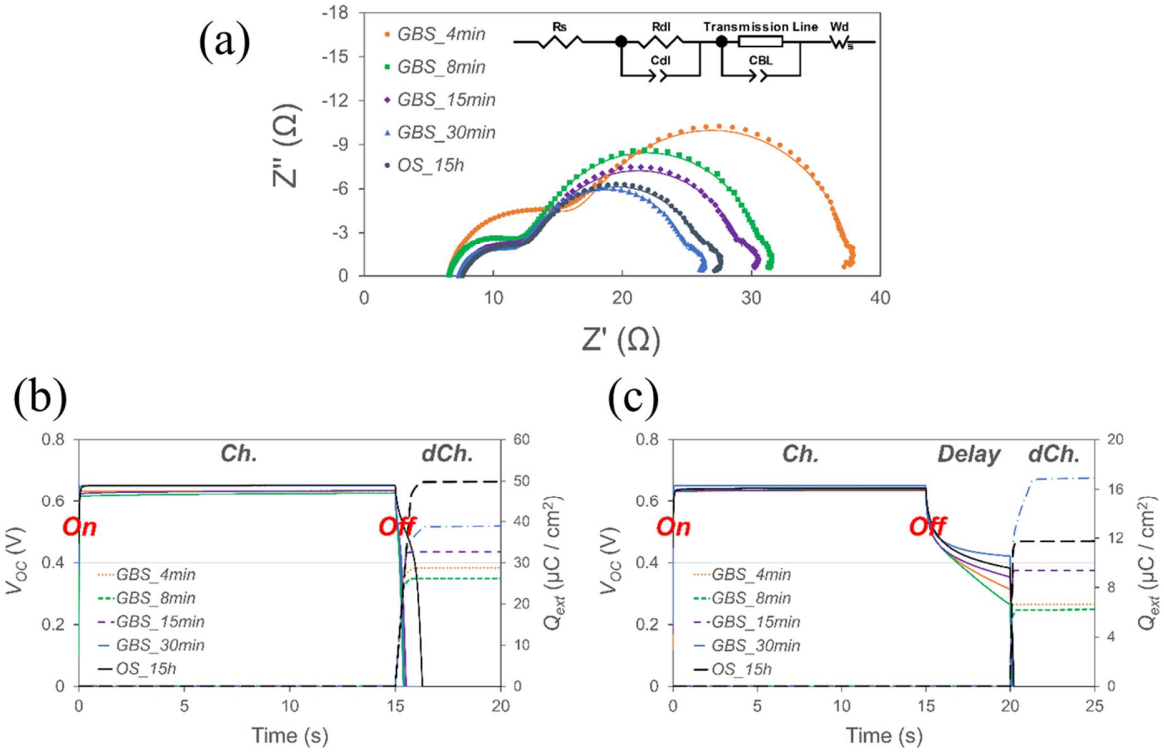

Figure 4.8 (a) Nyquist plots from N719-based DSCs using 7-μm-thick active layer according to dyeing condition. Inset is the equivalent circuit used for fitting. EIS was conducted at one sun illumination, applying a 10 mV AC modulation overlapped in DC forward bias ($-V_{OC}$) with the frequency ranging from 10^{6} to 10^{-1} Hz. Charge extraction process of (b) without delay and (c) with delay represented by V_{OC} (solid line) and Q_{ext} (dashed line) as a function of progress time. Note the differences in Q_{ext} between 30 min of GBS and 15 h of OS before and after delay.

Correlation between Dye-Free Sites and Charge Loss To further understand the dye surface coverage, we compared the charge loss in the active layer under dark condition, using the charge extraction method proposed by Duffy et al.[26] The active layer in DSCs can be described as a reservoir in which photoinjected electrons are stored, and the dye-free sites in it are drains through which these electrons recombine with the oxidized redox mediators. Firstly, the DSCs are illuminated at open circuit state for sufficient time to reach charge equilibrium. After 15 s, the light is switched off and the devices are synchronously converted into short-circuit state to measure the extracted charge (Q_{ext}), which together with V_{OC}, is presented as functions of time in **Figure 4.8b**, c. In both cases, V_{OC} reaches an equilibrium value in a few seconds after the light is turned on, while Q_{ext} stays at zero (charging). In **Figure 4.8c**, as soon as the light is off, arising vertical dashed lines indicate the conversion into short circuit state (discharging), which also reaches equilibrium in a few seconds. As expected, Q_{ext} is proportional to the dye capacity. The Q_{ext} value after 15 h of OS (50.01 μC cm^{-2}) is higher than that of 30 min of GBS (39.01 μC cm^{-2}).

For comparison, we left the devices in the dark for 5 s before converting into short circuit state to allow charge loss through the dye-free sites. In **Figure 4.8c**, the attenuating V_{OC} between 15–20 s indicates the charge loss in the dark at open circuit state (delay). After the 5-second delay, there is the inverted order of Q_{ext} between 15 h of OS (11.78 μC cm^{-2}) and 30 min of GBS (17.08 μC cm^{-2}). This is quite different from the case without delay (**Figure 4.8b**) and clearly indicates that much more charge is lost in DSCs fabricated with OS than those with GBS, because of the many more dye-free sites in the former. These results are in good agreement with those from impedance analysis.

4.3 Conclusion

In summary, up to now there has been no report on controlling the dye distribution in mesoporous TiO_2 film, although it is a very important factor in the performance of DSCs. For this purpose, we developed a sustainable and efficient dye arrangement method, gas bubbling soaking (GBS). Compared to the conventional method of overnight soaking (OS), GBS facilitates even dye distribution within the porous TiO_2 film, resulting in enhanced PCEs and significantly shortened DSC fabrication time. We achieved ~17% higher PCE (η = 9.0% with V_{OC} = 0.72 V, J_{SC} = 16.4 mA·cm^{-2}, and FF = 0.76) using dual-GBS than that using optimal duration of dual-OS with 7-μm-thick active layer. The physical driving force generated by gas flow during the GBS process is responsible for such improvements. The flowing gas carries dye molecules to the bottom of the active layer with it, while during OS most dye molecules stay near the top of the active layer. This finding was confirmed by plasmon sensor study and TOF-SIMS depth profiles. The well-balanced dye dispersion in the active layer created by GBS leads to extensive dye coverage on the TiO_2 surface and fewer dye-free sites. The resulting fast charge transport and decreased charge loss in the active layer improved the PCE in the device. This interpretation was explicitly confirmed by thorough experimental methods. This study suggests that GBS is a promising method for industrial production of DSCs, due to its sustainability, low-cost, and scalability.

4.4 Experimental Section

Dyeing Methods For the gas bubbling soaking (GBS) process, the prepared porous TiO_2 film substrate was placed face-up in a vessel whose opening was blocked except for some vents to avoid vessel damage due to excessive pressure. The vessel was filled with the dye solution. Then gas was injected into the vessel through a needle, followed by emission through vents. As shown in **Figure 4.9**, we tried a different size of vessel according to the object size. The gas injection pressure was controlled depending on the in-vessel volume and the number of gas injection entrance, ranging from 1 psi (left side in **Figure 4.9**) to 5 psi (right side in **Figure 4.9**). We used mainly N_2 gas for the GBS process, but CO_2 and air were also used for comparison. Considering the continuous vaporization of volatile solvent, we regularly added solvent so that the concentration of dye solution hardly changed during the soaking. In the conventional overnight soaking (OS) process, the same substrate was immersed in the dye solution at room temperature under dark condition for the desired duration.

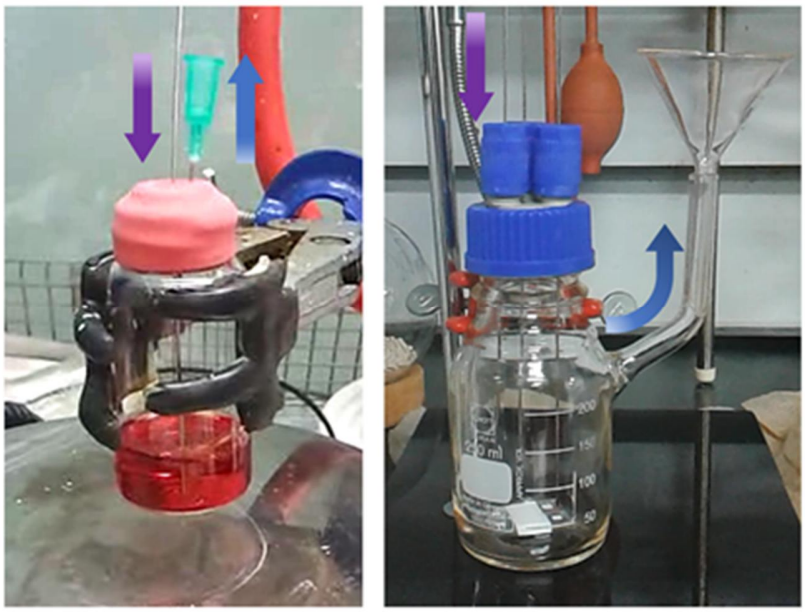

Figure 4.9 The photographs of experimental apparatus for GBS process. The size of vessel can be controlled depending on the object size. Considering the in-vessel volume and the number of gas injection entrance (purple arrow), the gas injection pressure is controlled from 1 psi (left side) to 5 psi (right side). Some vents (blue arrow) are needed for avoiding vessel damage due to excessive pressure.

Plasmon Sensor Fabrication Plasmon sensors were fabricated in the following four steps. Firstly, a 10-nm Au layer was coated onto the cleaned FTO glass using a thermal evaporator at the rate of 1×10^{-1} nm s^{-1}. Then the Au-coated FTO glass was heated at 500 °C for 3.5 h under argon flow, so that Au nanoparticles (with an average diameter of 40 nm) evolved from the amorphous Au layer.[27] Thirdly, a 10-nm-thick, dense TiO_2 layer was added on top of the Au layer, using atomic layer deposition (ALD, Lucida D100, NCD CO., LTD.), acting as an oscillational energy amplifier as well as a shield of Au nanoparticles against the external environment. Lastly, a mesoporous TiO_2 layer (~20 μm) was formed by screen-printing commercial TiO_2 paste and then sintering at 500 °C for 30 min. The absorption spectra of plasmon sensors before and after dyeing were recorded by the R928 photomultiplier tube of a UV-vis-NIR spectrophotometer (Cary 5000, Agilent Technologies, Inc.), with a connected diffuse reflectance accessory (DRA2500) for exact measurement. The morphological images and element data of the specimens were obtained from a cold field emission-scanning electron microscope (FE-SEM, SU-8220, Hitachi). The X-ray diffraction (XRD) analysis was conducted with a D8 ADVANCE system, with DAVINCI (Bruker AXS) diffractometer using Cu Kα radiation operated at 40 kV and 40 mA, for identifying the crystallinity of each specimen.

Plasmon Sensor Characterization **Figures 4.10a–4.10d** shows the photographs of corresponding fabrication step. Their intrinsic color transition results from the change in absorption property as shown **Figures 4.11a–4.11d**. The optical property in plasmon sensor originates from the interactions between incident light and surface electrons on gold (Au) film or nanoparticles.[28] At first step, no apparent peak, weak absorbance through wide range of wavelength corresponds to electromagnetic field propagation along the surface of Au layer. The appearance of small peak at second step implies the evolution of Au nanoparticles from amorphous layer, clearly proved in SEM images (**Figure 4.12a** and **4.12b**) and XRD patterns (**Figure 4.12c**). They look like rocky islands of average 40 nm diameter. In XRD patterns, their diffraction peaks at second step are too small to detect because thermally deposited Au layer is too thin (< 10 nm). Nevertheless, all peaks well match the (111), (200), and (220) Bragg reflections (2θ = 38.178°, 44.374°, and 64.559°) corresponding to JCPDS card (NO. 4-784).[29] The most critical change occurs at third step. ALD-deposited dense TiO_2 film (10 nm of thickness) covering Au nanoparticles acts as plasmon oscillational energy amplifier as well as shield against the surrounding environment, as evidenced by rapidly increased intensity of absorbance peak. Additionally, absorbance peak largely red-shifts from 556 nm to 648 nm, indicating higher refractive index near Au nanoparticles after deposition of dense TiO_2 layer. Lastly, screen-printed mesoporous TiO_2 film has a negligible impact on the position and intensity of absorbance peak.

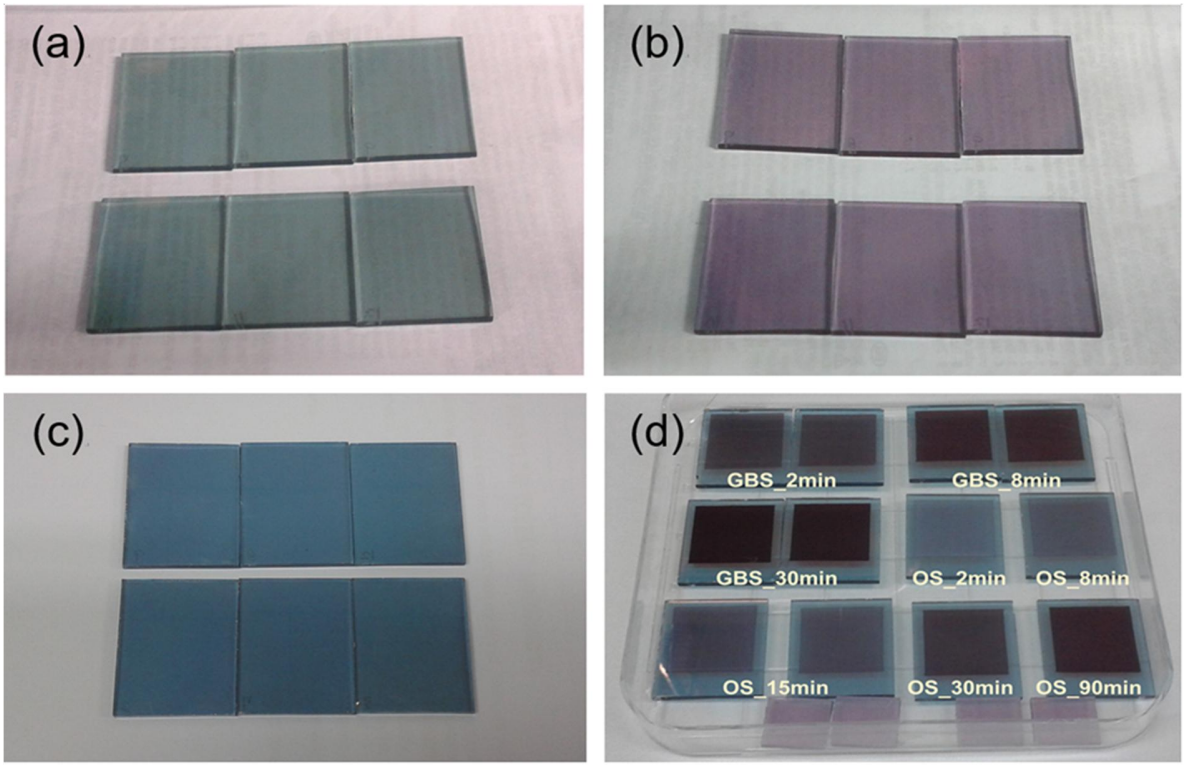

Figure 4.10 The photographs of plasmon sensors at each fabrication step, (a) first, (b) second, (c) third, and (d) forth step. Figure S5d shows all plasmon sensors after dyeing at various conditions using 0.08 mM N719 solution.

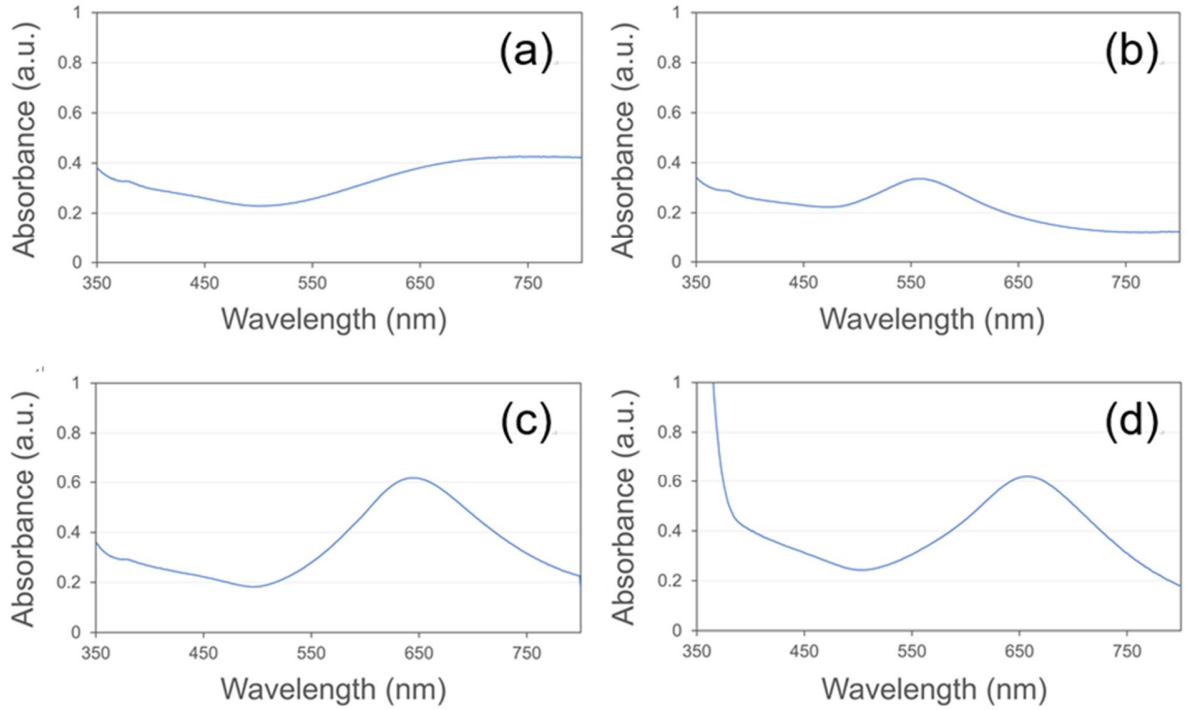

Figure 4.11 Absorbance spectra from plasmon sensors at each fabrication step, (a) first, (b) second, (c) third, and (d) forth step. Note the rapidly amplified intensity and large red-shift of absorbance peak from second to third step.

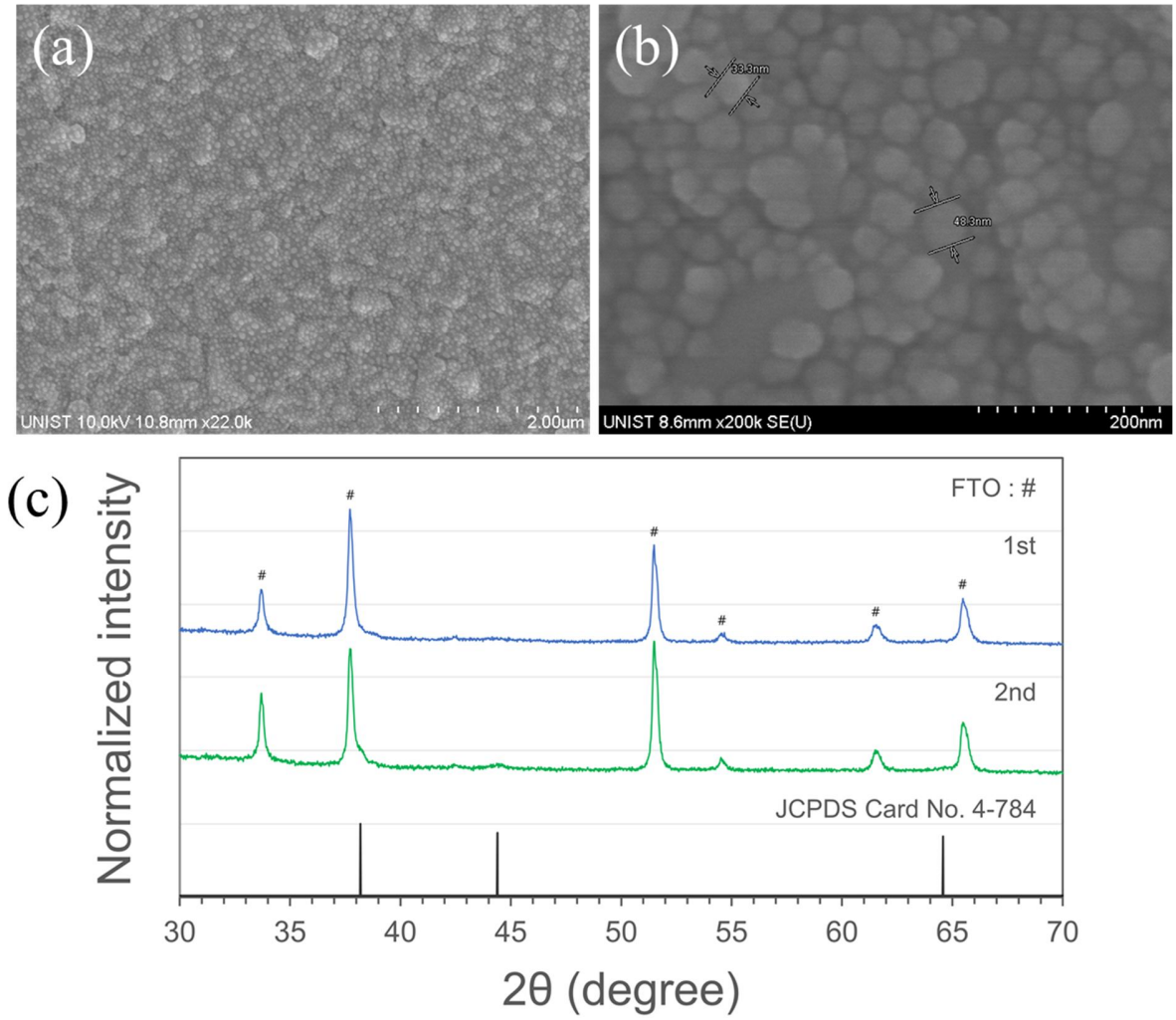

Figure 4.12 The plane SEM images in (a) low and (b) high magnification and (c) XRD patterns of plasmon sensor at second step. We identify the uniformly distributed rocklike Au nanoparticles of average 40 nm diameter. Refer to peak position of Au particles in JCPDS card (NO. 4-784) for easier comparison.

Time-of-flight Secondary Ion Mass Spectrometry The dye density as a function of depth in the porous TiO_2 film was acquired using TOF-SIMS (TOF.SIMS 5, ION-TOF GmbH) with a high maximum mass range (> 9000 u). The spectra were recorded in the positive ion mode at high mass resolution ($m/\Delta m$, > 10000 for Bi^+). Depth profiling was carried out in the dual beam mode at a repetition rate of up to 50 kHz. In this interlaced mode, the first ion beam (O_2, 2 keV) was used to bombard the desired area, and the second ion beam (Bi_1, 25 keV) was used to progressively analyze the bottom of the crater. The analytical beam was incident on a small area in the crater (25 × 25 μm^2) to avoid the crater edge effect.[30] Perfect charge compensation was applied to the insulating TiO_2 film, due to the very efficient electron flood gun (20 eV). The mass calibration was carried out based on unsaturated hydrocarbon species (CH_2^+, CH_3^+, $C_2H_2^+$, $C_2H_3^+$, and $C_7H_7^+$).

REFERENCE

1. Hagfeldt, A.; Boschloo, G.; Sun, L. C.; Kloo, L.; Pettersson, H., Dye-Sensitized Solar Cells. *Chem. Rev.* **2010,** *110* (11), 6595-6663.

2. Nasiri, A.; Zabalawi, S. A.; Mandic, G., Indoor Power Harvesting Using Photovoltaic Cells for Low-Power Applications. *IEEE Trans. Ind. Electron.* **2009,** *56* (11), 4502-4509.

3. Weerasinghe, H. C.; Sirimanne, P. M.; Simon, G. P.; Cheng, Y. B., Cold isostatic pressing technique for producing highly efficient flexible dye-sensitised solar cells on plastic substrates. *Prog. Photovoltaics* **2012,** *20* (3), 321-332.

4. Lee, H.; Hwang, D.; Jo, S. M.; Kim, D.; Seo, Y.; Kim, D. Y., Low-Temperature Fabrication of TiO2 Electrodes for Flexible Dye-Sensitized Solar Cells Using an Electrospray Process. *ACS Appl. Mater. Inter.* **2012,** *4* (6), 3308-3315.

5. Han, H. G.; Weerasinghe, H. C.; Min Kim, K.; Soo Kim, J.; Cheng, Y. B.; Jones, D. J.; Holmes, A. B.; Kwon, T. H., Ultrafast Fabrication of Flexible Dye-Sensitized Solar Cells by Ultrasonic Spray-Coating Technology. *Sci. Rep.* **2015,** *5*, 14645.

6. O'Regan, B.; Li, X. E.; Ghaddar, T., Dye adsorption, desorption, and distribution in mesoporous TiO2 films, and its effects on recombination losses in dye sensitized solar cells. *Energ Environ. Sci.* **2012,** *5* (5), 7203-7215.

7. Holliman, P. J.; Davies, M. L.; Connell, A.; Velasco, B. V.; Watson, T. M., Ultra-fast dye sensitisation and co-sensitisation for dye sensitized solar cells. *Chem. Commun.* **2010,** *46* (38), 7256-7258.

8. Kim, B.; Park, S. W.; Kim, J. Y.; Yoo, K.; Lee, J. A.; Lee, M. W.; Lee, D. K.; Kim, J. Y.; Kim, B.; Kim, H.; Han, S.; Son, H. J.; Ko, M. J., Rapid Dye Adsorption via Surface Modification of TiO2 Photoanodes for Dye-Sensitized Solar Cells. *ACS Appl. Mater. Inter.* **2013,** *5* (11), 5201-5207.

9. Ogomi, Y.; Sakaguchi, S.; Kado, T.; Kono, M.; Yamaguchi, Y.; Hayase, S., Ru dye uptake under pressurized CO2 improvement of photovoltaic performances for dye-sensitized solar cells. *J. Electrochem. Soc.* **2006,** *153* (12), A2294-A2297.

10. Masel, R. I., *Principles of adsorption and reaction on solid surfaces*. Wiley: New York, 1996; p xiv, 804 p.

11. Nazeeruddin, M. K.; Kay, A.; Rodicio, I.; Humphrybaker, R.; Muller, E.; Liska, P.; Vlachopoulos, N.; Gratzel, M., Conversion of Light to Electricity by Cis-X2bis(2,2'-Bipyridyl-4,4'-Dicarboxylate)Ruthenium(Ii) Charge-Transfer Sensitizers (X = Cl-, Br-, I-, Cn-, and Scn-) on Nanocrystalline Tio2 Electrodes. *J. Am. Chem. Soc.* **1993,** *115* (14), 6382-6390.

12. Kwon, T. H.; Armel, V.; Nattestad, A.; MacFarlane, D. R.; Bach, U.; Lind, S. J.; Gordon, K. C.; Tang, W. H.; Jones, D. J.; Holmes, A. B., Dithienothiophene (DTT)-Based Dyes for Dye-Sensitized Solar Cells: Synthesis of 2,6-Dibromo-DTT. *J. Org. Chem.* **2011,** *76* (10), 4088-4093.

13. Barea, E. M.; Gonzalez-Pedro, V.; Ripolles-Sanchis, T.; Wu, H. P.; Li, L. L.; Yeh, C. Y.; Diau, E. W. G.; Bisquert, J., Porphyrin Dyes with High Injection and Low Recombination for Highly Efficient Mesoscopic Dye-Sensitized Solar Cells. *J. Phys. Chem. C* **2011,** *115* (21), 10898-10902.

14. Cappel, U. B.; Moia, D.; Bruno, A.; Vaissier, V.; Haque, S. A.; Barnes, P. R. F., Evidence for photo-induced charge separation between dye molecules adsorbed to aluminium oxide surfaces. *Sci. Rep.* **2016,** *6*.

15. Gusak, V.; Heiniger, L. P.; Graetzel, M.; Langhammer, C.; Kasemo, B., Time-Resolved Indirect Nanoplasmonic Sensing Spectroscopy of Dye Molecule Interactions with Dense and Mesoporous TiO2 Films. *Nano Lett.* **2012,** *12* (5), 2397-2403.

16. Prodan, E.; Nordlander, P., Plasmon hybridization in spherical nanoparticles. *J. Chem. Phys.* **2004,** *120* (11), 5444-5454.

17. Rogers, P. H.; Sirinakis, G.; Carpenter, M. A., Direct observations of electrochemical reactions within Au-YSZ thin films via absorption shifts in the an nanoparticle surface plasmon resonance. *J. Phys. Chem. C* **2008,** *112* (17), 6749-6757.

18. Karker, N.; Dharmalingam, G.; Carpenter, M. A., Thermal Energy Harvesting Plasmonic Based Chemical Sensors. *ACS Nano* **2014,** *8* (10), 10953-10962.

19. Willets, K. A.; Van Duyne, R. P., Localized surface plasmon resonance spectroscopy and sensing. *Annu. Rev. Phys. Chem.* **2007,** *58*, 267-297.

20. Stepien, M.; Saarinen, J. J.; Teisala, H.; Tuominen, M.; Aromaa, M.; Haapanen, J.; Kuusipalo, J.; Makela, J. M.; Toivakka, M., ToF-SIMS Analysis of UV-Switchable TiO2-Nanoparticle-Coated Paper Surface. *Langmuir* **2013,** *29* (11), 3780-3790.

21. Franco, G.; Peter, L. M.; Ponomarev, E. A., Detection of inhomogeneous dye distribution in dye sensitised nanocrystalline solar cells by intensity modulated photocurrent spectroscopy (IMPS). *Electrochem. Commun.* **1999,** *1* (2), 61-64.

22. Guillen, E.; Ramos, F. J.; Anta, J. A.; Ahmad, S., Elucidating Transport-Recombination Mechanisms in Perovskite Solar Cells by Small-Perturbation Techniques. *J. Phys. Chem. C* **2014,** *118* (40), 22913-22922.

23. Kruger, J.; Plass, R.; Gratzel, M.; Cameron, P. J.; Peter, L. M., Charge transport and back reaction in solid-state dye-sensitized solar cells: A study using intensity-modulated photovoltage and photocurrent spectroscopy. *J. Phys. Chem. B* **2003,** *107* (31), 7536-7539.

24. Bisquert, J.; Vikhrenko, V. S., Interpretation of the time constants measured by kinetic techniques in nanostructured semiconductor electrodes and dye-sensitized solar cells. *J. Phys. Chem. B* **2004,** *108* (7), 2313-2322.

25. Wang, Q.; Ito, S.; Gratzel, M.; Fabregat-Santiago, F.; Mora-Sero, I.; Bisquert, J.; Bessho, T.; Imai, H., Characteristics of high efficiency dye-sensitized solar cells. *J. Phys. Chem. B* **2006,** *110* (50), 25210-25221.

26. Duffy, N. W.; Peter, L. M.; Rajapakse, R. M. G.; Wijayantha, K. G. U., A novel charge extraction method for the study of electron transport and interfacial transfer in dye sensitised nanocrystalline solar cells. *Electrochem. Commun.* **2000,** *2* (9), 658-662.

27. Meriaudeau, F.; Wig, A.; Passian, A.; Downey, T.; Buncick, M.; Ferrell, T. L., Gold island fiber optic sensor for refractive index sensing. *Sens. Actuator B-Chem.* **2000,** *69* (1-2), 51-57.

28. Van Duyne, R. P., Molecular plasmonics. *Science* **2004,** *306* (5698), 985-986.

29. Mukherjee, P.; Ahmad, A.; Mandal, D.; Senapati, S.; Sainkar, S. R.; Khan, M. I.; Ramani, R.; Parischa, R.; Ajayakumar, P. V.; Alam, M.; Sastry, M.; Kumar, R., Bioreduction of AuCl4- ions by the fungus, Verticillium sp. and surface trapping of the gold nanoparticles formed. *Angew. Chem.-Int. Edit.* **2001,** *40* (19), 3585-3588.

30. Tellez, H.; Aguadero, A.; Druce, J.; Burriel, M.; Fearn, S.; Ishihara, T.; McPhail, D. S.; Kilner, J. A., New perspectives in the surface analysis of energy materials by combined time-of-flight secondary ion mass spectrometry (ToF-SIMS) and high sensitivity low-energy ion scattering (HS-LEIS). *J. Anal. At. Spectrom.* **2014,** *29* (8), 1361-1370.

Chapter 5. Light Intensity Dependent Photo-energy Conversion/Storage Efficiency of Dye-sensitized Solar Battery (DSSB)

5.1 Introduction

Over the past decades, there have been many projects on the future depletion of the natural resources and the increasing green-house effect, trying to develop various renewable energy technologies.[1-3] In addition to that, the effective power management allows us to save a huge amount of surplus energy. Especially, power consumption in buildings runs to nearly 40% of the whole power consumption. In this reason, building energy management system industries are growing rapidly so that indoor environment-customized ubiquitous power supplies are increasingly required.[4-6] With indoor lighting as an open and inexpensive power source, photo-rechargeable batteries (PCBs) are promising systems as indoor power supplier because of simultaneous photo-energy conversion and storage.[7-11] For applying to indoor environment, photovoltaic part in PCB should meet the following requirements: (1) efficient conversion of indoor lighting power, (2) impervious to incident lighting conditions, (3) aesthetic impression, and (4) flexibly controllable open circuit voltage. Dye-sensitized solar cells (DSCs) definitely meet all requirements, so that we adopted DSC as a photo-energy converter in PCB.[12-16]

As the counterpart for energy storage, many kinds of supercapacitors have been employed due to their high power density[17-27], but have intrinsic problems such as low energy density and fast self-discharge.[28] Lithium ion batteries (LIBs) have been suggested as an alternative energy storage part because of high energy density and long cycle-life. However, any photovoltaic cells in a single unit cannot meet their high operating voltage (in general, > 3 V), requiring tandem structural photovoltaic part.[29] Instead, Liming Dai group proposed serial connected perovskite solar cell pack to photo-charge LIB, in which system photovoltaic cell pack and LIB were separated and wire-connected.[30] Moreover, most active materials for LIB have considerably positive Li^+ ion active potential (over 4 $V_{Li+/Li}$ corresponding to 1 V *vs.* normal hydrogen electrode, NHE), so that it is difficult to deliver sufficient output voltage (V_{dCh}) in combination with any photovoltaic electrodes. Some groups reported photo-assisted rechargeable system instead, in which photo-energy was used for reducing external applied voltage during charging.[31-33] Unfortunately, these efforts were far away from all-in-one PCB that satisfies following issues:

i. Being able to charge LIB by a single unit photovoltaic cell

ii. Efficient use of a space

iii. No over-charging problem.

In this work, we developed the photo-rechargeable all-in-one dye-sensitized solar battery (DSSB) using thin graphitic layer-coated lithium manganese oxide ($LiMn_2O_4$) as the electrode-immobilized storage material. $LiMn_2O_4$ is common cathode materials for LIB with two reaction regions, 3 and 4 $V_{Li+/Li}$. Generally, 3 $V_{Li+/Li}$ region is relatively inactive, but introduction of thin graphitic shells allow good Li^+ ion reactivity in 3 $V_{Li+/Li}$ region.[34] Contrary to 4 $V_{Li+/Li}$ region, it is suitable to make V_{dCh} that is defined as redox potential gap between charge regenerator and storage material. This modified $LiMn_2O_4$ storage-electrode was combined with dye-sensitized TiO_2 photo-electrode to realize an all-in-one external power-free PCB. We introduced three kinds of redox mediators as charge regenerator for oxidized dye such as I^-/I_3^-, $Co^{2+/3+}(bpy)_3(PF_6)_{2/3}$, and $Cu^{+/2+}(dmp)_2TFSI_{1/2}$ and investigated the impact of their electrochemical kinetics on the photo-charging/discharging performance depending on light intensity. As for standard light intensity (1 sun, 1000 W m^{-2}), the regeneration ability of redox mediator determined photo-charging current density (J_{Ch}) and thus stored energy density (E_{stored}) rather than V_{dCh}. However, when photo-charged under dim lighting close to indoor lighting, all charge regenerators delivered similar J_{Ch}. As a result, overall photo-energy conversion/storage efficiency ($\eta_{overall}$) was mainly determined by V_{dCh}, instead of J_{Ch}. This is totally different from the result under 1 sun condition. Our findings present the design strategy for indoor-customized photo-rechargeable system.

5.2 Results and discussion

The Working Principle of Dye-sensitized Solar Battery DSSB is an all-in-one photo-electrochemical system based on 3-electrodes including dye-sensitized TiO_2 photo-electrode (PE), surface-graphitized $LiMn_2O_4$ storage-electrode (SE), and catalytic-functionalized LISICON membrane-electrode (ME). **Figure 5.1a** describes the structure and working principle of DSSB. The V_{dCh} of DSSBs corresponds to the potential difference between reduction of charge regenerator and oxidation of $Li_2Mn_2O_4$.[35-36]

The redox potential of storage material should be higher as much as possible compared to that of charge regenerator to maximize V_{dCh}, while not exceeding the fermi level of TiO_2 for external power-free photo-charging. General cathode materials for LIB, lithium transition metal compounds, have too positive active potential to be utilized as storage material in DSSB. Among them, intrinsic $LiMn_2O_4$ has two Li^+ ion reaction regions (3 and 4 $V_{Li+/Li}$), but very poor reactivity in 3 $V_{Li+/Li}$ region due to the low electrical conductivity of the tetragonal phase of $LiMn_2O_4$. This limitation was overcome by high-energy ball-milling process that resulted in nano-sizing and surface-graphitization of $LiMn_2O_4$, facilitating use of 3 $V_{Li+/Li}$ region for energy storage (**Figure 5.1b**).[34] This modified $LiMn_2O_4$ was key factor for realization of all-in-one DSSB.

Next, two kinds of liquid electrolytes (catholyte containing charge regenerators and supporting electrolyte for SE) fill both PE and SE sides, physically separated by ME. The Y123 organic dye having donor-π-acceptor structure was employed as sensitizer because of its good compatibility with metal complexes as well as iodine charge regnerators (I^-/I_3^-).[37] 0.8 M $LiClO_4$ in acetonitrile was introduced at the SE side as a supporting electrolyte. We selected three types of charge regenerators such as I^-/I_3^-, $Co^{2+/3+}(bpy)_3$, and $Cu^{+/2+}(dmp)_2$ to investigate their impact on the photo-charging/discharging performance of DSSBs.[38-42] They show the increasingly down-shifted standard potential in the order of I^-/I_3^- < $Co^{2+/3+}(bpy)_3$ < $Cu^{+/2+}(dmp)_2$ (**Figure 5.1c**), but deteriorating electrochemical kinetics in the reverse order (**Table 5.1**). They are related with V_{dCh} and J_{Ch} of DSSB, respectively.

As for the working mechanism of DSSBs, photo-generated excitons from dyes are separated at the TiO_2/dye interface and then oxidized dyes are reduced by charge regenerator (Eq.5.1).[43] Collected photo-electrons reach the SE through external circuit and successively reduce $LiMn_2O_4$ to $Li_2Mn_2O_4$ (Eq.5.2), accompanying Li+ ions diffusion through ME for charge balance.[44] A thin graphitic layer-coated $LiMn_2O_4$ we employed is electrochemically active near 0.2 V *vs* NHE (**Figure 5.1c**), so that photo-injected electrons in TiO_2 network have sufficient driving force for external power-free photo-charging process.[45] In this manner, incident photo-energy is directly converted and stored as chemical energy, which can be reversibly converted to electric energy whenever needed. In operation mechanism of DSSB, the charging amount depends on the amount of either dye or redox mediator so that there is no over-charging problem.[36, 46-47]

$$M_{1,red} + S^{+} \leftrightarrow M_{1,ox} + S \tag{5.1}$$

$$\mathrm{Li}Mn_2O_4 + Li^{+} + e^{-} \leftrightarrow Li_2Mn_2O_4 \tag{5.2}$$

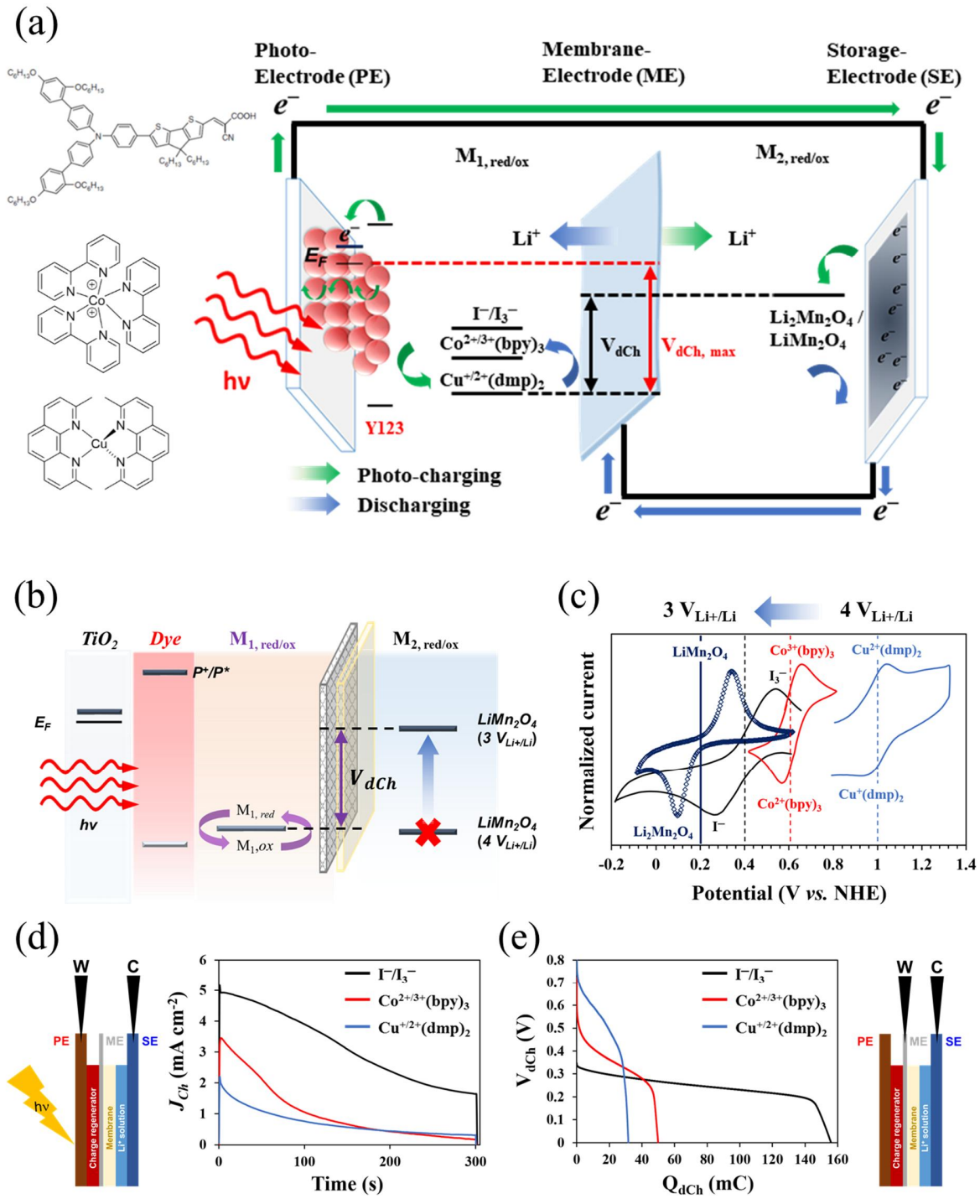

Figure 5.1 (a) The structure and working principle of DSSB. Inset shows the molecular structures of Y123 dye, $Co^{+2/+3}(bpy)_3(PF_6)_{2/3}$, and $Cu^{+/+2}(dmp)_2TFSI_{1/2}$ at left side. (b) The schematic diagram of output voltage formation before (4 $V_{Li+/Li}$) and after (3 $V_{Li+/Li}$) surface-graphatization of $LiMn_2O_4$. (c) Cyclic voltammograms of $Li_2Mn_2O_4/LiMn_2O_4$ (deep blue), I^-/I_3^- (black), $Co^{2+/3+}(bpy)_3(PF_6)_{2/3}$ (red), and $Cu^{+/2+}(dmp)_2TFSI_{1/2}$ (blue) in 0.1 M $LiClO_4$ in acetonitrile. (d) The photo-charging profile for 5 min under one sun condition. Left shows 2-electrode position for the J_{Ch} measurement mode, where working and counter are connected with the PE and the SE, respectively. (e) Galvanostatic discharging profile at a discharging rate of −0.03 mA cm^{-2}. Right shows 2-electrode position for the galvanostatic discharging mode, where working and counter are connected with the ME and the SE, respectively.

Table 5.1 Hybrid Device Performances depending on the Input Power and Kinetic Parameters of All Charge Regenerators

	η_Q [a] (%)				E_{stored} [a] (mWh g^{-1})				η_{reg} [b] (%)	k_0 (cm s^{-1})	D (cm^2 s^{-1})	$R_{CT,\ Ed/El}$ [c] (Ω)	N_{bulk} [c] (Ω)
	P_{in} [a] (W m^{-2})												
	250	400	650	1000	250	400	650	1000		×10^{-4}	×10^{-5}		
I^-/I_3^-	97	100	100	100	11.4	21.8	26.3	30.5	92.7	37.21	2.67	0.14	0.55
$Co^{2+/3+}(bpy)_3$	100	100	100	99	11.7	12.2	12.8	13.8	80.6	15.70	0.99	2.09	9.76
$Cu^{+/2+}(dmp)_2$	100	99	99	99	9.8	11.4	12.5	13.1	65.7	0.25	0.37	15.28	44.55

[a] Coulombic efficiency (η_Q) corresponds to the ratio of discharging capacity (Q_{dCh}) to photo-charging capacity (Q_{Ch}): $\eta_Q = Q_{dCh}/Q_{Ch}$. Total stored energy density in $LiMn_2O_4$ (E_{stored}) corresponds to the gross area below V_{dCh}-Q_{dCh} curve. P_{in} was controlled by the number of mesh plate on the photo-active layer of DSSBs.

[b] Charge regeneration efficiencies were evaluated using TCSPC technique as follows: $\eta_{reg} = 1 - (\tau_{Redox}/\tau_{Inert})$, where τ_{Redox} and τ_{Inert} are the PL lifetime of Y123 monolayer on ZrO_2 surrounded by redox active electrolyte and inert electrolyte, respectively.

[c] Charge transfer resistance at the electrode/electrolyte interface ($R_{CT,\ Ed/El}$) and Nernst diffusion impedance (N_{bulk}) are acquired from impedance spectra of symmetric cells.

We firstly present the temporal photo-charging under 1 sun condition (1000 W m^{-2}) and following galvanostatic discharging profiles with different charge regenerator in **Figure 5.1d** and **5.1e**, respectively. For all the cases, initial J_{Ch} attenuates steeply along with charging time, which is attributed to the rapid depletion of reducing agent (charge regenerator) and up-shifted fermi level of $LiMn_2O_4$ due to charge storage.[48-49] These phenomena diminish the driving force for photo-charging. I^-/I_3^- shows the highest photo-charging capacity (Q_{Ch}) that is corresponding to the gross area below J_{Ch}-time curve for 5 min, followed by $Co^{2+/3+}(bpy)_3$, and $Cu^{+/2+}(dmp)_2$. The resulting discharging capacity (Q_{dCh}) tends to follow the tendency of Q_{Ch}, resulting in 453 C g^{-1} for I^-/I_3^-, 145 C g^{-1} for $Co^{2+/3+}(bpy)_3$, and 92 C g^{-1} for $Cu^{+/2+}(dmp)_2$. As expected, V_{dCh} trend follows the order of standard potential of charge regenerator. Despite the lowest V_{dCh}, I^-/I_3^- achieves the highest E_{stored} of 30.5 mWh g^{-1} because its superior Q_{dCh} overcompensates it, which corresponds to the overall photo-energy conversion/storage efficiency ($\eta_{overall}$) of 0.79%. The $\eta_{overall}$ is defined as following Eq.5.3.[23]

$$\eta_{overall} = \frac{E_{stored}}{P_{in}\, A\, t_{Ch}} \tag{5.3}$$

Where P_{in} is the incident light intensity, A is the active area of PE, and t_{Ch} is the photo-charging time. We also checked the performance of DSSBs at different light intensities, 650, 400, 250 W m^{-2}. It is observed that all the charge regenerators provide almost 100% of Coulombic efficiency (η_Q) at all light intensities (**Table 5.1**). These results clearly show that photo-charging and following discharging are considerably influenced by charge regenerator. As for the origin of different J_{Ch}, it is definitely related with charge injection current according to the charge regenerators. More detailed explanation will be following in next section.

Photo-charging/discharging Performance depending on the Regenerator The measured J_{Ch} can be expressed using the photo-charge injection current density (J_{inj}) and the charge loss current density (J_{Loss}) as described in **Figure 5.2a**[50-52]:

$$J_{Ch} = J_{inj} - J_{Loss} \tag{5.4}$$

From this, J_{inj} was estimated as a function of light intensity (see explanation of **Figure 5.3** for details). As shown in **Figure 5.2b**, I^-/I_3^- exhibits always the highest J_{inj} and is followed by $Co^{2+/3+}(bpy)_3$ and $Cu^{+/2+}(dmp)_2$. We pay attention to fact that the J_{inj} trend well matches that of J_{Ch} and reach an understanding that J_{Ch} trend is mainly determined by J_{inj}. It is given by dividing measured photo-current density (J_{SC}) , here J_{Ch}, by charge collection efficiency (η_{CC}) as Eq.5.5[53]:

$$J_{inj} = J_{SC}/\eta_{CC} = J_{Ch}/\eta_{CC} = q\,\eta_{lh}\,\eta_{inj}\,\eta_{reg}\,I_0 \tag{5.5}$$

Where q is the elementary charge, I_0 is the incident photon flux, η_{lh} is the light harvesting efficiency, η_{inj} is the charge injection efficiency, and η_{reg} is the charge regeneration efficiency. Given the facts that All PEs were fabricated in the same conditions and only charge regenerator was controlled, η_{reg} must be decisive factor for the J_{inj}. The η_{reg} values were estimated by transient photoluminescence (PL) decay method, in which PL lifetimes of Y123 monolayer on ZrO_2 were compared according to the presence of charge regenerator in the electrolyte (see **Table 5.2** for detailed procedure).[54] **Figure 5.4** shows resulting PL decay signals with different charge regenerator and quantitative values are summarized in **Table 5.2**. The maximum η_{reg} is recorded with I^-/I_3^- (93%), while $Co^{2+/3+}(bpy)_3$ and $Cu^{+/2+}(dmp)_2$ provide relatively lower η_{reg} values (81% and 66%, respectively). This well matches the J_{inj} as well as J_{Ch} trends.

Further detailed discussion on η_{reg} will be followed because the charge regeneration ability of redox mediators in DSCs can be affected by following three factors: (1) potential difference (driving force) between ground-state oxidation of dye and standard potential of charge regenerator, (2) charge transfer rate, and (3) ionic diffusion coefficient.[55-57] We evaluated the charge transfer and diffusion ability of three types of charge regenerators in terms of rate constant (k_0), ionic diffusion coefficient (D) measured by linear sweep voltammetry and charge transfer resistance at the electrode/electrolyte interface ($R_{CT,\ Ed/El}$), Nernst diffusion impedance in the electrolyte (N_{bulk}) measured by impedance spectroscopy, respectively (detailed explanations are in Experimental Section).[58-60] As summarized in **Table 5.1**, I^-/I_3^- provides the highest k_0 (37.21×10^{-4} cm s^{-1}) and D (2.67×10^{-5} cm^2 s^{-1}), followed by $Co^{2+/3+}(bpy)_3$ and $Cu^{+/2+}(dmp)_2$. Accordingly, the $R_{CT,\ Ed/El}$ and N_{bulk} appear in the following order: $Cu^{+/2+}(dmp)_2 > Co^{2+/3+}(bpy)_3 > I^-/I_3^-$. We note the

extremely low $R_{CT,\ Ed/El}$ (0.14 Ω) and N_{bulk} (0.55 Ω) for I^-/I_3^-. All kinetic parameters are consistent with the trend of η_{reg}, which definitely explains why I^-/I_3^- best preforms as charge regenerator in DSSBs.

As for the galvanostatic discharging process in which oxidized charge regenerators are reduced at the ME/catholyte interface (**Figure 5.2a**), the reactivity and diffusion ability of charge regenerator are closely connected with discharging rate-dependence of η_Q. **Figure 5.2c** shows the discharging rate-dependence of η_Q with different charge regenerator. For all cases, DSSBs are photo-charged for 5 min under 1 sun condition before discharging. As the discharging current increases, I^-/I_3^- keeps up with the Q_{Ch} even at −0.28 mA cm^{-2} of discharging rate and thus facilitates almost 100% of η_Q. However, $Co^{2+/3+}(bpy)_3$ and $Cu^{+/2+}(dmp)_2$ show irreversible Q_{dCh}, especially $Cu^{+/2+}(dmp)_2$ exhibits poor η_Q below 70% even at −0.28 mA cm^{-2} of discharging rate. This result corresponds to the order of k_0 and D, I^-/I_3^- > $Co^{2+/3+}(bpy)_3$ > $Cu^{+/2+}(dmp)_2$. However, photo-charging/discharging performance of DSSB was totally different under dim lighting conditions close to indoor light intesity.

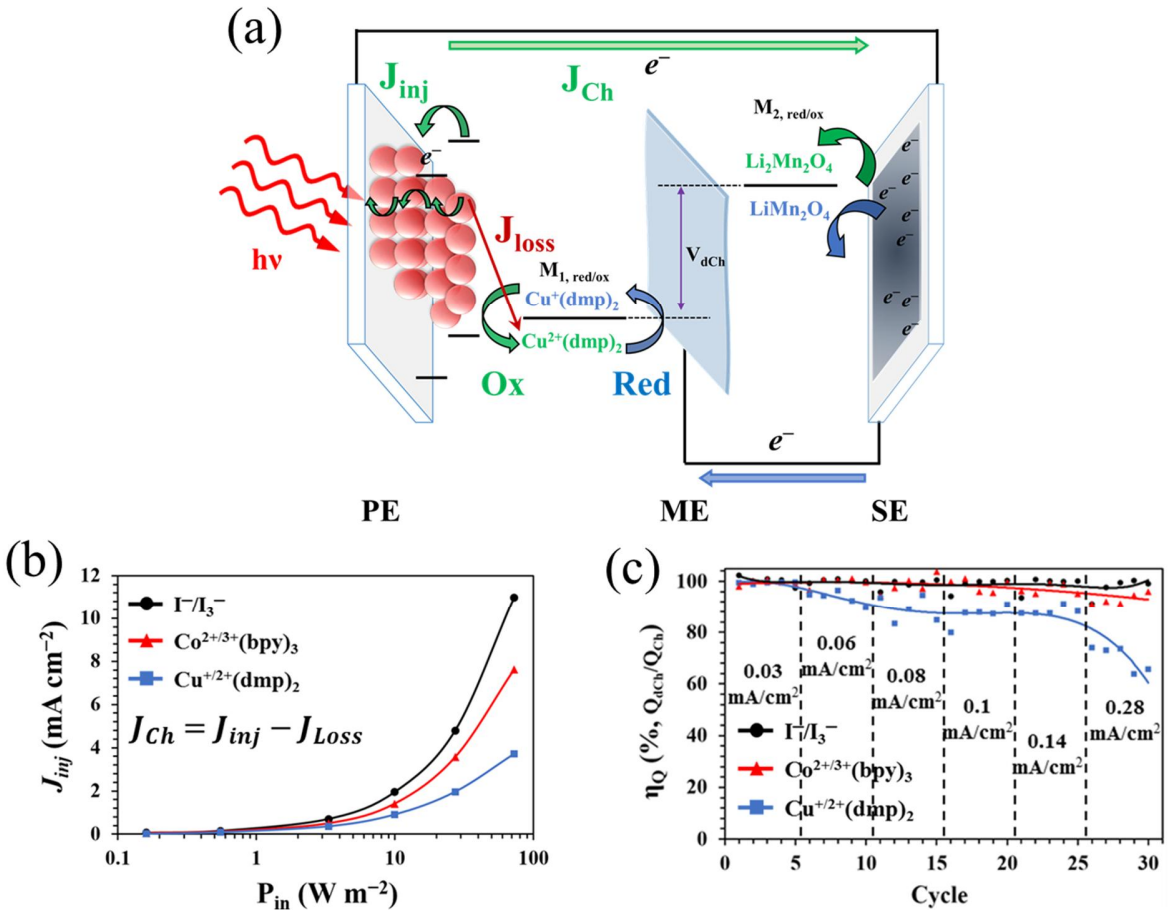

Figure 5.2 (a) Factors influential for photo-charging and galvanostatic discharging performance. Under the illumination, photo-charge is injected (J_{inj}) from dye and diffuses through TiO_2 network until either collected (J_{Ch}) at the electrode or recaptured (J_{Loss}) by oxidized charge regenerator. During the galvanostatic discharging, oxidized charge regenerator is reduced again at the ME/catholyte interface. (b) The J_{inj} profile as a function of incident light intensity, estimated using the J_{Ch} and J_{Loss}. (c) Discharging rate-dependence of η_Q. Symbols corresponds to experimental values, while trend lines are fitted.

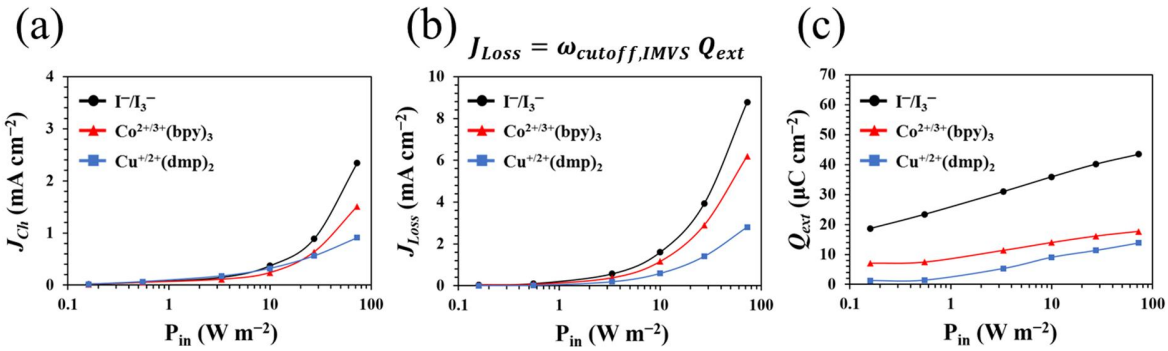

Figure 5.3 (a) Photo-charging current (J_{Ch}) and (b) charge loss current (J_{Loss}) as a function of photon flux. J_{Loss} is derived from recombination time that is derived from cutoff angular frequency ($\omega_{cutoff,\,IMVS}$) of photo-voltage efficiency frequency response spectra in the complex plane and (c) the extracted charge amount (Q_{ext}) from the TiO_2 network at the open circuit state under the illumination ($J_{Loss} = \omega_{cutoff,IMVS}\, Q_{ext}$).

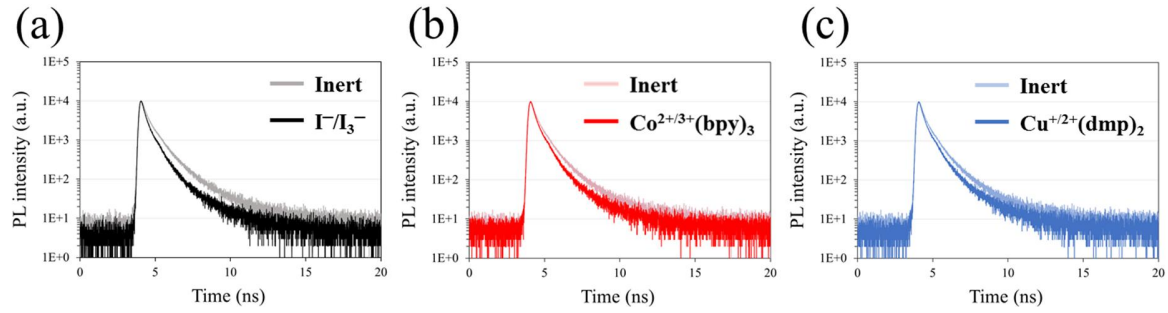

Figure 5.4 PL decay signals detected from Y123 dyed ZrO_2 layer surrounded by different redox mediator: (a) I^-/I_3^-, (b) $Co^{+2/+3}(bpy)_3(PF_6)_{2/3}$, and $Cu^{+/+2}(dmp)_2TFSI_{1/2}$.

Table 5.2 Fitting parameters for estimating average exciton lifetimes in Y123 monolayer on ZrO_2 and regeneration efficiency according to redox mediator.

	Concen. (mol)	A_1	τ_1 (ns)	A_2	τ_2 (ns)	A_3	τ_3 (ns)	τ_{ext} [a] (ns)	η_{reg} [b]
Inert	-	28857.4	0.276	3729.0	1.026	272.3	2.873	0.382	0
I^-/I_3^-	0.2 / 0.1	262804.0	0.010	14172.6	0.311	620.3	1.428	0.028	0.927
$Co^{2+/3+}$	0.2 / 0.06	72535.1	0.023	12351.3	0.327	452.5	1.373	0.074	0.806
$Cu^{+/2+}$	0.2 / 0.04	26355.0	0.048	8408.0	0.344	314.5	1.331	0.131	0.657

[a] Exciton lifetime was estimated by fitting transient PL spectra, followed by equalization of the whole spectra. FlouFit software was employed for fitting with a multi exponential model, $I(t) = \int_{-\infty}^{t} IRF(t') \sum_{t=1}^{n} A_i e^{-(t-t'/\tau_i)}\, dt'$, where *IRF(t')* is the experimentally measured instrument response function (lamp function), A_i is the amplitude of the i^{th} component at time zero in counts, τ_i is the lifetime of the i^{th} component and t is the time shift between *IRF(t')* and decay. For determining the average exciton lifetime, three exponential functions were used and quantitative values were derived from the resulting fitting signals by equalizing fitting signals as follows: $I(t) = A_1 e^{-(t/\tau_1)} + A_2 e^{-(t/\tau_2)} + A_3 e^{-(t/\tau_3)}$.

[b] Regeneration efficiency was estimated as follows: $\eta_{reg} = 1 - \left({}^{\tau_{redox}}/_{\tau_{inert}}\right)$, where τ_{redox} is the exciton lifetime of dyes with redox mediator in the electrolyte, and inert is the exciton lifetime of dyes with inert electrolyte

The Photo-Energy Conversion/Storage Performance under Dim Lighting We carried out photo-charging of DSSB under dim lighting. To simulate the condition of dim lighting, a commercial white LED was employed and the active layer of PE was covered with the self-made mesh plate. Incident light intensity flexibly varied according to the number of mesh plate (see **Figure 5.6** and **Table 5.4** for actual lighting system and intensity). Under dim lighting conditions, the performance of DSSBs are evaluated in terms of the $\eta_{overall}$ (**Figure 5.5a** and **Table 5.3**).

It is noteworthy that the trend of $\eta_{overall}$ changes when attenuating the light intensity. I^-/I_3^- and $Co^{2+/3+}(bpy)_3$ deliver the similar $\eta_{overall}$ (ca. 8.7% and 9.0%) at an intensity of 8.85 W m^{-2} (2670 lux), while $Cu^{+/2+}(dmp)_2$ delivers relatively lower $\eta_{overall}$ (7.3%). However, $Cu^{+/2+}(dmp)_2$ starts overtaking others from an intensity of 5.08 W m^{-2} (1520 lux) and eventually reaches the best $\eta_{overall}$ (8.8%) at an intensity of 1.37 W m^{-2} (410 lux), corresponding to general office illuminance.[61-63] $Co^{2+/3+}(bpy)_3$ also delivers good $\eta_{overall}$ (7.9%) at the same intensity, even though it is slightly lower than that of $Cu^{+/2+}(dmp)_2$.

To explain the $\eta_{overall}$ trend, we observed the photo-charging and galvanostatic discharging profiles (**Figure 5.5c – 5.5h**). At an intensity of 8.85 W m^{-2}, I^-/I_3^- shows the highest J_{Ch} and thus Q_{dCh} while the $Cu^{+/2+}(dmp)_2$ delivers the highest V_{dCh}, but the poor Q_{dCh}. As the light intensity decreases to 1.37 W m^{-2}, all devices deliver dramatically decreased and finally similar J_{Ch} each other. In contrast, remarkable difference is still observed in V_{dCh} as the light intensity decreases and $Cu^{+/2+}(dmp)_2$ shows the highest V_{dCh}. These mean that the tendency of $\eta_{overall}$ under dim lighting is mainly dependent on the V_{dCh} rather than Q_{dCh}. Therefore, $Cu^{+/2+}(dmp)_2$ with the most positive standard potential is the most suitable charge regenerator of DSSBs for indoor applications. Finally, using $Cu^{+/2+}(dmp)_2$ based DSSBs, we successfully operated melody-kit after 5 min photo-charging under commercial compact fluorescent lamp (**Figure 5.6c**, 2.36 W m^{-2}, 800 lux).

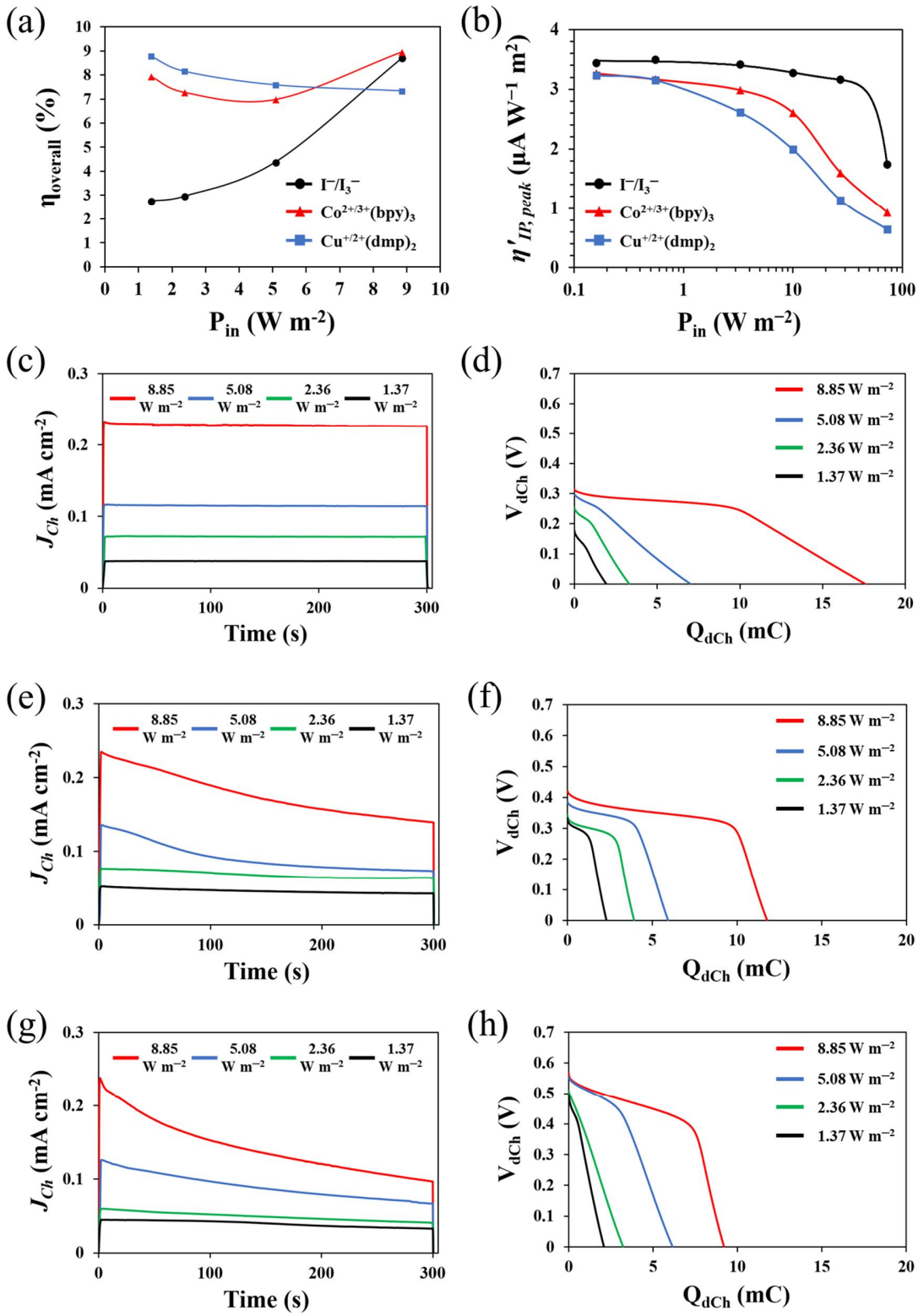

Figure 5.5 (a) Light intensity dependent photo-energy conversion/storage efficiency ($\eta_{overall}$) of DSSBs under dim lighting. (b) Light intensity-dependence of $\eta_{IP}'_{peak}$ measured by CIMPS. Note the difference of $\eta_{IP}'_{peak}$ becomes negligible as light intensity decreases. (c, e, g) Temporal photo-charging current (J_{SC}) profiles for 5 min under dim lighting and (d, f, h) following galvanostatic discharging profiles at a discharging rate of −0.03 mA cm^{-2}, with different charge regenerator: (c, d) I^-/I_3^-, (e, f) $Co^{2+/3+}(bpy)_3$, and (g, h) $Cu^{+/2+}(dmp)_2$.

Table 5.3. Performance Data of DSSBs under Dim Lighting and Light Intensity-Dependence of $\eta_{IP}'_{peak}$, corresponding to **Figure 5.5a** and **5.5b**.

	$\eta_{overall}$ [a] (%)				$\eta_{IP}'_{peak}$ [b] (μA W^{-1} m^2)					
P_{in} (W m^{-2})	1.37	2.36	5.08	8.85	0.2	0.6	3.3	10.0	27.3	72.8
Illuminance (lux)	410	800	1520	2670	70	240	1150	3170	7900	21100
I^-/I_3^-	2.8	3	4.4	8.7	3.4	3.5	3.4	3.3	3.2	1.7
$Co^{2+/3+}(bpy)_3$	7.9	7.3	7.0	9.0	3.3	3.2	3.0	2.6	1.6	0.9
$Cu^{+/2+}(dmp)_2$	8.8	8.2	7.6	7.3	3.2	3.2	2.6	2.0	1.1	0.6

[a] Commercial white light emitting diode was used as light source to simulate dim lighting condition.

[b] Photo-charging current efficiency (η_{IP}) corresponds to the ratio of photo-charging current (I_{Ch}) to incident light intensity (P_{in}): $\eta_{IP} = I_{Ch}/P_{in}$. $\eta_{IP}'_{peak}$ is maximum value of real part (η_{IP}') of photo-charging current efficiency frequency response. Monochromatic light emitting diode (503 nm) was used as light source to measure η_{IP}. Intensity was automatically controlled based on photo-diode.

To clearly understand light intensity dependence of J_{Ch} of DSSB, we measured light source frequency response of photo-charging current efficiency ($\eta_{IP} = I_{Ch}/P_{in}$) using controlled intensity modulated photo-spectroscopy (CIMPS) equipped with monochromatic light emitting diode (503 nm), where I_{Ch} is the photo-charging current.[64] Corresponding maximum values ($\eta_{IP}'_{peak}$) of η_{IP} are summarized in **Figure 5.5b** and **Table 5.3**. We note that the difference of $\eta_{IP}'_{peak}$ between charge regenerators becomes gradually negligible as light intensity decreases. Over 10.0 W m^{-2} of intensity (3170 lux), I^-/I_3^- exhibits much higher $\eta_{IP}'_{peak}$ compared to others. In contrast, the similar $\eta_{IP}'_{peak}$ values are observed below 0.6 W m^{-2} of intensity (240 lux) for all charge regenerators, which means the similar J_{Ch}. This exactly correponds to abovementioned J_{Ch} trend.

In brief, the dependence of J_{Ch} on the charge regenerator mainly results from the η_{reg} trend and is apparent under 1 sun condition. However, as the light intensity decreases, the effect of η_{reg} becomes gradually negligible because the number of photon flux is insufficient to oxidize all dyes (ca. 9.6×10^{19} m^{-2}) on TiO_2 film under the weak illumination (ca. 4.7×10^{19} m^{-2} s^{-1} of photon flux at 10 W m^{-2}). As a result, the V_{dCh} starts showing strong impact on the $\eta_{overall}$ from 5.08 W m^{-2}.

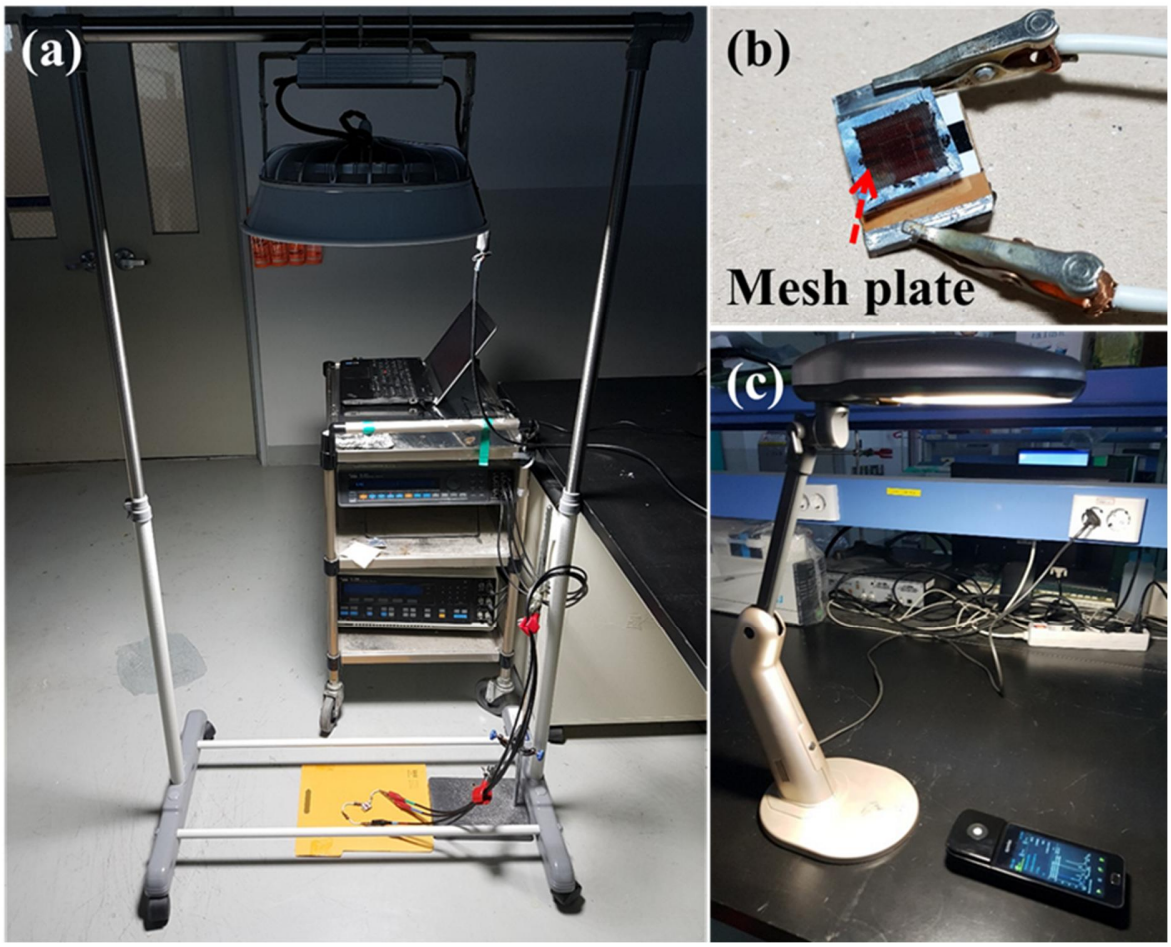

Figure 5.6 (a) Home-made lighting system using white LED, (b) Mesh plate on DSSB, and (c) Commercial desk lighting used for melody-kit operation and cycling test.

Table 5.4 Incident light intensity and corresponding illuminance according to the number of mesh plate on an illuminometer.

	0 Layer	1 Layer	2 Layer	3 Layer	Desk lighting
P_{in} (W m^{-2})	8.85	5.08	2.2	1.37	2.36
Illuminance (lux)	2670	1520	660	410	800

The Self-Discharge Rate and Cycle Life We also investigated the correlation between charge regenerator and durability of stored chemical energy converted from photo-energy. Stored photo-charge in the SE can be self-discharged through two routes, either ME/catholyte interface or TiO_2/catholyte interface. The self-discharge rate depending on the charge regenerator was monitored in two types of discharge modes, where the SE and the PE are either not connected (discharge mode-1) or connected (discharge mode-2). **Figures 5.7a** and **5.7b** present the temporal open circuit voltage (V_{OC}) between the ME and the SE. All charge regenerators seem to be negligible V_{OC} decay even after 100 h in the discharge mode-1, while huge V_{OC} decays are observed in the discharge mode-2. This result clearly reveals that TiO_2/catholyte interface is a main route for the self-discharge and the reason might be related with stepwise energy level of $Li_2Mn_2O_4$ > TiO_2 > $M_{1,\ red/ox}$.[65-66]

However, as shown in **Figure 5.7c – 5.7e**, the actual residual capacities do not correspond with abovementioned V_{OC} decays and very dependent on the charge regenerators. In discharge mode-1, I^-/I_3^- (98%) preserves almost initial capacity while $Co^{2+/3+}(bpy)_3$ (35%) and $Cu^{+/2+}(dmp)_2$ (68%) lose considerable amount of charge. In discharge mode-2, residual capacities dramatically reduced compared with discharge mode-1. I^-/I_3^- (56%) remains half initial capacity while $Co^{2+/3+}(bpy)_3$ (0.2%) and $Cu^{+/2+}(dmp)_2$ (4%) completely loss all stored charge. Based on these results, we confirm that the TiO_2/catholyte interface is main route of self-discharge. In addition, it is noteworthy fact that the trend of self-discharge rate according to charge regenerators is related with charge recombination rates at the TiO_2/catholyte interface.

Figure 5.8 shows the charge recombination time (τ_n) in TiO_2 network according to the charge regenerator. I^-/I_3^- gives the longest τ_n, followed by $Cu^{+/2+}(dmp)_2$ and $Co^{2+/3+}(bpy)_3$. This τ_n order inversely agrees with that of self-discharge rate, $Co^{2+/3+}(bpy)_3$ > $Cu^{+/2+}(dmp)_2$ > I^-/I_3^-, suggesting that the self-discharge rate is highly dependent on the recombination rate with oxidized charge regenerator.

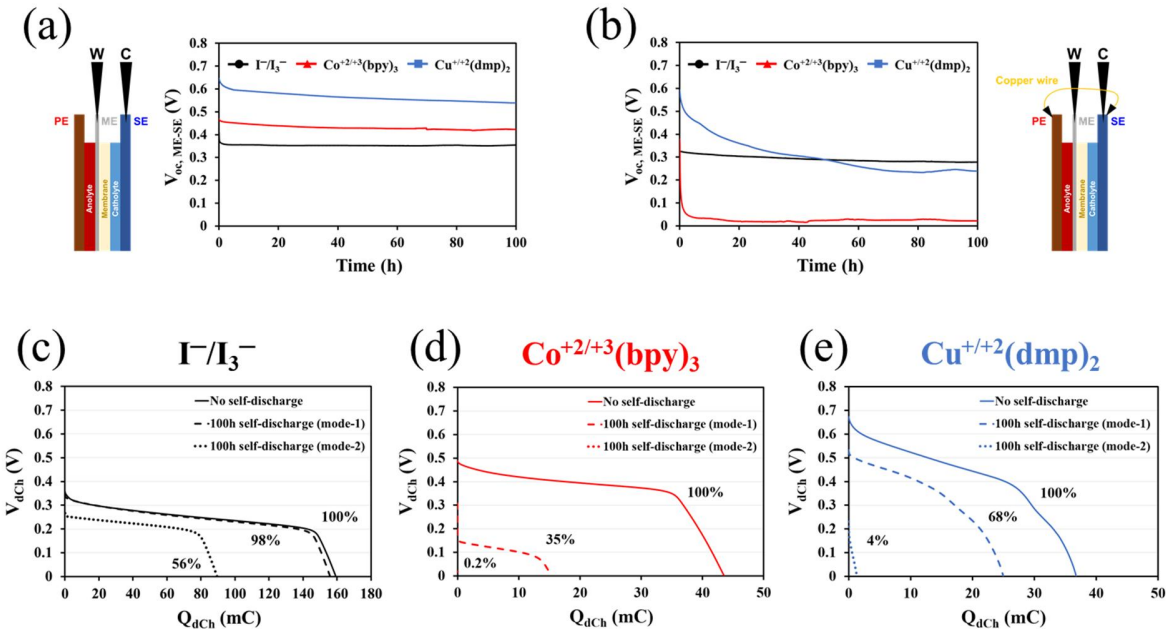

Figure 5.7 Open circuit voltage monitoring for 100 h in the different discharge mode: (a) discharge mode-1 and (b) discharge mode-2. Galvanostatic discharging profiles of DSSBs with different charge regenerator: (c) I^-/I_3^-, (d) $Co^{2+/3+}(bpy)_3(PF_6)_{2/3}$, and (e) $Cu^{+/2+}(dmp)_2TFSI_{1/2}$ before and after self-discharge test. Self-discharge test was carried out for 100 hours. Note the huge difference of self-discharge rate according to discharge mode.

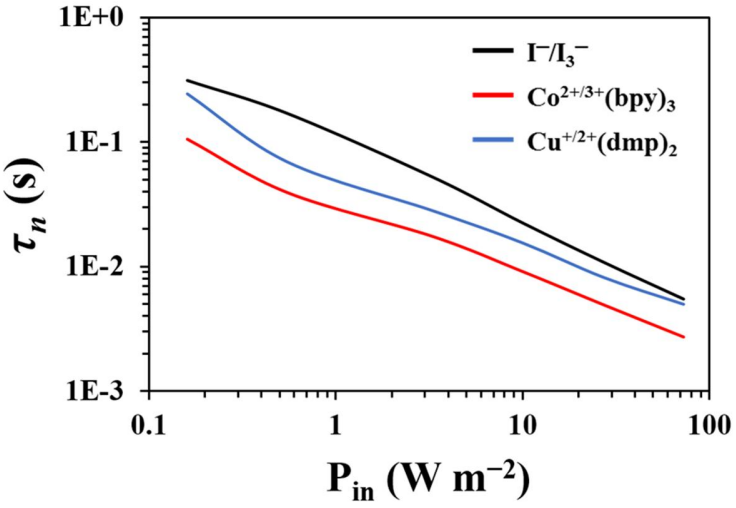

Figure 5.8 Charge recombination time (τ_n) in TiO_2 network at the open circuit state as a function of incident photon flux, which is derived from the cutoff angular frequency of photo-voltage efficiency frequency response spectra in the complex plane as follows: $\tau_n = 1/\omega_{cutoff,IMVS}$ (raw data is not shown).

Lastly, cycling stability was tested through the photo-charging (1000 W m^{-2})/galvanostatic discharging (−0.03 mA cm^{-2}) process as one cycle. **Figure 5.9** plots the η_Q values (black filled circle) for total 50 cycles of photo-charging/discharging with corresponding Q_{Ch} (red filled square) and Q_{dCh} (blue filled square). It is observed that both I^-/I_3^- and $Co^{2+/3+}(bpy)_3$ exhibit near 100% of η_Q the whole cycling test, which means that most stored photo-charge in $LiMn_2O_4$ layer can be extracted reproducibly. However, $Cu^{+/2+}(dmp)_2$ delivers somewhat fluctuating η_Q during the cycling test. We attribute this unstable photo-charging/discharging performance to slow ionic kinetics of $Cu^{+/2+}(dmp)_2$. Initial rapid enhancement of η_Q is observed for all the cases. This results from the dense $LiMn_2O_4$ layer as shown in SEM images (**Figure 5.11a** and **5.11b**), which retards electrolyte infiltration. Moreover, I^-/I_3^- shows the continuous increase of capacity until 10 cycles. As photo-charging/discharging cycles are repeated, $LiMn_2O_4$ clusters agglomerated during the ball milling process gradually disassemble due to continuous volume change of each particle by Li ion intercalation, so that more Li ion pathways are activated.[34] This activation process is more apparent for the case of I^-/I_3^- because of much higher Q_{Ch}.

However, under commercial desk lighting (1.28 W m^{-2}, 450 lux), the $Cu^{+/2+}(dmp)_2$ also delivered stable and reproducible performance over 100 cycles (**Figure 5.10**). In other words, the ionic kinetic issue becomes less important under dim lighting.

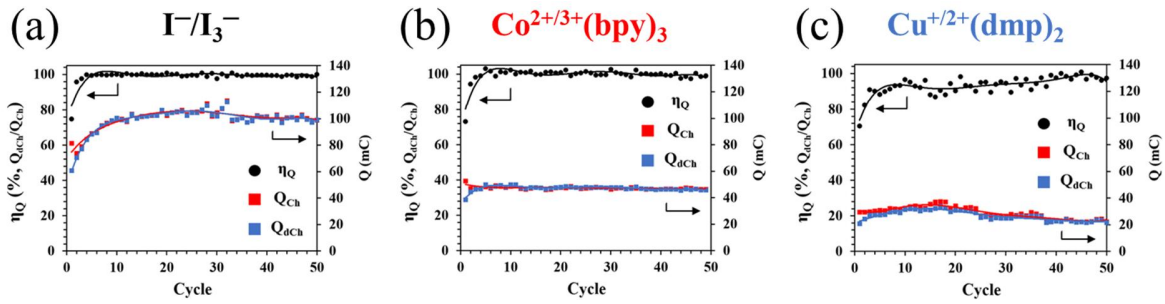

Figure 5.9 1 sun photo-charging/discharging cycling test of DSSBs with different charge regenerator: (c) I^-/I_3^-, (d) $Co^{2+/3+}(bpy)_3$, and (e) $Cu^{+/2+}(dmp)_2$.

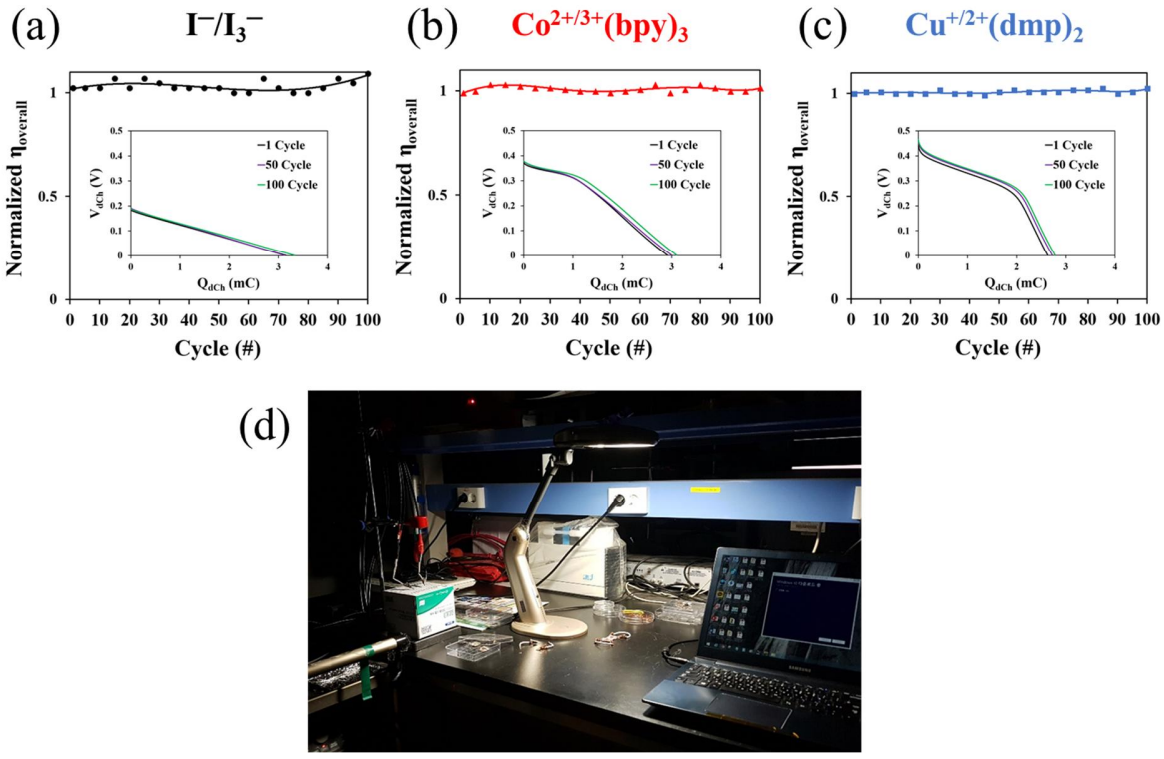

Figure 5.10 Desk lighting photo-charging/discharging cycling test of DSSBs with different charge regenerator: (c) I^-/I_3^-, (d) $Co^{2+/3+}(bpy)_3$, and (e) $Cu^{+/2+}(dmp)_2$. Inset shows galvanostatic discharging profiles at 1, 50, and 100 cycles. (d) Real photograph taken during the measurement.

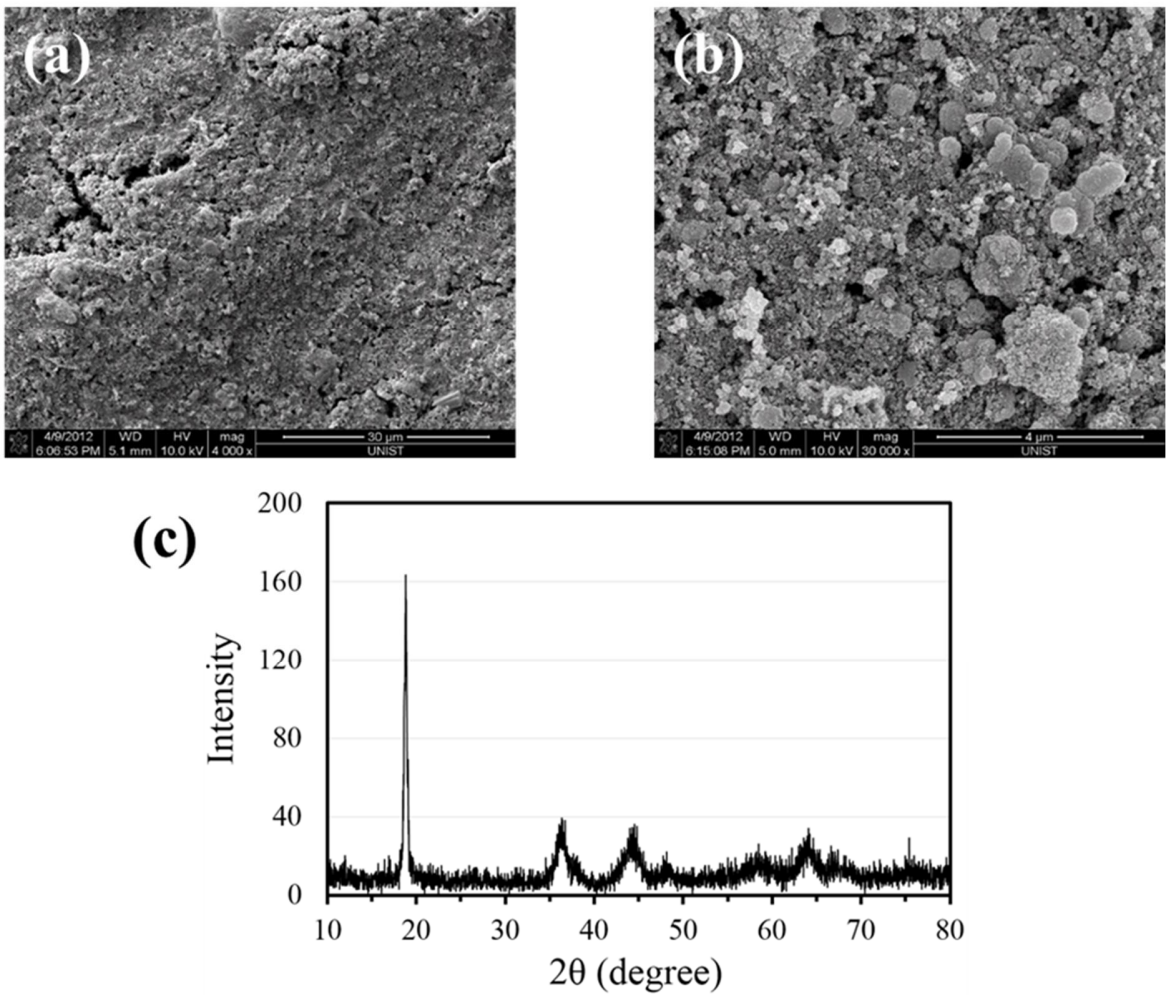

Figure 5.11 The plane SEM images of $LiMn_2O_4$ film in a (a) low and (b) high magnification, same with that used for storage electrode in DSSBs. (c) XRD pattern of surface-graphitized $LiMn_2O_4$ powder.

The light intensity dependence of η_{IP} For fundamental insight into the light intensity-dependence of photo-charging current, we observed light source frequency response of photo-charging current efficiency ($\eta_{IP} = I_{Ch}/P_{in}$) according to the light intensity using controlled intensity modulated photo-spectroscopy (CIMPS) equipped with monochromatic light emitting diode (503 nm).[64] **Figure 5.12a** shows the real (η_{IP}') and imaginary (η_{IP}'') parts of photo-charging current efficiency frequency response at 72.8 W m^{-2} of intensity. As expected, I^-/I_3^- provides the highest η_{IP}' peak ($\eta_{IP}'_{peak}$) and is followed by $Co^{2+/3+}(bpy)_3$ and $Cu^{+/2+}(dmp)_2$, which trend is consistent with the photo-charging current density (J_{Ch}) order. Whereas I^-/I_3^- is also characterized by the biggest η_{IP}' decay at the lowest frequency (10^{-1} Hz). However, these tendencies gradually change as light intensity decreases:

i. The difference of $\eta_{IP}'_{peak}$ between them becomes gradually negligible with decreasing light intensity
ii. I^-/I_3^- starts exhibiting the smallest η_{IP}' decay from 3.3 W m^{-2} (ca. 1150 lux) as shown in **Table 5.5**.

To clearly understand such findings, we need to consider sequential process; photo-charge injection from dye to TiO_2 and following charge collection. In short, it is logical inference that η_{IP}'peak and frequency-dependent η_{IP}' decay are related to charge injection and charge diffusion in the PE, respectively. The correlation between J_{Ch} and charge injection is minutely investigated above. This section focus on the correlation between η_{IP}' decay and effective charge diffusion coefficient (D_n).

DSSBs based on I^-/I_3^- exhibit the biggest η_{IP}' decay, but negligible η_{IP}' decay below 3.3 W m^{-2} of intensity. We calculated the ratio of minimum η_{IP}' to maximum η_{IP}' to compare the degree of frequency-dependent η_{IP}' decay as follows: $\delta_{IP} = 1 - (\eta'_{IP\,static}/\eta'_{IP\,peak})$, where δ_{IP} is the frequency-dependent η_{IP}' decay factor, $\eta_{IP}'_{static}$ is the η_{IP}' at the lowest frequency (10^{-1} Hz) and $\eta_{IP}'_{peak}$ is the η_{IP}' at the cutoff frequency. As summarized in **Table 5.5**, I^-/I_3^- shows rapid fall of δ_{IP} from 3.3 W m^{-2} of intensity. The trend of δ_{IP} can be explained by the electron diffusion in TiO_2 network. **Figure 5.12b** and **Table 5.5** shows that I^-/I_3^- delivers the lowest D_n at over 27.3 W m^{-2} of intensity (ca. 7900 lux) but starts higher than others at below 3.3 W m^{-2} of intensity. This D_n trend inversely corresponds to δ_{IP} trend, indicating that the tendency of δ_{IP} is correlated with the D_n. The D_n is intimately associated with the relative charge amount in TiO_2 conduction band to that in trap state.[67-68] In other words, it is expected that the oxidized species (I_2 and I_3^-) in the I^-/I_3^- catholyte make a huge amount of charge trapped in TiO_2 surface state under the illumination, but such effect becomes smaller as light intensity extremely decreases. Although most practical light sources are based on dc power supply, the δ_{IP} would be important factor of photo-charging for some special cases, such as either flickering or battery-deficient lighting.

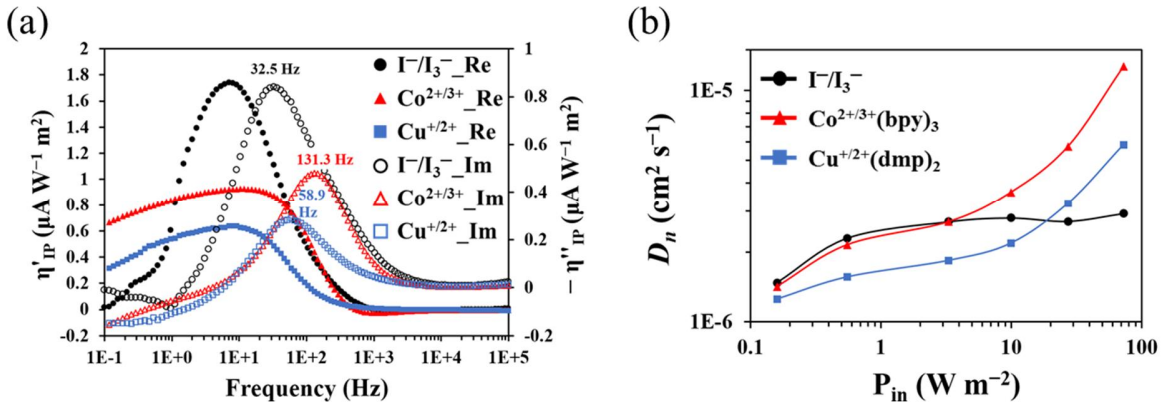

Figure 5.12 (a) The real (η_{IP}', filled symbol) and imaginary (η_{IP}'', blank symbol) parts of photo-charging current efficiency frequency response at 72.8 W m^{-2} of intensity. (b) The light intensity dependent effective charge diffusion coefficient (D_n) of photo-injected electrons during the photo-charging, which is derived from charge transport time.

Table 5.5 Kinetic Data as a function of Photon Flux, Measured from the DSSBs with Different Charge Regenerator

	$\eta_{IP}'_{peak}$ [a] (μA W^{-1} m^2)						δ_{IP} [b] (%)						D_n [c] (×10^{-6} cm^2 s^{-1})					
	P_{in} [d]																	
W m^{-2}	0.2	0.6	3.3	10.0	27.3	72.8	0.2	0.6	3.3	10.0	27.3	72.8	0.2	0.6	3.3	10.0	27.3	72.8
Lux	70	240	1150	3170	7900	21100	70	240	1150	3170	7900	21100	70	240	1150	3170	7900	21100
I^-/I_3^-	3.4	3.5	3.4	3.3	3.2	1.7	0	0.1	1.0	31.0	98.6	99.1	1.5	2.3	2.7	2.8	2.7	2.9
$Co^{2+/3+}$	3.3	3.2	3.0	2.6	1.6	0.9	0.2	1.8	9.1	24.6	29.6	28.1	1.4	2.1	2.7	3.6	5.7	12.7
$Cu^{+/2+}$	3.2	3.2	2.6	2.0	1.1	0.6	2.0	7.0	17.8	30.2	22.6	51.1	1.3	1.6	1.8	2.2	3.2	5.8

[a] $\eta_{IP}'_{peak}$ is maximum value of real (η_{IP}') part of photo-charging current efficiency frequency response.

[b] The frequency-dependent η_{IP}' decay factor (δ_{IP}) is calculated as follows: $\delta_{IP} = 1 - (\eta'_{IP\,static}/\eta'_{IP\,peak})$, where $\eta_{IP}'_{static}$ is the η_{IP}' at the lowest frequency (10^{-1} Hz).

[c] The effective charge diffusion coefficient (D_n) is derived from the cutoff frequency of photo-charging current efficiency frequency response spectra in the complex plane as follows: $D_n = \omega_{cutoff,IMPS}\, L^2/\xi$, where $\omega_{cutoff,\,IMPS}$ is the cutoff angular frequency in the η_{IP}'' plot, L is the TiO_2 film thickness, and ξ is a numerical factor that depends on the optical density of the film.

5.3 Conclusion

This work presents all-in-one photo-rechargeable system, dye-sensitized solar battery (DSSB), which requires no external power for energy storage. Three types of redox mediators, such as I^-/I_3^-, $Co^{2+/3+}(bpy)_3$, and $Cu^{+/2+}(dmp)_2$, were introduced as charge regenerator for oxidized dyes and their impact on the device performance was thoroughly investigated according to the incident light intensity. Major findings are follows: i) electrochemical kinetics of charge regenerator is directly connected with the photo-charging/discharging capacities (Q_{Ch} /Q_{dCh}) and thus stored energy density (E_{stored}). Therefore, I^-/I_3^- exhibited the highest Q_{dCh} (453 C g^{-1}) and E_{stored} (30.5 mWh g^{-1}) under 1 sun condition with good cycling stability. However, ii) all charge regenerators deliver similar Q_{Ch} under extremely low light intensity, instead, output voltage (V_{dCh}) becomes more critical for E_{stored}. As a result, $Cu^{+/2+}(dmp)_2$ delivered the highest overall photo-energy conversion/storage efficiency (25.6 %) under indoor lighting intensity (0.47 W m^{-2}, 120 lux) with over 100 cycling stability. In addition, we found out that self-discharge of stored charge not only mainly occurs through TiO_2/catholyte interface, but also depends on the recombination rate with oxidized charge regenerators in the order: I^-/I_3^- < $Cu^{+/2+}(dmp)_2$ < $Co^{2+/3+}(bpy)_3$. DSSB proposed here is very useful photo-rechargeable system for indoor environment because of easy V_{dCh} control through material modification, efficient power conversion of dim lighting, and all-in-one structure that is featured by aesthetic impression as well as no over-charging problem. As social concerns about energy saving increase, the development of indoor/outdoor-customized photo-rechargeable system would be increasingly required regarding the scope of application, which is also our future research theme.

5.4 Experimental Section

Storage-Electrode Fabrication Storage-electrode was composed of $LiMn_2O_4$ as an active material, Super P(Timcal) carbon black as a conduction enhancer and polyvinylidene fluoride (PVdF, SOLVAY Solef 5130) as a binder (weight ratio of 8:1:1) on the Au-coated FTO. Firstly, PVdF powder was dissolved in *N*-methyl pyrrolidinone (NMP). Mixture of $LiMn_2O_4$ and Super P was finely dispersed into the PVdF/NMP paste with stirring. The Au-coated FTO glass was pre-drilled for electrolyte injection and masked using kapton tape (25.4 μm). The $LiMn_2O_4$ slurry was dropped onto the masked substrate, followed by drying at 110 °C for 1 h and naturally cooling to 25 °C. The active area was 0.6×0.6 cm^2 and the loading density of $LiMn_2O$ ranged 1 ~ 2.2 mg/cm^2.

Cell Assembly Storage-electrode and LISICON membrane were attached using the 60-μm Surlyn® resin (Meltonix 1170-60, Solaronix SA) at 110 °C. Then, upper side of LISICON was masked with kapton tape and Pt-sputtered for making 3 mm width Pt layer as a charge collector using FEI-sputter (K575X, EMITECH), followed by electrodeposition of poly(3,4-ethylenedioxythiophene) (PEDOT) on that as a catalytic layer. The electrodeposition was carried out applying a constant current (+0.5 mA) for 30 s in an acetonitrile dispersion of EDOT containing 0.01 M EDOT (97%, Aldrich) and 0.1 M $LiClO_4$ (99.99% trace metals basis, Aldrich). Then, photo-electrode was attached on that using 2 layers of 60-μm Surlyn® resin at 110 °C. Both internal spaces for photo-electrode side and storage-electrode side were filled with catholyte and 0.8 M $LiClO_4$ in acetonitrile, respectively. I^-/I_3^- catholyte was composed of 0.2 M I_2 (≥ 99.8%, Aldrich), 0.1 M LiI (99.9% trace metals basis, Aldrich), 0.05 M guanidine thiocyanate (≥ 97%, Aldrich), 0.6 M 1,2-dimethyl-3-propylimidazolium iodide (DMPII, Solaronix SA), and 0.5 M 4-tert-butylpridine (96%, Aldrich) in acetonitrile. $Co^{2+/3+}(bpy)_3$ and $Cu^{+/2+}(dmp)_2$ catholytes were composed of 0.25 M $Co^{2+}(bpy)_3(PF_6)_2$, 0.05 M $Co^{3+}(bpy)_3(PF_6)_3$, 0.1 M $LiClO_4$, and 0.5 M 4-tert-butylpyridine in acetonitrile and 0.2 M $Cu^{+}(dmp)_2$TFSI, 0.04 M $Cu^{2+}(dmp)_2$TFSI/Cl, 0.1 M $LiClO_4$, and 0.5 M 4-tert-butylpyridine in acetonitrile, respectively.

Characterization The absorbance spectra of dye desorption solution were recorded by the R928 photomultiplier tube of a UV-vis-NIR spectrophotometer (Cary 5000, Agilent Technologies, Inc.). The surface morphology of $LiMn_2O_4$ film was observed by field emission-scanning electron micro-scope (FE-SEM, Haitachi, S-4800). To identify the crystallinity of the graphitized $LiMn_2O_4$, X-ray diffraction (XRD) was carried out in a D8 ADVANCE system equipped with a DAVINCI (Bruker AXS) diffractometer using Cu Kα radiation operated at 40 kV and 10 mA. All electrochemical analyses were performed on potentiostats/galvanostats (BioLogic VMP3).

Photo-Charging/Galvanostatic Discharging Photo-charging current was measured using chronoamperometry technique applying 0 V of dc bias under the illumination. Following discharging was carried out using chronopotentiometry technique with various constant currents. Standard one sun condition (AM 1.5, 100 mW cm^{-2}) was simulated by photovoltaic efficiency measurement system (IQE-200, Newport Corporation). A commercial light-emitting diode lighting power (LG Innotek Co., Ltd.) was employed to simulate the indoor light intensity.

Cyclic Voltammetry Cyclic voltammetry was carried out at 100 mV s^{-1} of scan rate in a 3-electrode system containing Ag/AgCl (in a saturated aqueous potassium chloride solution) as the reference electrode and Pt wire as the counter-electrode in supporting electrolyte (0.1 M $LiClO_4$ in acetonitrile). Standard redox potentials were referenced versus that of ferrocene/ferrocenium (+0.63 V *vs.* NHE).

Controlled Intensity Modulated Photo-spectroscopy To study the photo-current and photo-voltage efficiency frequency response of DSSBs, controlled intensity modulated photo-spectroscopy (CIMPS) technique was carried out on a photoelectrochemical workstation (ZENNIUM XPOT, ZAHNER-elektrik GmbH & Co. KG) equipped with a frequency response analyzer and an automatically intensity-controlled light-emitting diode (503 nm). A small-amplitude sinusoidal pulse (~10% of dc potential) was applied to light source bias with frequency sweep from 10^5 to 10^{-1} Hz.

Linear Sweep Voltammetry and Impedance Spectroscopic Analyses Linear sweep voltammetry was carried out at 100 mV s^{-1} of scan rate with the symmetric cells consisting of two PEDOT-coated FTO substrates and the electrolyte same with the catholyte in DSSB. Electrochemical impedance spectroscopy was carried out with the same symmetric cells, applying a 10 mV sinusoidal pulse to a dc bias equivalent to the open circuit voltage (0 V) with the frequency sweep from 10^6 to 10^{-1} Hz. All obtained Nyquist plots were fitted with suitable equivalent circuits using ZView software (Scribner Associates, Inc.).

Time-Correlated Single Photon Counting Transient photoluminescence lifetime was measured on fluorescence lifetime spectrometer (FluoTime 300, PicoQuant GmbH), operated in time-correlated single photon counting (TCSPC) mode. The whole system was composed of a Ti:sapphire laser (Mira900, Coherent) with a ~150 fs pulse width and a 76 MHz repetition rate, emission monochromator (SP-2150i), and data acquirer (PicoHarp 300) with photon counting detector (microchannel plate photomultiplier tubes, R3809U-59). Collected decay signals and the instrumental response function were fitted together using an appropriate software (FlouFit, PicoQuant) to acquire the time constant.

The evaluation of electrochemical kinetic parameters For the measurements, I prepared symmetric cell that consists of two PEDOT-coated FTO electrodes and the electrolyte as depicted in **Figure 5.13a**. The rate constant (k_0) for charge transfer near electrode surface and ionic diffusion coefficient (*D*) values are summarized in **Table 5.1**. For both factors, symmetric cells containing I^-/I_3^- electrolyte always give the highest values, indicative of the fastest reaction and diffusion of I^-/I_3^-. The impedance spectroscopy analysis strongly supports linear sweep voltammetry results in terms of electrode/electrolyte interface impedance and Nernst diffusion impedance.

Figure 5.13c and **5.13d** present Nyquist plots obtained from symmetric cells with different electrolyte and equivalent circuit we adopted for fitting, respectively. It is apparent that I^-/I_3^- and $Co^{2+/3+}(bpy)_3$ feature two semicircles in impedance spectra, while $Cu^{+/2+}(dmp)_2$ is characterized by three semicircles. Nyquist plots obtained from the symmetric cells are generally composed of two semicircles, corresponding to charge transfer resistance at the electrode/electrolyte interface ($R_{CT,\ Ed/El}$) at high frequency region and Nernst diffusion impedance in the electrolyte (N_{bulk}) at low frequency region, respectively. However, when the electrode surface has a porous structure, additional element should be introduced to circuit to consider Nernst diffusion impedance within the electrode pores (N_{pore}).[59] This element has been known to appear at higher frequency region than that of $R_{CT,\ Ed/El}$. Therefore, we attributed additional semicircle at high frequency region (200~2.5 kHz) with $Cu^{+/2+}(dmp)_2$ electrolyte to sluggish ionic diffusion within the of PEDOT pore. For the other cases, diffusion limitation in PEDOT pore is negligible and thus the N_{pore} do not appear. All $R_{CT,\ Ed/El}$ and N_{bulk} values are summarized in **Table 5.1**. It is noteworthy that I^-/I_3^- provides very low R_{CT} (0.14 Ω) and N_{bulk} (0.55 Ω).

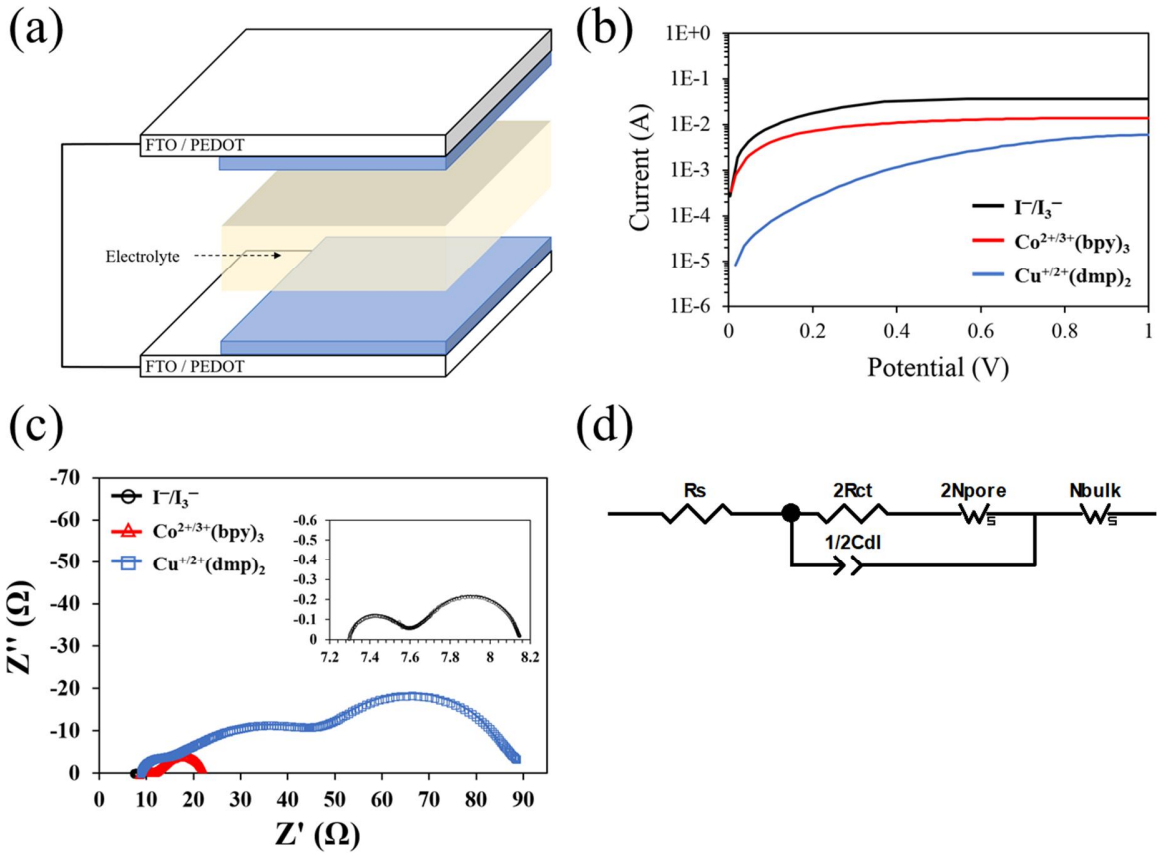

Figure 5.13 (a) The structure of symmetric cell used for (b) linear sweep voltammetry and (c) impedance analyses for rate constant (k_0) and ionic diffusion coefficient (D) of redox mediators, respectively. k_0 and D were estimated using the exchange current (I_0) and limiting current (I_{lim}) as following Eq.5.6 and Eq.5.7:

$$I_0 = nFAk_0C_O^{1-\alpha}C_R^{\alpha} \quad (5.6)$$

$$I_{lim} = 2nFAC_RD/\delta \quad (5.7)$$

where n is the number of electrons transferred in the electrochemical reaction, F is the faraday constant, A is the active area, C_O^* and C_R^* are bulk concentrations of redox species, α is the transfer coefficient (≈ 0.5), and δ is the distance between electrodes. (d) Equivalent circuit adopted for fitting impedance spectra.

REFERENCE

1. Patel, M. R., *Wind and solar power systems: design, analysis, and operation*. Second Edition ed.; CRC press: 2005.

2. Pehnt, M., Dynamic life cycle assessment (LCA) of renewable energy technologies. *Renewable Energy* **2006,** *31* (1), 55-71.

3. LaVan, D. A.; Cha, J. N., Approaches for biological and biomimetic energy conversion. *Proc. Natl. Acad. Sci. U. S. A.* **2006,** *103* (14), 5251-5255.

4. Helal, S.; Mann, W.; El-Zabadani, H.; King, J.; Kaddoura, Y.; Jansen, E., The gator tech smart house: A programmable pervasive space. *Computer* **2005,** *38* (3), 50-60.

5. Nasiri, A.; Zabalawi, S. A.; Mandic, G., Indoor power harvesting using photovoltaic cells for low-power applications. *IEEE Trans. Ind. Electron.* **2009,** *56* (11), 4502-4509.

6. Haight, R.; Haensch, W.; Friedman, D., Solar-powering the Internet of Things. *Science* **2016,** *353* (6295), 124-125.

7. Nagai, H.; Segawa, H., Energy-storable dye-sensitized solar cell with a polypyrrole electrode. *Chem. Commun.* **2004,** (8), 974-975.

8. Song, T.; Sun, B., Towards photo-rechargeable textiles integrating power conversion and energy storage functions: can we kill two birds with one stone? *ChemSusChem* **2013,** *6* (3), 408-10.

9. Ng, C. H.; Lim, H. N.; Hayase, S.; Harrison, I.; Pandikumar, A.; Huang, N. M., Potential active materials for photo-supercapacitor: A review. *J. Power Sources* **2015,** *296*, 169-185.

10. Schmidt, D.; Hager, M. D.; Schubert, U. S., Photo-Rechargeable Electric Energy Storage Systems. *Adv. Energy Mater.* **2016,** *6* (1), 1500369.

11. Yu, M.; McCulloch, W. D.; Huang, Z.; Trang, B. B.; Lu, J.; Amine, K.; Wu, Y., Solar-powered electrochemical energy storage: an alternative to solar fuels. *J. Mater. Chem. A* **2016,** *4* (8), 2766-2782.

12. De Rossi, F.; Pontecorvo, T.; Brown, T. M., Characterization of photovoltaic devices for indoor light harvesting and customization of flexible dye solar cells to deliver superior efficiency under artificial lighting. *Appl. Energy* **2015,** *156*, 413-422.

13. Freitag, M.; Teuscher, J.; Saygili, Y.; Zhang, X.; Giordano, F.; Liska, P.; Hua, J.; Zakeeruddin, S. M.; Moser, J.-E.; Grätzel, M., Dye-sensitized solar cells for efficient power generation under ambient lighting. *Nat. Photonics* **2017,** *11*, 372-378.

14. Tingare, Y. S.; Vinh, N. S. n.; Chou, H. H.; Liu, Y. C.; Long, Y. S.; Wu, T. C.; Wei, T. C.; Yeh, C. Y., New Acetylene□Bridged 9, 10□Conjugated Anthracene Sensitizers: Application in Outdoor and Indoor Dye□Sensitized Solar Cells. *Adv. Energy Mater.* **2017,** *1700032*.

15. Cojocaru, L.; Uchida, S.; Tamaki, K.; Jayaweera, P. V.; Kaneko, S.; Nakazaki, J.; Kubo, T.; Segawa, H., Determination of unique power conversion efficiency of solar cell showing hysteresis in the IV curve under various light intensities. *Sci. Rep.* **2017,** *7* (1), 11790.

16. Tsai, M.-C.; Wang, C.-L.; Chang, C.-W.; Hsu, C.-W.; Hsiao, Y.-H.; Liu, C.-L.; Wang, C.-C.; Lin, S.-Y.; Lin, C.-Y., A large, ultra-black, efficient and cost-effective dye-sensitized solar module approaching 12% overall efficiency under 1000 lux indoor light. *J. Mater. Chem. A* **2018,** *6*, 1995-2003.

17. Murakami, T. N.; Kawashima, N.; Miyasaka, T., A high-voltage dye-sensitized photocapacitor of a three-electrode system. *Chem. Commun*. **2005,** (26), 3346-8.

18. Hsu, C.-Y.; Chen, H.-W.; Lee, K.-M.; Hu, C.-W.; Ho, K.-C., A dye-sensitized photo-supercapacitor based on PProDOT-Et2 thick films. *J. Power Sources* **2010,** *195* (18), 6232-6238.

19. Bae, J.; Park, Y. J.; Lee, M.; Cha, S. N.; Choi, Y. J.; Lee, C. S.; Kim, J. M.; Wang, Z. L., Single-fiber-based hybridization of energy converters and storage units using graphene as electrodes. *Adv. Mater.* **2011,** *23* (30), 3446-3449.

20. Wee, G.; Salim, T.; Lam, Y. M.; Mhaisalkar, S. G.; Srinivasan, M., Printable photo-supercapacitor using single-walled carbon nanotubes. *Energy Environ. Sci.* **2011,** *4* (2), 413-416.

21. Chen, T.; Qiu, L.; Yang, Z.; Cai, Z.; Ren, J.; Li, H.; Lin, H.; Sun, X.; Peng, H., An Integrated "energy wire" for both photoelectric conversion and energy storage. *Angew. Chem. Int. Ed.* **2012,** *51* (48), 11977-80.

22. Sun, H.; You, X.; Deng, J.; Chen, X.; Yang, Z.; Chen, P.; Fang, X.; Peng, H., A twisted wire□ shaped dual□function energy device for photoelectric conversion and electrochemical storage. *Angew. Chem., Int. Ed.* **2014,** *53* (26), 6664-6668.

23. Xu, X.; Li, S.; Zhang, H.; Shen, Y.; Zakeeruddin, S. M.; Graetzel, M.; Cheng, Y.-B.; Wang, M., A power pack based on organometallic perovskite solar cell and supercapacitor. *ACS Nano* **2015,** *9* (2), 1782-1787.

24. Xue, Y.; Ding, Y.; Niu, J.; Xia, Z.; Roy, A.; Chen, H.; Qu, J.; Wang, Z. L.; Dai, L., Rationally designed graphene-nanotube 3D architectures with a seamless nodal junction for efficient energy conversion and storage. *Sci. Adv.* **2015,** *1* (8), e1400198.

25. Wen, Z.; Yeh, M.-H.; Guo, H.; Wang, J.; Zi, Y.; Xu, W.; Deng, J.; Zhu, L.; Wang, X.; Hu, C.; Zhu, L.; Sun, X.; Wang, Z. L., Self-powered textile for wearable electronics by hybridizing fiber-shaped nanogenerators, solar cells, and supercapacitors. *Sci. Adv.* **2016,** *2* (10), e1600097.

26. Scalia, A.; Bella, F.; Lamberti, A.; Bianco, S.; Gerbaldi, C.; Tresso, E.; Pirri, C. F., A flexible and portable powerpack by solid-state supercapacitor and dye-sensitized solar cell integration. *J. Power Sources* **2017,** *359*, 311-321.

27. Liu, R.; Wang, J.; Sun, T.; Wang, M.; Wu, C.; Zou, H.; Song, T.; Zhang, X.; Lee, S.-T.; Wang, Z. L., Silicon Nanowire/Polymer Hybrid Solar Cell-Supercapacitor: A Self-Charging Power Unit with a Total Efficiency of 10.5%. *Nano Lett.* **2017,** *17*, 4240-4247.

28. Andreas, H. A., Self-Discharge in Electrochemical Capacitors: A Perspective Article. *J. Electrochem. Soc.* **2015,** *162* (5), A5047-A5053.

29. Guo, W.; Xue, X.; Wang, S.; Lin, C.; Wang, Z. L., An integrated power pack of dye-sensitized solar cell and Li battery based on double-sided TiO2 nanotube arrays. *Nano Lett.* **2012,** *12* (5), 2520-2523.

30. Xu, J.; Chen, Y.; Dai, L., Efficiently photo-charging lithium-ion battery by perovskite solar cell. *Nat. Commun.* **2015,** *6*, 8103.

31. Yu, M.; McCulloch, W. D.; Beauchamp, D. R.; Huang, Z.; Ren, X.; Wu, Y., Aqueous lithium–iodine solar flow battery for the simultaneous conversion and storage of solar energy. *J. Am. Chem. Soc.* **2015,** *137* (26), 8332-8335.

32. Li, Q.; Li, N.; Liu, Y.; Wang, Y.; Zhou, H., High□Safety and Low□Cost Photoassisted Chargeable Aqueous Sodium□Ion Batteries with 90% Input Electric Energy Savings. *Adv. Energy Mater.* **2016,** *6* (18), 1600632.

33. Liao, S.; Shi, J.; Ding, C.; Liu, M.; Xiong, F.; Wang, N.; Chen, J.; Li, C., Photoelectrochemical regeneration of all vanadium redox species for construction of a solar rechargeable flow cell. *J. Energy Chem.* **2018,** *27* (1), 278-282.

34. Noh, H. K.; Park, H. S.; Jeong, H. Y.; Lee, S. U.; Song, H. K., Doubling the capacity of lithium manganese oxide spinel by a flexible skinny graphitic layer. *Angew. Chem., Int. Ed.* **2014,** *53* (20), 5059-63.

35. Wedege, K.; Azevedo, J.; Khataee, A.; Bentien, A.; Mendes, A., Direct solar charging of an organic–inorganic, stable, and aqueous alkaline redox flow battery with a hematite photoanode. *Angew. Chem., Int. Ed.* **2016,** *55* (25), 7142-7147.

36. Azevedo, J.; Seipp, T.; Burfeind, J.; Sousa, C.; Bentien, A.; Araújo, J. P.; Mendes, A., Unbiased solar energy storage: Photoelectrochemical redox flow battery. *Nano Energy* **2016,** *22*, 396-405.

37. Tsao, H. N.; Yi, C.; Moehl, T.; Yum, J. H.; Zakeeruddin, S. M.; Nazeeruddin, M. K.; Grätzel, M., Cyclopentadithiophene Bridged Donor–Acceptor Dyes Achieve High Power Conversion Efficiencies in Dye□Sensitized Solar Cells Based on the tris□Cobalt Bipyridine Redox Couple. *ChemSusChem* **2011,** *4* (5), 591-594.

38. Sapp, S. A.; Elliott, C. M.; Contado, C.; Caramori, S.; Bignozzi, C. A., Substituted polypyridine complexes of cobalt (II/III) as efficient electron-transfer mediators in dye-sensitized solar cells. *J. Am. Chem. Soc.* **2002,** *124* (37), 11215-11222.

39. Boschloo, G.; Hagfeldt, A., Characteristics of the iodide/triiodide redox mediator in dye-sensitized solar cells. *Acc. Chem. Res.* **2009,** *42* (11), 1819-1826.

40. Klahr, B. M.; Hamann, T. W., Performance enhancement and limitations of cobalt bipyridyl redox shuttles in dye-sensitized solar cells. *J. Phys. Chem. C* **2009,** *113* (31), 14040-14045.

41. Bai, Y.; Yu, Q.; Cai, N.; Wang, Y.; Zhang, M.; Wang, P., High-efficiency organic dye-sensitized mesoscopic solar cells with a copper redox shuttle. *Chem. Commun.* **2011,** *47* (15), 4376-4378.

42. Freitag, M.; Daniel, Q.; Pazoki, M.; Sveinbjörnsson, K.; Zhang, J.; Sun, L.; Hagfeldt, A.; Boschloo, G., High-efficiency dye-sensitized solar cells with molecular copper phenanthroline as solid hole conductor. *Energy Environ. Sci.* **2015,** *8* (9), 2634-2637.

43. Hagfeldt, A.; Boschloo, G.; Sun, L.; Kloo, L.; Pettersson, H., Dye-Sensitized Solar Cells. *Chem. Rev.* **2010,** *110* (11), 6595-6663.

44. Goodenough, J. B.; Park, K.-S., The Li-ion rechargeable battery: a perspective. *J. Am. Chem. Soc.* **2013,** *135* (4), 1167-1176.

45. Cohn, A. P.; Erwin, W. R.; Share, K.; Oakes, L.; Westover, A. S.; Carter, R. E.; Bardhan, R.; Pint, C. L., All silicon electrode photocapacitor for integrated energy storage and conversion. *Nano Lett.* **2015,** *15* (4), 2727-2731.

46. Wang, W.; Luo, Q.; Li, B.; Wei, X.; Li, L.; Yang, Z., Recent progress in redox flow battery research and development. *Adv. Funct. Mater.* **2013,** *23* (8), 970-986.

47. Liao, S.; Zong, X.; Seger, B.; Pedersen, T.; Yao, T.; Ding, C.; Shi, J.; Chen, J.; Li, C., Integrating a dual-silicon photoelectrochemical cell into a redox flow battery for unassisted photocharging. *Nat. Commun.* **2016,** *7*, 11474.

48. Julien, C. M.; Mauger, A.; Zaghib, K.; Groult, H., Comparative issues of cathode materials for Li-ion batteries. *Inorganics* **2014,** *2* (1), 132-154.

49. Li, W.; Fu, H. C.; Li, L.; Cabán□Acevedo, M.; He Jr, H.; Jin, S., Integrated photoelectrochemical solar energy conversion and organic redox flow battery devices. *Angew. Chem., Int. Ed.* **2016,** *55* (42), 13104-13108.

50. Zhu, K.; Jang, S.-R.; Frank, A. J., Impact of high charge-collection efficiencies and dark energy-loss processes on transport, recombination, and photovoltaic properties of dye-sensitized solar cells. *J. Phys. Chem. Lett.* **2011,** *2* (9), 1070-1076.

51. Barnes, P. R.; Anderson, A. Y.; Juozapavicius, M.; Liu, L.; Li, X.; Palomares, E.; Forneli, A.; O'Regan, B. C., Factors controlling charge recombination under dark and light conditions in dye sensitised solar cells. *Phys. Chem. Chem. Phys.* **2011,** *13* (8), 3547-3558.

52. Barnes, P. R.; Miettunen, K.; Li, X.; Anderson, A. Y.; Bessho, T.; Gratzel, M.; O'Regan, B. C., Interpretation of optoelectronic transient and charge extraction measurements in dye□sensitized solar cells. *Adv. Mater.* **2013,** *25* (13), 1881-1922.

53. Yella, A.; Lee, H.-W.; Tsao, H. N.; Yi, C.; Chandiran, A. K.; Nazeeruddin, M. K.; Diau, E. W.-G.; Yeh, C.-Y.; Zakeeruddin, S. M.; Grätzel, M., Porphyrin-Sensitized Solar Cells with Cobalt (II/III)–Based Redox Electrolyte Exceed 12 Percent Efficiency. *Science* **2011,** *334* (6056), 629-634.

54. Jin, M. Y.; Kim, B. M.; Jung, H. S.; Park, J. H.; Roh, D. H.; Nam, D. G.; Kwon, T. H.; Ryu, D. H., Indoline□Based Molecular Engineering for Optimizing the Performance of Photoactive Thin Films. *Adv. Funct. Mater.* **2016,** *26* (38), 6876-6887.

55. Kashif, M. K.; Axelson, J. C.; Duffy, N. W.; Forsyth, C. M.; Chang, C. J.; Long, J. R.; Spiccia, L.; Bach, U., A new direction in dye-sensitized solar cells redox mediator development: in situ fine-tuning of the cobalt (II)/(III) redox potential through Lewis base interactions. *J. Am. Chem. Soc.* **2012,** *134* (40), 16646-16653.

56. Sun, Z.; Liang, M.; Chen, J., Kinetics of iodine-free redox shuttles in dye-sensitized solar cells: interfacial recombination and dye regeneration. *Acc. Chem. Res.* **2015,** *48* (6), 1541-1550.

57. Wu, J.; Lan, Z.; Lin, J.; Huang, M.; Huang, Y.; Fan, L.; Luo, G., Electrolytes in dye-sensitized solar cells. *Chem. Rev.* **2015,** *115* (5), 2136-2173.

58. Park, S. M.; Ho, S.; Aruliah, S.; Weber, M. F.; Ward, C. A.; Venter, R. D.; Srinivasan, S., Electrochemical Reduction of Oxygen at Platinum Electrodes in KOH Solutions□Temperature and Concentration Effects. *J. Electrochem. Soc.* **1986,** *133* (8), 1641-1649.

59. Roy-Mayhew, J. D.; Bozym, D. J.; Punckt, C.; Aksay, I. A., Functionalized graphene as a catalytic counter electrode in dye-sensitized solar cells. *ACS Nano* **2010,** *4* (10), 6203-6211.

60. Ju, M. J.; Jeon, I. Y.; Kim, J. C.; Lim, K.; Choi, H. J.; Jung, S. M.; Choi, I. T.; Eom, Y. K.; Kwon, Y. J.; Ko, J., Graphene Nanoplatelets Doped with N at its Edges as Metal□Free Cathodes for Organic Dye□Sensitized Solar Cells. *Adv. Mater.* **2014,** *26* (19), 3055-3062.

61. Pears, A., *Strategic study of household energy and greenhouse issues*. Sustainable Solutions Pty Ltd: 1998.

62. Li, D. H.; Lam, T. N.; Wong, S., Lighting and energy performance for an office using high frequency dimming controls. *Energy Convers. Manage.* **2006,** *47* (9-10), 1133-1145.

63. Bai, Y.-W.; Ku, Y.-T., Automatic room light intensity detection and control using a microprocessor and light sensors. *IEEE Trans. Consum. Electron.* **2008,** *54* (3), 1173-1176.

64. Kim, B.-M.; Han, H.-G.; Kim, J. S.; Shin, H.; Kwon, T.-H., Control and Monitoring of Dye Distribution in Mesoporous TiO2 Film for Improving Photovoltaic Performance. *ACS Appl. Mater. Interfaces* **2017,** *9* (3), 2572-2580.

65. Lee, Y. L.; Lo, Y. S., Highly efficient quantum□dot□sensitized solar cell based on co□sensitization of CdS/CdSe. *Adv. Funct. Mater.* **2009,** *19* (4), 604-609.

66. Hao, Y.; Yang, W.; Zhang, L.; Jiang, R.; Mijangos, E.; Saygili, Y.; Hammarström, L.; Hagfeldt, A.; Boschloo, G., A small electron donor in cobalt complex electrolyte significantly improves efficiency in dye-sensitized solar cells. *Nat. Commun.* **2016,** *7*, 13934.

67. Fisher, A.; Peter, L.; Ponomarev, E.; Walker, A.; Wijayantha, K., Intensity dependence of the back reaction and transport of electrons in dye-sensitized nanocrystalline TiO2 solar cells. *J. Phys. Chem. B* **2000,** *104* (5), 949-958.

68. Jennings, J. R.; Ghicov, A.; Peter, L. M.; Schmuki, P.; Walker, A. B., Dye-sensitized solar cells based on oriented TiO2 nanotube arrays: transport, trapping, and transfer of electrons. *J. Am. Chem. Soc.* **2008,** *130* (40), 13364-13372.

Acknowledgement

2013 년 12 월 끝자락, 권태혁 교수님과의 면담을 위해 처음 UNIST 를 방문했던 기억이 생생합니다. 그렇게 2014 년부터 시작된 저의 대학원 생활이 어느새 막바지에 이르렀습니다. 짧고도 길었던 지난 4 년 6 개월간의 시간은 저의 인생에 큰 영향을 주었고 돌이켜 보면 많은 분들의 격려와 도움 덕분에 무사히 학위 과정을 마칠 수 있었던 것 같습니다. 먼저 대학원 생활동안 저에게 끊임없는 격려와 가르침 주신 권태혁 교수님께 진심으로 감사의 인사를 드립니다. 교수님으로부터 받은 학문적 소양과 따뜻함은 앞으로 사회 생활을 헤쳐 나감에 있어 구심점이 될 것입니다. 부족한 저를 여기까지 이끌어 주셔서 감사합니다. 항상 초심을 잃지 않고 정진하도록 하겠습니다. 항상 저를 믿고 바라봐 주신 부모님, 많이 사랑합니다. 두 분은 순탄치만은 않았던 대학원 생활을 제가 견디고 달려올 수 있었던 원동력이었습니다. 하나밖에 없는 아들 잘 하고 있으니 조금만 더 참고 기다려주세요.

아울러 우리 ER Lab 울타리 안에 많은 동료들에게도 감사의 인사를 전합니다. Co-worker 이자 실험실 내 유일한 형인 정수형, 도중 연구주제가 바뀌어 힘든 부분이 있겠지만 머지 않아 좋은 결과 있을 거예요. 파이팅 하세요. 실험실 내 유일한 동갑내기인 현규, 그래서 그런지 알게 모르게 마음속으로 의지가 되었던 것 같네 ㅋㅋ 어서 DSSB 로 좋은 결과 만들어 보자. 나도 많이 도울게. Co-worker 이자 유일한 입학 동기 현오 SHIN, 돌이켜 보면 너한테 여러 측면에서 많이 의지를 했던 것 같네. 고독한 소주파인 나의 술친구가 되어줘서 고마웠음 ㅋ 남은 연구도 잘 진행해서 좋은 결실 이루길 바랄게. 넌 꼭 잘 될 거다 ㅋ 랩장으로써 ERL 을 이끌어 가고 있는 현탁, 연구적인 부분은 두말할 것도 없고 실험실 생활도 잘하고 있는 것 같아 보기 좋다. 형으로써 많은 도움주지 못해서 미안해 ㅜㅜ... 다재 다능한 ERL MC 광민, 몇 안되는 DSC 디바이스 가이인데 많은 도움주지 못해서 미안하네. 항상 정진하는 마음으로 연구 잘 진행해서 좋은 결실을 맺길 바라. 오피스 옆자리에서 묵묵히 논문을 보던 정혁, 벌써 졸업한지 2 년이 되었네. 좋은데 취직했다는 소식 들었어. 멀리서나마 축하의 메시지 보낸다. 막 사회에 나가서 활동하고 있을 언영, 같은 부산 주민이라고 이래저래 놀려 대긴 했지만 너그러운 마음으로 이해하길... 그게 부산 스타일 아니겠나 ㅎ 점점 상남자로 거듭나고 있는 정승, 처음 UNIST 와서 봤던 너의 앳된(?) 이미지가 아직도 생생하다 ㅋㅋ 분야는 다르지만 날이 갈수록 너의 연구들이 성숙하는 것 같아 보기 좋네.

하는 일들 모두 좋은 결실 맺길 바라고 함께 진행하고자 했던 일도 계속 돌파구를 찾아 보자구나. 합성과 디바이스 모두 섭렵한 만능 덕호, DSC 분야 연구자가 몇 안되는데 니가 있어 든든할 따름이다 ㅋ 지금까지 도움만 받고 주지는 못한 것 같아 미안하다... 앞으로도 파이팅이다. 유일한 부사수였던 준혁, 돌이켜보니 사수로써 해준게 없구나... 워낙 알아서 잘하니 신경 쓸 것도 없었다만... 앞으로도 지금처럼 잘 헤쳐 나가길 바라고 도움이 필요하면 언제든 얘기하길 바라. 알고 보면 여성스러운 민수, 언제나 바위처럼 묵직한 모습 그게 너의 최고 장점이라고 생각한다. 앞으로 더욱 적극적인 모습으로 새로 하는 일들도 좋은 결실 맺길 바라. 바이오 패밀리인 대리마을 주민 채헌과 ERL 패셔니스타 채규, 너희 둘은 어떨 때 보면 사이 좋은(?) 남매 같아 ㅋ 분야가 다르다 보니 너희들에게 별 도움을 주진 못했지만 알아서 잘 해왔고 앞으로도 잘 할거라고 믿는다. ERL 의 주역이 되어 실험실을 잘 이끌어 주길 바라. 항상 예의 바른 은혜, 저번에 구두로 얘기했듯이 연구도 실험실 생활도 너무 잘하고 있어서 보기 좋아. 함께 진행하는 연구도 앞으로 잘해 나가 보자구나. 이제 막 대학원 생활 시작한 왕효와 민규, 사실 난 너희가 제일 부럽다... 이해할 수 없겠지만... 천천히 꾸준히 정진해서 부끄럽지 않은 연구자가 되길 바란다. (민규야 저번 엠티 때 누워서 나누었던 담화는 정말 즐거웠다 ㅋ) 끝으로 실험실 막내인 학부생들 (성준, 병권, 정경, 경민), 앞으로 많이 배우고 선배들 도와서 실험실 잘 이끌어 나가길 바라.

학위과정 내내 실험을 함께 했던 co-worker 이명희 누님, 누님께는 co-work 하는 일 외에도 많은 부분을 배웠습니다. 덕분에 전기화학 분야 관련 지식들을 쉽게 접하고 배울 수 있었어요. 감사합니다. 새로이 하는 연구들도 잘 되 시길 바라고 계속 도움 드릴 수 있도록 할 게요. 지금은 중국에서 연구중인 명우야, 덕분에 UNIST 에서 첫 논문을 만들고 연구의 틀을 닦을 수 있었다. 거리가 멀어 자주 보기는 힘들지만 자주 연락하고 담에 만나면 또 칭따오 한잔 하자.

졸업 후에는 지금까지 보다 더욱 힘들고 넓은 사회에서의 시작이 기다리고 있을 거라고 생각합니다. 그럴 때마다 지금까지 받은 격려와 가름침들을 바탕으로 잘 헤쳐 나갈 것이며 새로운 도전을 즐기도록 하겠습니다. 모두 행복하세요.

2018 년 7 월

김병만 드림